THE UNIVERSITY OF CHICAGO

ELECTROMECHANICAL COUPLING AND GATING POLARITY IN VOLTAGE-GATED ION CHANNELS

A DISSERTATION SUBMITTED TO

THE FACULTY OF THE DIVISION OF THE BIOLOGICAL SCIENCES

AND THE PRITZKER SCHOOL OF MEDICINE

IN CANDIDACY FOR THE DEGREE OF

DOCTOR OF PHILOSOPHY

INTERDISCIPLINARY SCIENTIST TRAINING PROGRAM:

BIOCHEMISTRY AND MOLECULAR BIOPHYSICS

BY

MICHAEL DAVID CLARK

CHICAGO, ILLINOIS

DECEMBER 2019

Table of Contents

LIST OF FIGURES

LIST OF TABLES

ABBREVIATIONS

BK – Big K^+ (potassium channel of large conductance)

cAMP – cyclic adenosine monophosphate

cGMP – cyclic guanosine monophosphate

cNMP – cyclic nucleoside monophosphate

Ca_v – voltage-gated Ca^{2+} channel

CHS – cholesterol hemisuccinate

CNBD – cyclic nucleotide binding domain

CNBHD – cyclic nucleotide binding homology domain

CNG – cyclic nucleotide gated (ion channel)

Cryo-EM – cryogenic electron microscopy

DDM – n-dodecyl "-D maltopyranoside

DMCA – double mutant cycle analysis

DTT – dithiothreitol

Eag – Ether-a-go-go (ion channel, Eag1)

EDTA - Ethylenediaminetetraacetic acid

FL – full length

FSC – Fourier shell coefficient

FSEC – fluorescence size exclusion chromatography

GDN – glycol-diosgenin

GFP – green fluorescent protein

GOF – gain of function

HCN – Hyperpolarization activated, cyclic nucleotide gated (ion channel)

HEPES – 4-(2-hydroxyethyl)-1-piperazineethanesulfonic acid

hERG – human Ether-a-go-go-Related (ion channel)

HRV 3C – human rhinovirus 3C protease

H_v1 – human voltage-gated proton channel

IMAC – immobilized metal affinity chromatography

IPTG – isopropyl "-D-1-thiogalactopyranoside

KAT1 – K_v *Arabidopsis thaliana* 1 (ion channel)

KcsA – bacterial K+ channel

K_v – Voltage-gated potassium channel

LB – Luria Broth

LKT1 – lycopersicum K+ transporter 1 (ion channel)

LMNG – lauryl maltose neopentyl glycol

LOF – loss of function

MD – Molecular Dynamics

MVP – Methanocaldococcus voltage-sensitive protein (ion channel)

MWCO – Molecular Weight Cut Off

NaChBac – bacterial sodium channel

Na_v – Voltage-gated sodium channel

NaVAb – Bacterial voltage-gated sodium channel

NCS – non-crystallographic symmetry

pCNBD – pseudo cyclic nucleotide binding domain

PIP_2 – phosphatidylinositol bisphosphate

PMSF – phenylmethanesulfonylfluoride

P_o – open probability (normalized 0 to 1)

RCF – relative centrifugal force

RMS – Root Mean Square

RMSD – Root Mean Square Deviation

S1 – first transmembrane segment (and so on, S2, etc.)

SDS-PAGE – Sodium Dodecyl Lauryl Sulfate Polyacrylamide Gel Electrophoresis

SEC – Size Exclusion Chromatography

SEM – Standard Error of the Mean

SKOR – Stelar K+ Outward Rectifier (ion channel)

Tax-4 – CNG channel from *C. elegans*

TEVC – two electrode voltage clamp

TM – transmembrane

TMD – transmembrane domain

TPC – two pore (ion) channel

VGIC – voltage gated ion channel

VSD – voltage sensing domain

WT – wild type

2N2 – membrane scaffold belt protein

ACKNOWLEDGEMENTS

This thesis is the culmination of four years of work in the Perozo lab. However, the process actually began much earlier, with my mother and father, Diane and James. It is their wisdom and parenting skill that instilled in me the creativity and curiosity, diligence and perseverance, a strong sense of ethics that I imagine I possess. It is to them I dedicate this thesis. Throughout my childhood, my younger brother and best friend Jeff-ery was my constant companion in making discoveries (not all of which were “good”).

My high school chemistry teacher Marc Ehrhardt gave me a copy of the textbook Chemistry, seventh edition by Zumdahl and Zumdahl to borrow for the summer. Today, the textbook can be purchased for $4.19 on Amazon.com. However at the time I received the book, I realized Chemistry was priceless. As a chemistry major at Northwestern, I joined the lab of Ishwar Radhakrisnan as a freshman work-study student: washing dishes, and then eventually doing experiments. After a few mishaps, including adding MW standards to each SDS-PAGE sample (because what chemist doesn’t prefer a spike-in standard) I learned my way around the lab. Ishwar accelerated my development as a scientist, and he became my direct mentor: conscientious, critical, and committed absolutely to rigorous science and the development of his trainees.

The chance to work with Eduardo Perozo was one of the main reasons I came to UChicago. He cultivates a lab in which we are free to pursue discoveries and do science for the sake of science. Eduardo inspires with his creativity, passion, and magnetic and kind disposition. I am fortunate and grateful to be among the many he has trained and the countless he has inspired with his effusive and unadulterated love of science. I owe much to my colleagues at UChicago in the Perozo and Bezanilla labs. I admire them for many reasons: Tian for her tireless diligence

and kindness, Bharat for willingness in sharing his time and expertise, Gustavo – a modern era ion channel savant-philosopher, Rong for computational wizardry and deep and careful analysis, Elle for good humor and a neurobiology perspective. To a few hombres buenos for their friendship: Navid for a maniacal obsession with mechanosensitivity, Young Hoon for the contrast between his dark thoughts and cheerful disposition, and Alejandro for his kindness, humor and botanical brilliance. Thank you to Margaret who is one of the strongest, most inspirational people I'm proud to know. She is also an excellent lab manager. To my two former students, Ania and Jason, thank you for all the experimental help, but more importantly for teaching me how to teach. Thanks to many collaborators who made this work possible and enjoyable, Joe, Tera, and Pedro "Profe Chamo" in EM, Ray Hulse for data, ideas and hospitality. To Pancho, Nani and their lab for their kindness and great ideas: Elizabeth, Joao, Carlos, Bernardo and Li. Thank you to friends and classmates, especially those who are both like Maciek. And last but not least to my wonderful girlfriend Lillian. Having gone through this with you I can't imagine it without you.

Chapter 1: Introduction

A critical, and perhaps defining, aspect of life is the active maintenance of a non-equilibrium state (Schrodinger 1944). Much of this process occurs at the plasma membrane, where the cell expends inordinate amounts of "currency" constructing and maintaining a semipermeable barrier between itself and its surroundings, and then setting up gradients across this membrane (**Fig. 1-1**) (Hediger et al. 2004). The cell then outfits its membrane with a dazzling array of molecular machines, including transporters, receptors and channels. With these machines, cells make use of their electrochemical gradients to exchange nutrients, poisons, and information with each other and their environment in a process broadly termed cell signaling (Gouaux and MacKinnon 2005). Of the various modes of cell signaling (optical, electrical, chemical and mechanical), electrical signaling presents key advantages for multicellular organisms (Hille 1978). First, electrical signaling can take advantage of ion gradients established across membranes; thus every cell can use this mode of communication if desired. Second, conduction of electrical signals is rapid, outpacing the chemical signaling limited by small molecule diffusion. Third, electrical signaling has high fidelity, as the many constituent channels and transporters can exhibit switch-like behavior on the microsecond time scale and over potential ranges of a few millivolts (Bezanilla 2008). Finally, bioelectrical signaling naturally lends itself to construction of robust feedback mechanisms, seen clearly in the voltage-gated ion channel (VGIC). Such proteins conduct ions, and the ion conductance is itself regulated by membrane potential (Hodgkin and Huxley 1952; Catterall 1995). By combining different VGICs with distinct ionic selectivity and voltage dependence, organisms generate complex electrical behavior like the autonomous, rhythmic cardiac/neuron action potentials that underlie pacemaking (Brown et al. 1979; Santoro et al. 1998).

Figure 1-1

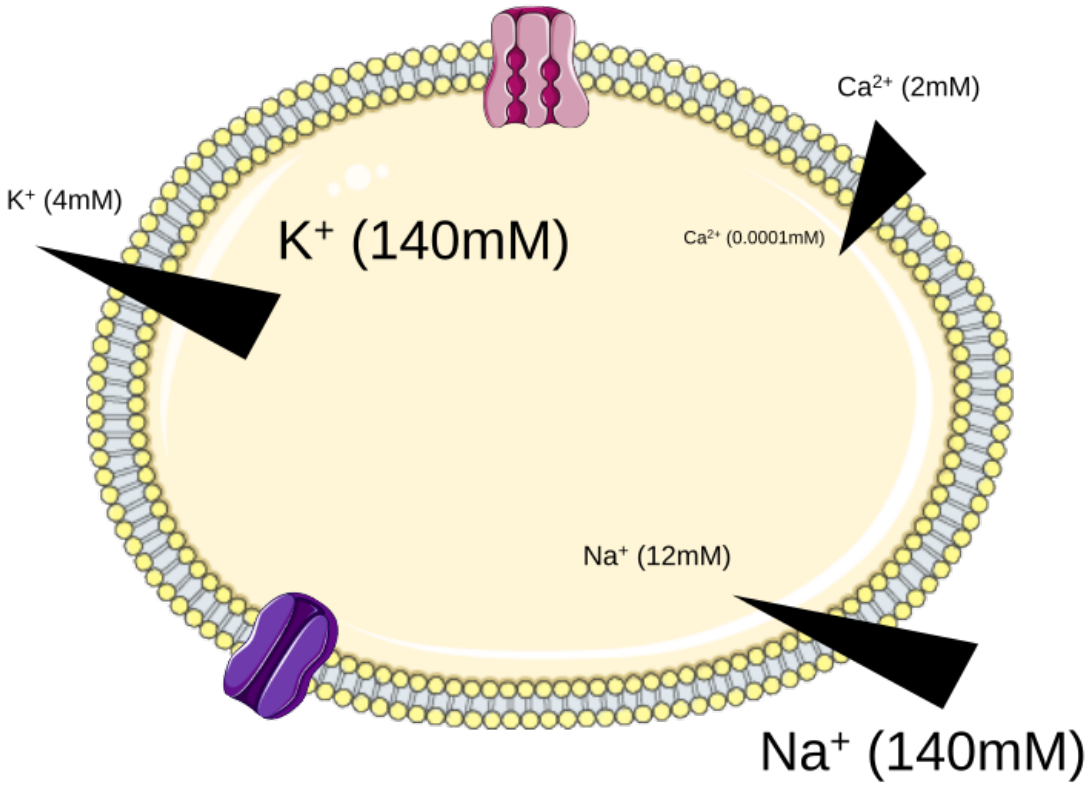

Figure 1-1: Cation gradients in eukaryotic cells

Cartoon of eukaryotic cell depicting gradients of major cations (K^+, Na^+, and Ca^{2+}). Gradients can be generated by active transporters (pink), and dissipated by channels (purple).

A significant body of work on VGICs has allowed us to begin to decode the language of intercellular electrical communication. Beginning in 1791, Luigi Galvani published experimental evidence of animal electricity, recorded using his primitive electrophysiology rig comprising a lightning rod to a dead frog. In the following century, extracellular action potentials were recorded with increasing sophistication. It wasn't until the discovery of the squid giant axon as a model system (Young 1936) that the first intracellular action potential was recorded (Curtis and Cole 1940, Hodgkin and Huxley 1939). One of several key realizations of Hodgkin, Huxley and Katz was the voltage dependence of the ionic conductance in squid giant axons (Hodgkin and Huxley 1952, Hodgkin et al. 1952). Using voltage clamp, current clamp, and manipulation of ionic conditions, Hodgkin and Huxley gathered the data required to formulate their mathematical model of the voltage-dependent ionic conductances which give rise to the action potential (Hodgkin and Huxley 1952).

Today, we know that VGICs are responsible for these voltage-dependent currents measured in frog muscle and squid axons. One of the most fundamental characteristics of a VGIC is its gating polarity: whether it opens upon membrane depolarization, or upon membrane hyperpolarization (**Fig. 1-2a**). The physiological distinction between these two channel types is significant. Depolarization-activated channels are far more common, with Na+ and K+, selective types underlying the initiation (Na+) and termination (K+) of the action potential measured by countless physiologists. Hyperpolarization-activated channels on the other hand, perform specialized physiological functions as inwardly rectifying cation channels. Complex electrical activity can be built by combining the distinct activities of depolarization and hyperpolarization-activated channels, perhaps seen most strikingly in pacemaker cells (**Fig. 1-2b**) (Brown et al. 1979). In mammals, hyperpolarization-activated, cyclic nucleotide-gated (HCN) channels form the funny current, an inward sodium/potassium current that is activated by the undershoot following an action potential (**Fig. 1-2b**, blue component) (Santoro et al. 1998). Thus, this

hyperpolarization-activated channel allows for rhythmic firing, lending pacemaking activity to cardiomyocytes and neurons.

Figure 1-2

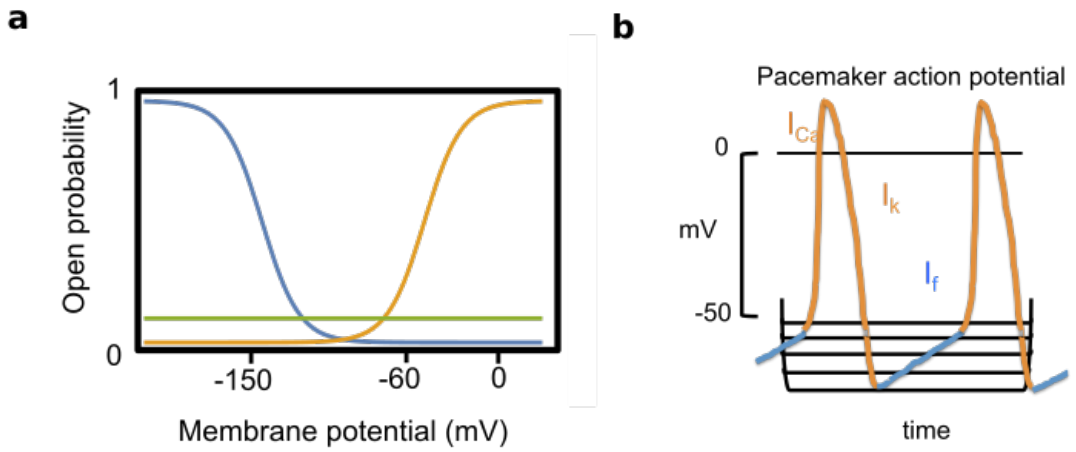

Figure 1-2: Ion channel response to voltage and the physiological importance of gating polarity **a,** A plot of channel open probability as a function of voltage can distinguish three types of response to membrane potential (voltage). Voltage-independent/leak channels (green), depolarization-activated channels (orange) and hyperpolarization-activated channels (blue). **b,** The pacemaker action potential utilizes depolarization-activated (orange) and hyperpolarization-activated (blue) conductances. Note that the hypolarization-activated conductance (funny current, I_f) is required for successive firing, giving rise to pacemaking. Figure is a schematization of data from rat sinoatrial node from Brown et al. 1979.

Following the molecular cloning, electrophysiological recording and structure determination of VGICs, we know many molecular details of these channels, with the voltage-gated potassium (K_v) channels the most well understood. Structurally, K_v channels are tetrameric protein assemblies consisting of four voltage sensing domains (VSDs) and one tetrameric pore domain (**Fig. 1-3b**) (Bezanilla, 2008; MacKinnon, 1991; Sigworth, 1993; Swartz, 2008; Tombola et al., 2006a). Each individual VSD contains four transmembrane segments (S1-S4), the fourth of which contains a string of gating charges: arginines and lysines, arranged in a conserved RxxRxxR pattern (where R is arginine, and x is typically a hydrophobic residue). The remaining helices of the VSD (S1-S3) contain a central hydrophobic gasket, which acts as a charge transfer center: a high-energy barrier through which the gating charges cross upon a change in the transmembrane electric field. S1-S3 also contain distributed countercharge residues, typically aspartates and glutamates that form salt bridge pairs with the gating charges (**Fig. 1-3c**). In the consensus model of VGIC activation, the first step comprises a movement of the gating charges across the hydrophobic gasket, and the concomitant exchange of countercharge pairs (Vargas et al. 2011). The movement of these gating charges generates a capacitive current, termed a gating current, which is ~two orders of magnitude smaller than the ionic current, yet is still measurable (Armstrong and Bezanilla 1973). Gating current measurements, together with similar experiments using site-specific fluorescent probes in the VSD have informed consensus models of the VSD motions as they correlate with channel opening and closing. Essentially, these models posit a vertical motion of the S4 segment of 6-12 Å, corresponding to the exchange of between one and three gating charges across the gasket (Vargas et al. 2011). The specific details of VSD conformational changes are likely channel dependent, as the estimated charge transferred per VSD varies from ~1 e in the isolated VSD of the *Ciona intestinalis* voltage-sensitive phosphatase (Li et al. 2014), to ~3-4 in the Shaker K_v channel (Aggarwal and MacKinnon 1996).

Figure 1-3

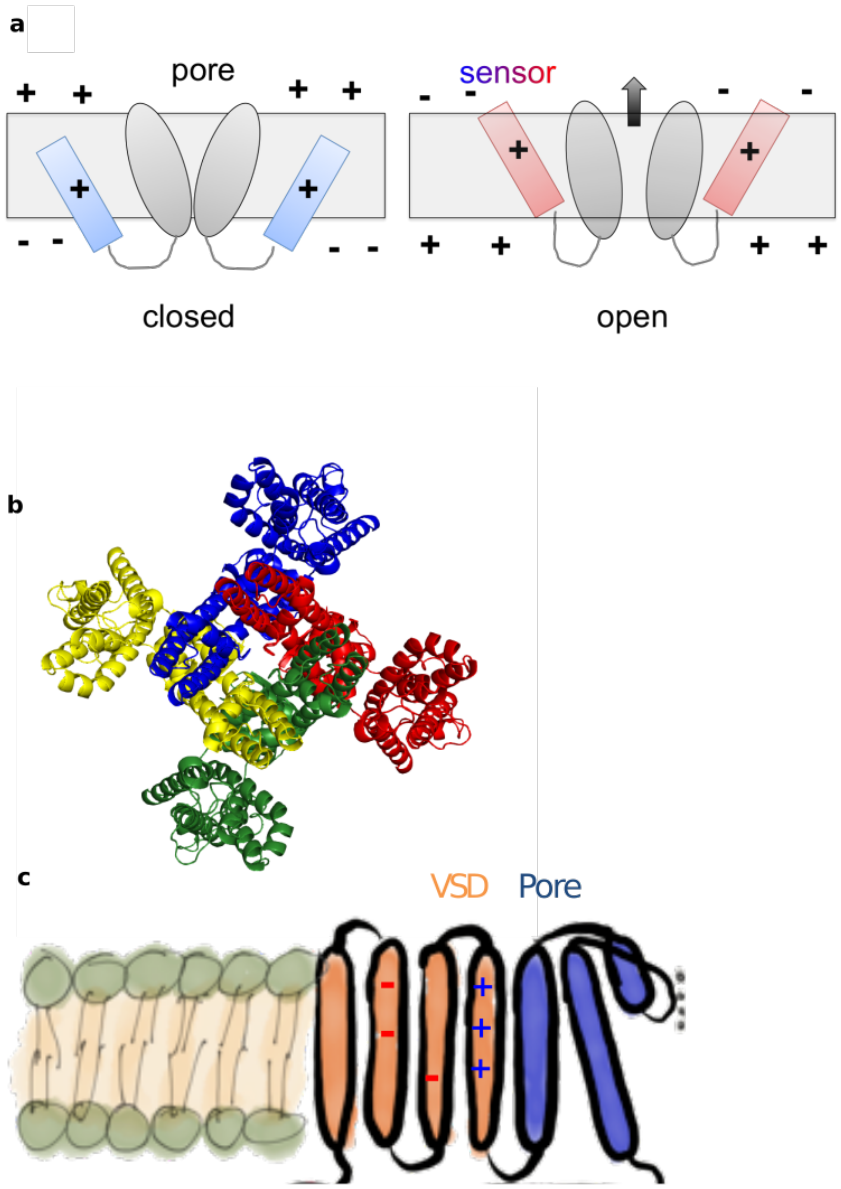

Figure 1-3: Cartoon depiction of a depolarization-activated ion channel

a, Schematic representation of a positively-charge voltage sensor, linked to a pore. The sensor can either be resting (down), or activated (up), and the pore either closed or open. In a depolarization-activated ion channel, an activated sensor corresponds to an open pore. Figure based on Bezanilla 2000. **b,** Structure of $K_v1.2$ (Long et al. 2005) showing tetrameric arrangement of a VGIC. **c,** Cartoon of a single subunit of a VGIC. VSD (orange) has positive charges on its S4 segment, and negative charges on S1-S3. Pore subunit (blue) tetramerizes to form ion conduction pathway.

Major goals of the ion channel field are to elucidate the structures of all states that constitute the activation pathway of a given channel, as well as characterize the dynamics of the transitions between these states. In terms of the VSD, recent progress has been made in Na_v and two-pore potassium channels (TPCs), which have yielded structures with VSDs in both 'up' and 'down' states (Wisedchaisri et al. 2019; Xu et al. 2019; Guo et al. 2016; Kintzer et al. 2018). Comparison of these 'up' and 'down' VSDs have provided support for a vertical S4 motion in the cases of a chimeric Na_v toxin complex (Xu et al. 2019) and of a disulfide-crosslinked Na_v (Wisedchaisri et al. 2019), and a electric-field refocusing / transporter model for TPC (Kintzer et al. 2018). The divergence of VSD activation mechanisms proposed for Na_v and TPC highlight the need for further detailed studies in which multiple states of the same channel are captured / interrogated.

While at present we have an impressive understanding of the general conformational landscape of VSDs, we know much less about how VSDs are energetically coupled to the pore domain. This electromechanical coupling allows the electric field-driven conformational changes arising in the VSDs to be mechanically transmitted to the pore, thereby opening or closing the gate (Chowdhury and Chanda, 2012; Long et al., 2005; Vardanyan and Pongs, 2012). Recent VGIC structures have revealed large differences in the physical relationship between the VSDs and the pore, with VGICs best classified as either domain-swapped or non-domain-swapped (**Fig. 1-4**) (Whicher and MacKinnon, 2016). In domain-swapped VGICs, each VSD is situated adjacent to the pore subunit of the neighboring protomer, while in non-domain-swapped VGICs each VSD apposes the pore subunit of its own protomer. The majority of studies of VSD-pore coupling have been performed on domain-swapped VGICs, which includes the prototypical *Drosophila* Shaker K_v channel and mammalian K_v1 channel (Long et al. 2005). Domain-swapped VGICs, which also include all Na_v, Ca_v and TPCs are necessarily activated by membrane depolarization. Non-domain-swapped ion are functionally intriguing: within this

subgroup are channels with opposite gating polarity: depolarization-activated like ether-a go go (Eag) and human ether-a go go-related gene (hERG) and hyperpolarization-activated like HCN and KAT1, as well as voltage-independent cyclic nucleotide gated (CNG) channels (**Fig. 1-4b-d**).

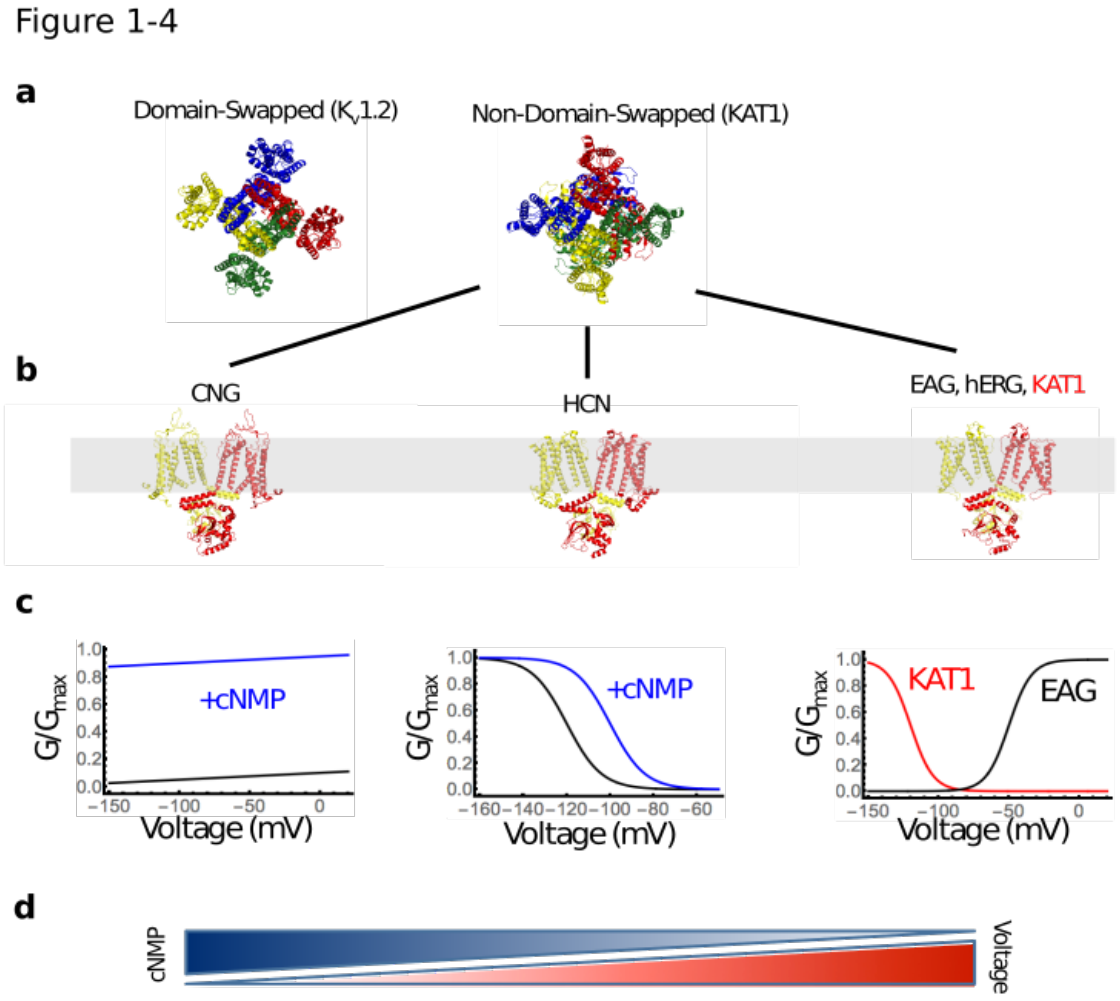

Figure 1-4: Structural and functional diversity of tetrameric ion channels.
a, Two major classes of channels, domain swapped and non-domain swapped are distinguished by the relative positions of VSD and pore domains. **b,** Solved structures of non-domain-swapped ion channels, two subunits shown for clarity **c,** G-V relations of each channel subclass **d,** Gradient depiction of cyclic-nucleotide and voltage sensitivity for subclass members. Figure inspired by James and Zagotta 2019.

VSDs are likely to function in mechanistically similar ways (with an outward movement of S4 upon depolarization, (Bezanilla, 2008; Swartz, 2008; Tombola et al., 2006b)) whether VGICs are domain swapped or not. This likely conservation in VSD mechanism prompts a key mechanistic question, which motivates the work presented in this thesis. How does an inward/downward movement of S4 close a depolarization-activated channel, yet drive a hyperpolarization-activated channel towards the open conformation? Considering that these channels share the same overall fold (4.7 Å transmembrane domain Cα RMSD between Eag1 and KAT1), the question becomes even more intriguing. A complete description of electromechanical coupling must account for both depolarization and hyperpolarization-activated ion channels, the latter of which are poorly structurally characterized.

The recent structures of non-domain swapped channels CNG (Li et al., 2017), Eag1 (Whicher and MacKinnon, 2016), HCN1 (Lee and MacKinnon, 2017) and hERG (Wang and MacKinnon, 2017) highlight the fact that although non-domain swapped VGICs share a common structural blueprint (figure S1), there isn't a clear correlation between their functional behavior and sequence similarity (**Fig. 1-4**). Hyperpolarization-activated hHCN1, shares only 23% sequence identity with atKAT1 within the transmembrane regions, yet atKAT1 and depolarization-activated rnEag are related by 28% transmembrane sequence identity. Moreover, the paucity of structural information on hyperpolarization-activated channels has made it difficult to test the generality of any mechanism beyond HCN1.

Thus, we sought to further characterize the structure and function of hyperpolarization-activated channels, as these channels play important physiological roles in animals and plants, and are functionally conserved in archaea. They are worthy subjects of investigation in their own right. Additionally, hyperpolarization-activation channels, as a biophysical anomaly, present a unique

opportunity to understand the general principles underlying VSD-pore coupling in the larger VGIC super family.

The animal hyperpolarization-activated, cyclic nucleotide-gated (HCN) channel is a Na/K selective channel that gives rise to the rhythmic firing activity of pacemaker cells in the heart and brain (Santoro et al. 1998). Activated by the hyperpolarizing undershoot at the end of an action potential, the HCN channel opens to allow Na entry, slowly depolarizing the cell toward threshold, which then activates Na_v or Ca_v channels to fire another action potential. Binding of cyclic nucleotide monophosphates (cNMPs), specifically cAMP, facilitates HCN channel activation (Altomare et al. 2001; Wainger et al. 2001), providing a mechanism for the autonomic nervous system to regulate heart rate.

The *Arabidopsis thaliana* hyperpolarization-activated K_v channel KAT1 is one of the best functionally characterized ion channels in plants, and has served as a unique model system for studies of electromechanical coupling due to its reversed gating polarity (Hedrich et al., 1995; Hoshi, 1995; Schachtman et al., 1992). Thus, in the physiological setting of the *Arabidopsis* guard cell, KAT1 conducts an inward K+ current, tuning the intracellular osmotic potential and driving the leaf stomatal aperture diameter via changes in turgor pressure (Hedrich, 2012). As higher plants like *Arabidopsis* lack the Na-K ATPase pumps of their animal counterparts they rely on K_v channels and K-H^+ pumps for maintenance of their potassium gradients.

Finally, a hyperpolarization activated K_v channel (MVP) has been found in the archaeal thermophile *Methanocaldococcus Jannaschi* (Sesti et al. 2003). The physiological role, if any, of MVP is unknown. However, the channel represents a unique snapshot in the evolutionary history of VGICs and lends itself well to biochemical and biophysical investigation due to its thermostability. Unlike the HCN and KAT1 channels, MVP lacks any intracellular or extracellular

domains, indicating that MVP may serve as a minimalist model system for reversed electromechanical coupling.

This thesis will devote its second chapter to the structural and functional characterization of the *Arabidopsis* hyperpolarization-activated K_v channel KAT1. We determined the cryo-EM structure of KAT1 in a closed state, and employed structure-guided mutagenesis and electrophysiology to interrogate the activation mechanism of the channel. Alanine scanning mutagenesis was used to probe the energetics of pore opening. Double mutant cycle analysis was used to construct experimentally constrained models of the down state of the KAT1 VSD. Energetics of mutants at the VSD-pore interface strongly indicates that in the absence of any VSD bias the pore domain is intrinsically closed. We propose a direct coupling mechanism in which minimally, a one click downward movement of the S4 segment towards the C-linker hairpin drives the S6 inner helical bundle towards the open conformation. This mechanism is reminiscent of a "reversed" direct coupling model as described for domain swapped VGICs (Bezanilla et al., 1994; Islas and Sigworth, 1999), and contrasts with the allosterically coupled voltage-sensitive mechanism reported for HCN channels (Altomare et al., 2001; Chen et al., 2007; Kusch et al., 2010). We also suggest that in our direct coupling mechanism, because S4 contacts the C-linker of the neighboring subunit, that while KAT1 is nominally/structurally non-domain-swapped, it is functionally domain swapped.

In the third chapter, this thesis will describe our efforts towards elucidation of the open state structure of KAT1. A direct comparison of open and closed structures of the same channel will provide invaluable insights into the activation mechanism; thus we have expended significant effort in identifying mutants which promote channel opening at 0 mV, which might be amenable to structure determination. We present our progress in determining the structures of such mutants using cryo-EM.

This third chapter will also include a structural and functional comparison of KAT1 and SKOR. *Arabidopsis* SKOR is a depolarization-activated K_v channel sharing 47% identity with KAT1 in the transmembrane region. In fact, KAT1 and SKOR are among the most similar VGICs with opposite gating polarity, and can serve as a model system for understanding electromechanical coupling. We present our progress towards determining the cryo-EM structure of SKOR, as well as discuss functional experiments designed to probe the effects of amino acid substitutions between KAT1 and SKOR.

This thesis will devote its fourth chapter to describing preliminary structural characterization of MVP using single particle cryo-electron microscopy (cryo-EM). Using a chimeric construct in which a four helix bundle from the channel KcsA was grafted to the C-terminus of MVP, a chimera-Fab complex was generated and imaged by cryo-EM. A low resolution (~10 Å resolution) reconstruction of this complex revealed significant conformational flexibility. We determined that MVP possesses a non-domain swapped architecture, a feature shared with all other hyperpolarization-activated ion channels of known structure (HCN1 and KAT1). In addition, the intracellular gate appears to be closed, consistent with functional measurements.

In its final chapter, this thesis will attempt to synthesize available structural and functional data on hyperpolarization-activated ion channels and advance the following classification of KAT1 as a reversed-K_v channel, rather than an HCN-like channel. This classification points to a mechanistic division in hyperpolarization-activated ion channels and also argues that the fundamental determinant of gating polarity is the detailed nature of contacts between the VSD and pore domain: the structural determinants of electromechanical coupling.

References

Altomare, C., Bucchi, A., Camatini, E., Baruscotti, M., Viscomi, C., Moroni, A., and Difrancesco, D. (2001). Integrated Allosteric Model of Voltage Gating of HCN Channels. J. Gen. Physiol. *117*, 519–532.

Aggarwal, S. K., & MacKinnon, R. (1996). Contribution of the S4 Segment to Gating Charge in the Shaker K+ Channel. Neuron, 16, 1169–1177.

Armstrong, C. M., & Bezanilla, F. (1973). Currents Related to Movement of the Gating Particles of the Sodium Channels. Nature, 242, 459–561.

Bezanilla, F., Perozo, E., and Stefani, E. (1994). Gating of Shaker K+ channels: II. The components of gating currents and a model of channel activation. Biophys. J. *66*, 1011–1021.

Bezanilla, F. (2000). The Voltage Sensor in Voltage-Dependent Ion Channels. *Physiological Reviews*, *80*(2), 555–592.

Bezanilla, F. (2008). How membrane proteins sense voltage. Nat. Rev. Mol. Cell Biol. *9*, 323–332.

Blunck, R., and Batulan, Z. (2012). Mechanism of electromechanical coupling in voltage-gated potassium channels. Front. Pharmacol. *3*, 1–16.

Brown, H. F., Difrancesco, D., & Noble, S. J. (1979). How does adrenaline accelerate the heart? *Nature*, *280*, 1–2.

Catterall, W. A. (1995). STRUCTURE AND FUNCTION OF VOLTAGE-GATED ION CHANNELS. Annual Review of Biochemistry, 64, 493–531.

Chen, S., Wang, J., Zhou, L., George, M.S., and Siegelbaum, S.A. (2007). Voltage Sensor Movement and cAMP Binding Allosterically Regulate an Inherently Voltage-independent Closed − Open Transition in HCN Channels. J. Gen. Physiol. *129*, 175–188.

Chowdhury, S., and Chanda, B. (2012). Perspectives on: conformational coupling in ion channels: thermodynamics of electromechanical coupling in voltage-gated ion channels. J. Gen. Physiol. *140*, 613–623.

Chowdhury, S., Haehnel, B.M., and Chanda, B. (2014). Interfacial gating triad is crucial for electromechanical transduction in voltage-activated potassium channels. J. Gen. Physiol. *144*, 457–467.

Curtis, H. J. and Cole, K. S. (1940). Membrane action potentials from the squid giant axon. J. Cell. Comp. Physiol. 15,145 -157.

Gouaux, E., & MacKinnon, R. (2005). Principles of Selective Ion Transport in Channels and Pumps. *Science*, *310*, 1461–1465.

Guo, J., Zeng, W., Chen, Q., Lee, C., Chen, L., Yang, Y., Cang, C., Ren, D., and Jiang, Y. (2016). Structure of the voltage-gated two-pore channel TPC1 from Arabidopsis thaliana. Nature *531*, 196–201.

Hediger, M. A., Romero, M. F., Peng, J.-B., Rolfs, A., Takanaga, H., & Bruford, E. A. (2004). The ABCs of solute carriers: physiological, pathological and therapeutic implications of human membrane transport proteins. *Pflugers Archiv European Journal of Physiology*, *447*(5), 465–468.

Hedrich, R., Moran, O., Conti, F., Busch, H., Becker, D., Gambale, F., Dreyer, I., Kuch, A., Neuwinger, K., and Palme, K. (1995). Inward rectifier Potassium channels in plants differ from their animal counterparts in response to voltage and channel modulators. Eur. Biophys. J. *24*, 107–115.

Hedrich, R. (2012). Ion channels in plants. Physiol. Rev. *92*, 1777–1811.

Hille, B. (1978). Ionic channels in excitable membranes. Current problems and biophysical approaches. Biophysical Journal, 22(2), 283–294. http://doi.org/10.1016/S0006-3495(78)85489-7

Hodgkin, A. L. and Huxley, A. F. (1939). Action potentials recorded from inside a nerve fibre. Nature 144,710 -711.

Hodgkin, A. L. and Huxley, A. F. (1952). A quantitative description of membrane current and its application to conduction and excitation in nerve. J. Physiol. Lond. 117,500 -544.

Hodgkin, A. L., Huxley, A. F., and Katz, B. (1952). Measurement of current-voltage relations in the membrane of the giant axon of Loligo J. Physiol. 116: 424-448

Islas, L.D., and Sigworth, F.J. (1999). Voltage Sensitivity and Gating Charge in Shaker and Shab Family Potassium Channels. J. Gen. Physiol. *114*, 723–742.

James, Z.M., and Zagotta, W.N. (2018). Structural insights into the mechanisms of CNBD channel function. J. Gen. Physiol. *150*, 225–244.

Kintzer, A. F., Green, E. M., Dominik, P. K., Bridges, M., Armache, J.-P., Deneka, D., et al. (2018). Structural basis for activation of voltage sensor domains in an ion channel TPC1. *Proceedings of the National Academy of Sciences*, *115*(39), E9095–E9104.

Kusch, J., Biskup, C., Thon, S., Schulz, E., Nache, V., Zimmer, T., Schwede, F., and Benndorf, K. (2010). Interdependence of Receptor Activation and Ligand Binding in HCN2 Pacemaker Channels. Neuron *67*, 75–85.

Latorre, R., Olcese, R., Basso, C., Gonzalez, C., Muñoz, F., Cosmelli, D., and Alvarez, O. (2003). Molecular Coupling between Voltage Sensor and Pore Opening in the Arabidopsis Inward Rectifier K+ Channel KAT1. J. Gen. Physiol. *122*, 459–469.

Ledwell, J.L., and Aldrich, R.W. (1999). Mutations in the S4 Region Isolate the Final Voltage-dependent Cooperative Step in Potassium Channel Activation. J. Gen. Physiol. *113*, 389–414.

Lee, C.-H., and MacKinnon, R. (2017). Structures of the Human HCN1 Hyperpolarization-Activated Channel. Cell *168*, 111–120.

Li, Q., Wanderling, S., Paduch, M., Medovoy, D., Singharoy, A., McGreevy, R., Villalba-Galea, C.A., Hulse, R.E., Roux, B., Schulten, K., et al. (2014). Structural mechanism of voltage-dependent gating in an isolated voltage-sensing domain. Nat. Struct. Mol. Biol. *21*, 244–252.

Long, S.B., Campbell, E.B., and MacKinnon, R. (2005). Voltage sensor of Kv1.2: structural basis of electromechanical coupling. Science *309*, 903–908.

MacKinnon, R. (1991). Determination of the subunit stoichiometry of a voltage-activated potassium channel. Nature *350*, 232–235.

Männikkö, R., Elinder, F., and Larsson, H.P. (2002). Voltage-sensing mechanism is conserved among ion channels gated by opposite voltages. Nature *419*, 837–841.

Randich, A. M., Cuello, L. G., Wanderling, S. S., & Perozo, E. (2014). Biochemical and structural analysis of the hyperpolarization-activated K+ channel MVP. *Biochemistry*, *53*(10), 1627–1636. http://doi.org/10.1021/bi4014243

Santoro, B., Liu, D. T., Yao, H., Bartsch, D., Kandel, E. R., Siegelbaum, S. A., & Tibbs, G. R. (1998). Identification of a Gene Encoding a Hyperpolarization-Activated Pacemaker Channel of Brain. *Cell*, 717–729.

Schachtman, D.P., Schroeder, J.I., Lucas, W.J., Anderson, J.A., and Gaber, R.F. (1992). Expression of an Inward-Rectifying Potassium Channel by the Arabidopsis KAT1 cDNA. Science *258*, 1654–1658.

Schrodinger, E. What is life? Cambridge Press, 1944. 90-165

Sesti, F., Rajan, S., Gonzalez-Colaso, R., Nikolaeva, N., and Goldstein, S.A.N. (2003). Hyperpolarization moves S4 sensors inward to open MVP, a methanococcal voltage-gated potassium channel. Nat. Neurosci. *6*, 353–361.

Sigworth, F.J. (1993). Voltage gating of ion channels. Q. Rev. Biophys. *27*, 1–40.

Swartz, K.J. (2008). Sensing voltage across lipid membranes. Nature *456*, 891–897.

Tombola, F., Pathak, M.M., and Isacoff, E.Y. (2006). How Does Voltage Open an Ion Channel? Annu. Rev. Cell Dev. Biol. *22*, 23–52.

Vardanyan, V., and Pongs, O. (2012). Coupling of voltage-sensors to the channel pore: A comparative view. Front. Pharmacol. *3*, 1–10.

Vargas, E., Yarov-Yarovoy, V., Khalili-Araghi, F., Catterall, W.A., Klein, M.L., Tarek, M., Lindahl, E., Schulten, K., Perozo, E., Bezanilla, F., et al. (2012). An emerging consensus on voltage-dependent gating from computational modeling and molecular dynamics simulations. J. Gen. Physiol. *140*, 587–594.

Wainger, B. J., Degennaro, M., Santoro, B., Siegelbaum, S. A., & Tibbs, G. R. (2001). Molecular mechanism of cAMP modulation of HCN pacemaker channels. *Nature*, *411*, 805–810.

Whicher, J.R., and MacKinnon, R. (2016). Structure of the voltage-gated K+ channel Eag1 reveals an alternative voltage sensing mechanism. Science *353*, 664–669.

Wisedchaisri, G., Tonggu, L., McCord, E., El-Din, T. M. G., Wang, L., Zheng, N., & Catterall, W. A. (2019). Resting-State Structure and Gating Mechanism of a Voltage-Gated Sodium Channel. *Cell*, 1–24. http://doi.org/10.1016/j.cell.2019.06.031

Xu, H., Hackos, D.H., Koth, C.M., Xu, H., Li, T., Rohou, A., Arthur, C.P., Tzakoniati, F., Wong, E., and Estevez, A. (2019). Structural Basis of Nav1.7 Inhibition by a Gating-Modifier Spider Toxin. Cell *176*, 702–715.

Young, J. Z. (1936). The structure of nerve fibres in cephalopods and Crustacea. Proc. R. Soc. Lond. B 121,319 -337.

Chapter 2: The Cryo-EM Structure of the Hyperpolarization-Activated K^+ Channel KAT1: A Molecular Mechanism of Electromechanical Coupling

A condensed version of this chapter has been submitted for publication as:
The Cryo-EM Structure of the Hyperpolarization-Activated K^+ Channel KAT1: A Molecular Mechanism of Electromechanical Coupling
Michael David Clark, Gustavo F. Contreras, Rong Shen and Eduardo Perozo

Abstract

Voltage-gated potassium (K_v) channels orchestrate electrical signaling and control cell volume by gating in response to either membrane depolarization or hyperpolarization. Yet, while all voltage-sensing domains transduce transmembrane electric fields by a common mechanism involving the outward translocation of gating charges (Bezanilla 2008, Mannikko et al. 2002, Latorre et al. 2003), the general determinants of gating polarity remain poorly understood (Blunck and Batulan 2012). Here, we provide a molecular mechanism for electromechanical coupling and gating polarity in non-domain-swapped K_v channels based on the cryo-EM structure of KAT1, the hyperpolarization-activated K_v channel from *Arabidopsis thaliana*. KAT1 displays an activated voltage sensor, which interacts with a closed pore domain directly via two interfaces and indirectly via an intercalated phospholipid. Functional evaluation of KAT1 structure-guided mutants at the sensor-pore interfaces suggests a mechanism in which direct interaction between the sensor and C-linker hairpin in the adjacent pore subunit is the primary determinant of gating polarity. We suggest that a ~5-7 Å inward motion of the S4 sensor helix underlies a direct-coupling mechanism, driving a conformational reorientation of the C-linker and ultimately opening the activation gate formed by the S6 intracellular bundle. This direct-coupling mechanism contrasts with allosteric mechanisms proposed for hyperpolarization-activated HCN channels (Altomare et al. 2001), and represents an unexpected link between depolarization and hyperpolarization-activated channels.

Introduction

Voltage-gated ion channels (VGICs) are the key molecular entities responsible for cellular excitability and intercellular electrical communication in eukaryotes. Structurally, voltage-gated potassium (K_v) channels are protein assemblies consisting of four voltage-sensing domains (VSDs) and one tetrameric pore domain (Bezanilla, 2008; MacKinnon, 1991; Sigworth, 1993; Swartz, 2008; Tombola et al., 2006). The VSDs are physically linked and energetically coupled to the pore domain, such that electric field-driven conformational changes arising in the VSDs are mechanically transmitted to the pore domain, a process known as electromechanical coupling (Chowdhury and Chanda, 2012; Long et al., 2005; Vardanyan and Pongs, 2012). Recent VGIC structures have revealed large differences in the physical relationship between the VSDs and the pore, with VGICs best classified as either domain-swapped or non-domain-swapped (**Fig. 1-4**) (Whicher and MacKinnon, 2016). This distinction is based purely on structural considerations, namely whether a VSD directly abuts its own pore subunit (non-domain-swapped) or whether, via a helical S4-S5 linker, a VSD abuts its neighboring pore subunit (domain swapped) (**Fig. 1-4a**). Distinct coupling mechanisms are likely to exist in each of these architectures, with further mechanistic differences possible even within the same architecture. Indeed, within the non-domain-swapped subgroup are channels with opposite gating polarity, as well as voltage-independent cyclic nucleotide-gated (CNG) channels. The depolarization-activated channels include ether-a-go-go (Eag) and human ether-a-go-go-related gene (hERG), and the hyperpolarization-activated channels include hyperpolarization-activated cyclic nucleotide gated (HCN) and *Arabidopsis thaliana* K_v (KAT1) (**Fig. 1-4**). However, whether domain-swapped or not, VSDs are known to function in mechanistically similar ways in all VGICs (with an outward movement of S4 upon depolarization, and vice versa) (Bezanilla, 2008; Swartz, 2008; Tombola et al., 2006). Given that these channels share the same overall fold, how does a downward movement of S4 close Eag/hERG, yet open HCN/KAT1?

The *Arabidopsis thaliana* K_v channel KAT1 is one of the best functionally characterized ion channels in plants and has served as a unique model system for studies of electromechanical coupling due to its reversed gating polarity. KAT1 activates upon membrane hyperpolarization, yet unlike HCN, its gating is not modulated by cyclic nucleotides (Hedrich et al., 1995; Hoshi, 1995; Schachtman et al., 1992). Thus, in the physiological setting of the *Arabidopsis* guard cell, KAT1 conducts an inward K^+ current, tuning the intracellular osmotic potential and driving the leaf stomatal aperture diameter via changes in turgor pressure (Hedrich, 2012). The recent structures of non-domain-swapped channels, including a CNG channel (Li et al., 2017), Eag1 (Whicher and MacKinnon, 2016), HCN1 (Lee and MacKinnon, 2017), BK (Big Potassium), (Tao et al., 2017), and hERG (Wang and MacKinnon, 2017) highlight the fact that although non-domain-swapped VGICs share a common structural blueprint (**Fig. 1-4**) , there is not a clear correlation between their functional behavior and sequence similarity. All three share the CNBD-containing channel architecture as a basic scaffold (**Fig. 2-1**). Hidden among the potential differences in these sequences and structures is the possibility of elucidating the mechanistic principles underlying the polarity of electromechanical coupling.

Figure 2-1

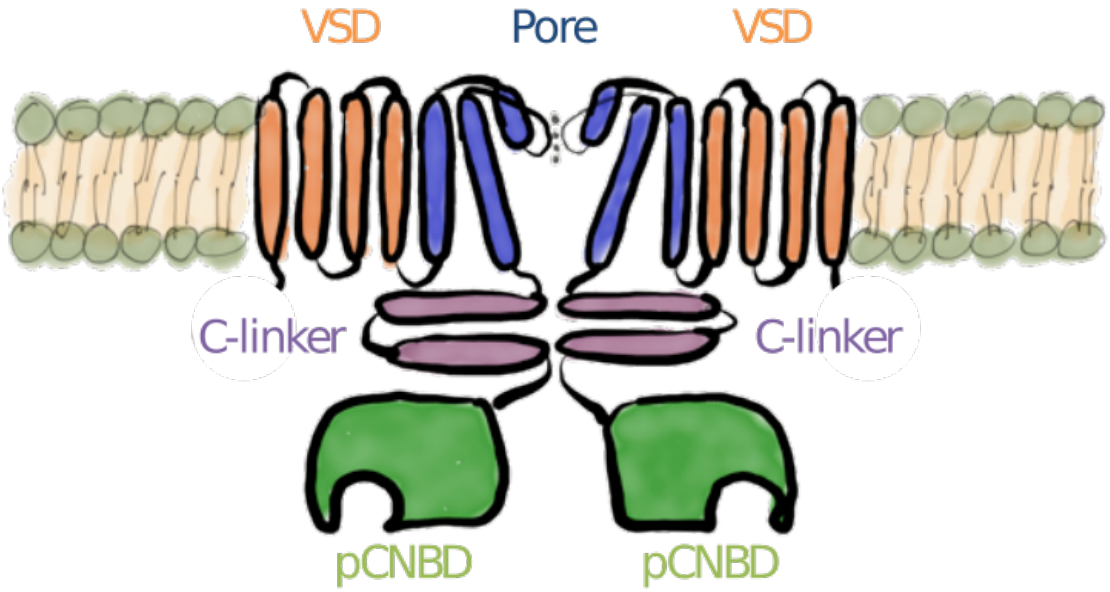

Figure 2-1: Cartoon of architecture of CNBD-containing channel KAT1

a, Cartoon with two subunits shown for clarity. Each subunit contains (starting from the N-terminus), a voltage-sensing domain (VSD), and pore domain subunit, a C-linker helical hairpin, and finally a cyclic nucleotide-binding domain (CNBD). In the cases that the CNBD is ligand-binding-incompetent, Eag1, hERG, etc., it is termed CNB-homology-D (CNBHD), or a pseudo-CNBD (pCNBD) in the case of KAT1.

The paucity of structural information on hyperpolarization-activated channels has made it difficult to test the generality of any coupling mechanism beyond HCN1. Here, we have determined the closed-state structure of KAT1 by cryo-EM in the nominal absence of a transmembrane electric field to address the question of reverse polarity voltage-dependent gating. Structure-guided mutagenesis, electrophysiology, and mutant cycle analysis were used to probe the energetics of pore opening, construct 'down' state models of the KAT1 VSD, and interrogate interactions between VSD and pore. Energetics of these mutants indicate that in the absence of any VSD bias the pore domain is intrinsically closed, and point to strong interactions between the S4 helix and the cytoplasmic C-linker (a helical hairpin extending directly from S6). Taken together, our data are consistent with an obligatory coupling mechanism in which minimally, a one helical turn ('one-click', ~5 Å) downward movement of the S4 segment towards the C-linker hairpin of the neighboring subunit drives the S6 inner helical bundle towards the open conformation. This mechanism contrasts with the allosterically-coupled, voltage-sensitive gating reported for HCN channels (Altomare et al., 2001; Chen et al., 2007; Kusch et al., 2010) and is instead reminiscent of a "reversed" direct coupling model as described for depolarization-activated VGICs like Eag and hERG (Wang and MacKinnon, 2017; Whicher and MacKinnon, 2016).

Results and Discussion

Preliminary functional and biochemical characterization of Arabidopsis thaliana KAT1

KAT1 yields large (microamp) inward potassium currents when expressed in Xenopus oocytes, and has thus served as a model system for physiologists (**Fig. 2-2**) (Schachtman et al., 1992). We began our studies by testing the function of a construct (which we term KAT1em, or KAT1-Ctrunc), which was previously shown to be fully functional, with similar activation kinetics and thermodynamics as the full-length channel (**Fig. 2-2**) (Marten and Hoshi, 1998). KAT1em comprises residues 1-501, spanning the transmembrane region and predicted cyclic nucleotide binding domain (CNBD) **(Fig. 2-3)**. When compared to KAT1-full-length, as well as KAT1-C-del constructs, KAT1em showed superior biochemical behavior in terms of extraction yield, stability in detergent (**Fig. 2-3**) and fluorescence size exclusion chromatography (FSEC) peak homogeneity. Thus, KAT1em was subjected to further biochemical characterization. Purification of KAT1em in gentle detergent LMNG yielded two peaks of interest, which were fractionated and separately subjected to negative stain electron microscopy (**Fig. 2-3c**). The first peak (larger molecular weight species) corresponded to an 'octamer', a dimer of tetramers in which KAT1em channels stack back-to-back via their cytoplasmic domains, forming a dumbbell shaped complex. The second peak (smaller molecular weight species) corresponded to a tetramer, based on particle size and SEC retention volume. An extensive screen was carried out by FSEC, in which buffer pH, ionic strength, and detergent were varied in order to maximize the proportion of either tetramer, or octamer (data not shown). Optimized conditions lead to preparations of mostly octamer, which were then subjected to cryo-EM analysis (**Fig. 2-4**).

Figure 2-2

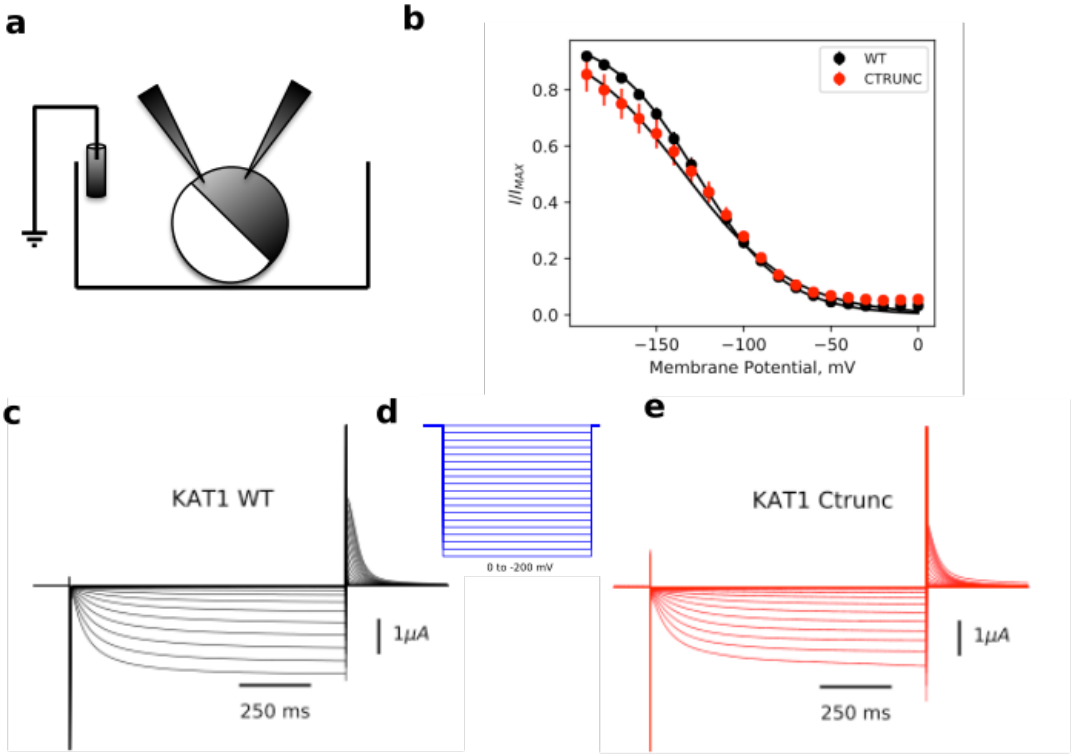

Figure 2-2: Function of *Arabidopsis thaliana* KAT1 and KAT1em construct.

a, Cartoon of Xenopus oocyte two electrode voltage clamp (TEVC) setup. Oocyte expressing an ion channel is placed in a bath with a ground electrode. The oocyte is impaled by two pipette electrodes, one which measures the membrane potential, and one which injects current to clamp the membrane at a commanded potential. **b,** Plot of I/Imax vs voltage for full-length KAT1 (black), and KAT1em (KAT1-Ctrunc, red), demonstrating activation by membrane hyperpolarization and indicating that truncation of the distal KAT1 C-terminus has a minimal effect on channel function. **c-e,** Representative macroscopic currents of full-length KAT1 (black, left), and KAT1em (KAT1-Ctrunc, red, right), recorded in *Xenopus* oocytes using a family of hyperpolarizing pulses (blue, middle).

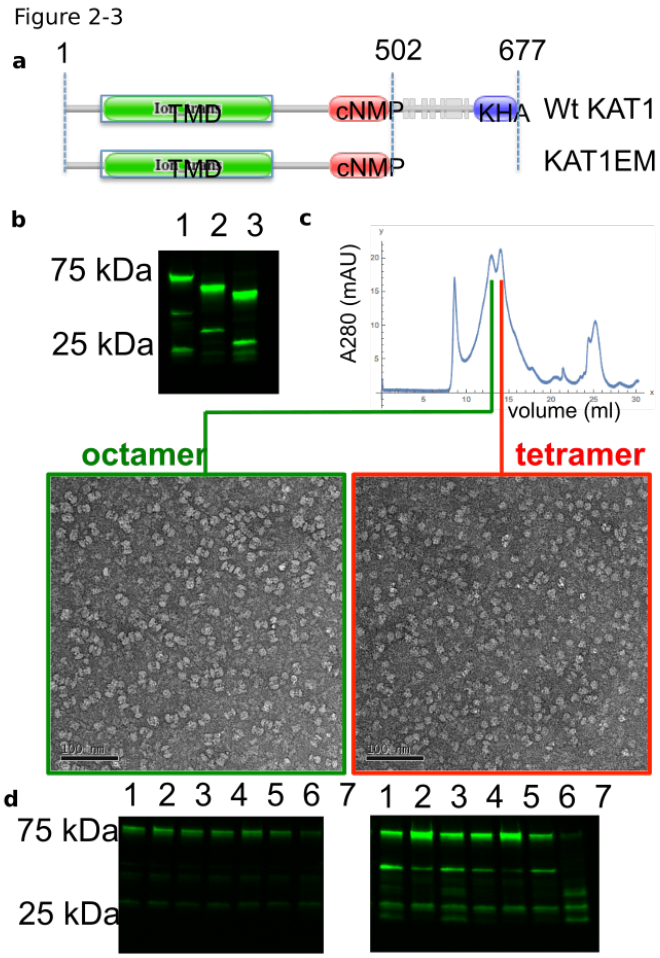

Figure 2-3: Preliminary biochemical characterization of *Arabidopsis thaliana* KAT1

a, Predicted domain diagram of KAT1, showing a transmembrane domain (TMD), a putative CNBD (cNMP-binding), a putative unstructured domain, and finally a KHA domain, found at the C-terminus of several plant ion channels. KAT1em construct is a truncation of unstructured region and KHA domain, and was shown to be fully functional (Fig 2-2). **b,** GFP in-gel fluorescence SDS-PAGE, showing expression of KAT1FL (1), KAT1C-del (2), and KAT1em (3) in sf9 insect cells. KAT1Cdel is a deletion of the putative unstructured region between cNMP-binding domain and KHA domain. **c,** Trial purification of KAT1em in gentle detergent LMNG. Two SEC peaks of interest are observed, when subjected to negative stain electron microscopy, the leading peak (green) is assigned as a dimer of tetramers, or octamer. The second peak (red) is assigned as a tetramer. **d,** GFP in-gel SDS-PAGE detergent screen of KAT1em in ESF9 cells (left gel) and sf9 cells (right cells). Detergents used are: 1% DDM/CHS (1), 1% DDM/CHS+20% glycerol (2), 2% DDM/CHS (3), 1% LMNG/CHS (4), 1% LMNG/CHS+20% glycerol (5), 1% GDN (6), 1% cymal-6 (7).

Figure 2-4

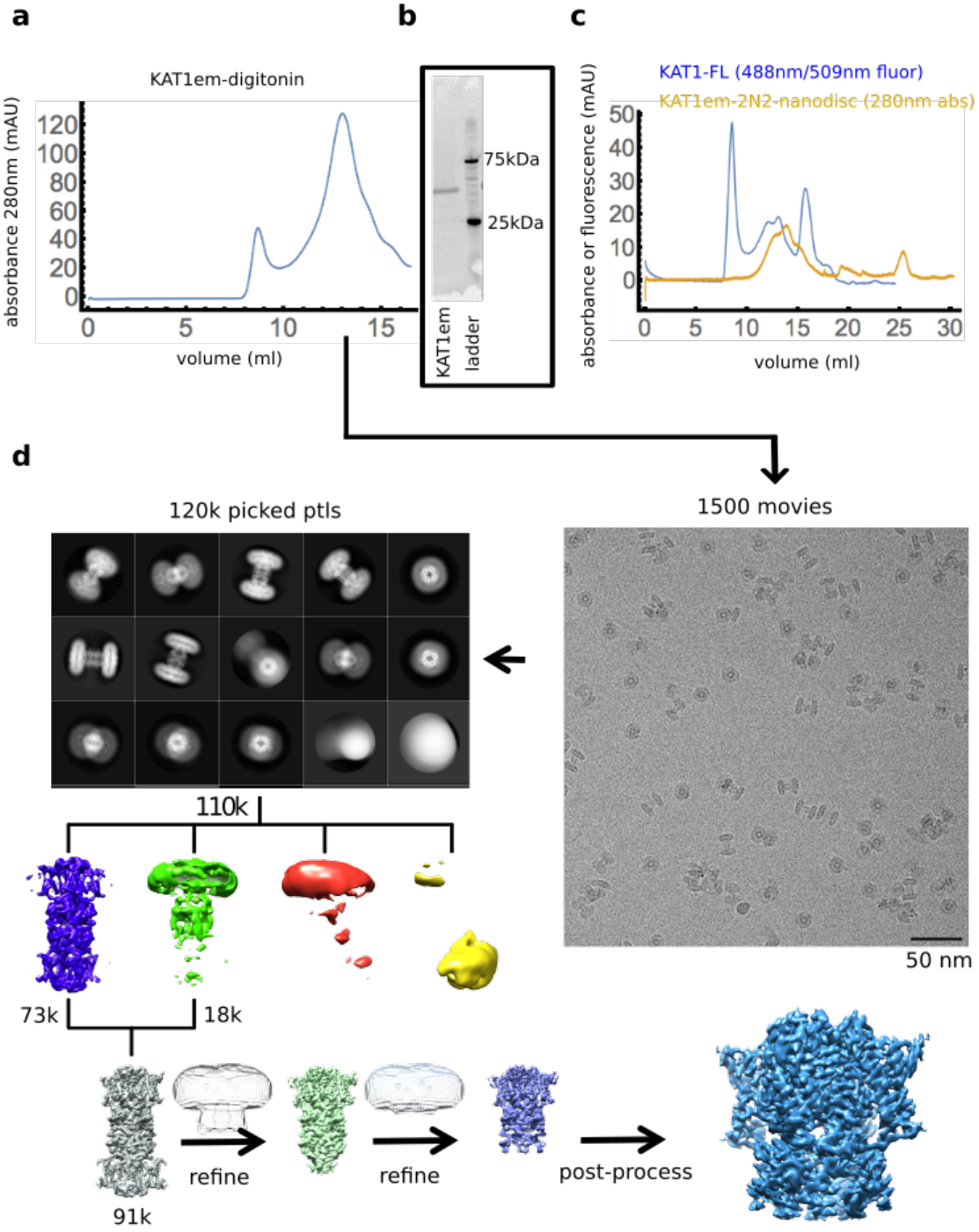

Figure 2-4: Optimized KAT1 biochemistry and cryo-EM workflow.

Figure 2-4, continued.

a, Size exclusion chromatograph (SEC) of Kat1em purified in digitonin, run on superose 6 column. **b,** Stain-free SDS-PAGE of purified Kat1em. **c,** SEC of KAT1em in 2N2 nanodiscs (yellow trace), showing putative octamer, tetramer, and empty nanodisc. FSEC of full-length KAT1-Cterminal-GFP (blue trace) showing putative octamer and tetramer. These two samples were not subjected to any cryo-EM experiments, and are included only for the purpose of comparison. **d**, KAT1em cryoEM workflow. Details given in methods section.

Cryo-EM structure determination of KAT1em

An outline of the structure determination process is shown in (**Fig. 2-4**). The structure of KAT1em in gentle detergent digitonin was determined by cryo-EM at a nominal resolution of 3.5 Å in the transmembrane domain (**Figs. 2-4 and 2-5**). Focused refinements of a single tetramer, and then further focused refinements of the TMD of a single tetramer, were important in improving map in the transmembrane helices (**Fig. 2-4**). Map quality supported *de novo* model building (**Fig. 2-5**). Refined atomic models show good agreement with the density and good stereochemistry (**Fig. 2-4** and **Table 1**).

Figure 2-5

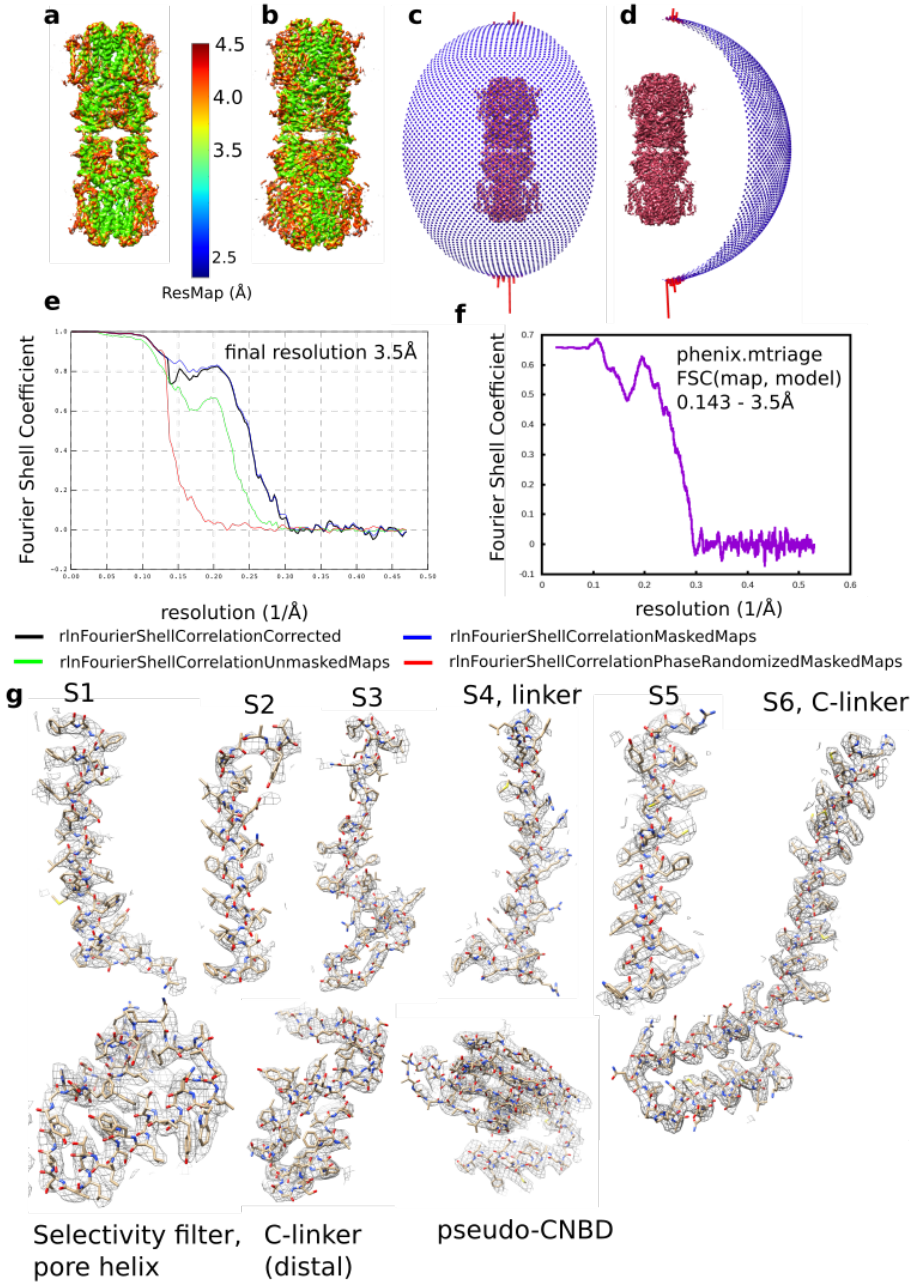

Figure 2-5: Cryo-EM map and model validation

a, ResMap coloring of unfiltered half map of full molecule **b,** Same ResMap coloring in **a** on sharpened full molecule map. **c,d,** 90° rotated angular distribution plots for refined full molecule. **e,** FSC plot for transmembrane region focused map. FSC 0.143 criterion is used for resolution determination (Rosenthal and Henderson 2003). **f,** FSC(map, model) plot from phenix.mtriage (Afonine et al. 2018a), indicating correspondence of tetramer atomic model to TMD-focused-refined density map. **g**, Sharpened cryo-EM density map is shown with fitted atomic model.

Table 1-1: Cryo-EM and model building statistics

Data Collection	
Microscope	Titan Krios
Voltage (kV)	300
Detector	K2 Summit
Nominal defocus range (μm)	-1 to -2.5
Super-resolution pixel size (Å)	0.532
Nominal total electron dose (e-/Å^2)	50
Exposure time (s)	12
Number of images	1502
Reconstruction (Relion 2)	
Picked particle number	124,211
Final particle number	91,689
Full molecule resolution (masked, Å)	3.8
Transmembrane resolution (masked, Å)	3.5
Map sharpening B-factor	-134
Model Refinement (Phenix)	
Refinement resolution limit (Å)	3.5
FSC(map, model) = 0.143 (Å)	3.50
RMS deviations	
Bond length (Å)	0.0104
Bond Angle (°)	1.35
Ramachandran plot	
Favored (%)	90.27
Allowed (%)	9.50
Outlier (%)	0.23
Validation	
MolProbity score	1.70
Clashscore	3.64
EMRinger score (tetramer model, full map)	2.01
EMRinger score (TMD-Clinker model: residues 50-342, TMD map)	2.28

Architecture of *Arabidopsis thaliana* KAT1

KAT1em assembles as a dimer of non-domain-swapped tetramers. The details of the octamer interface will be discussed later, as the physiological importance, if any, of the octamer is unknown. KAT1 adopts the non-domain-swapped architecture of the CNBD-containing subfamily. Each subunit contains a four helical bundle VSD, a pore domain component, a C-linker (an alpha-helical hairpin extension off of the S6 pore-lining helix), and finally a pseudo-CNDB (**Fig. 2-6**). Each of these components of KAT1 will now be described, and their contribution to channel activation discussed.

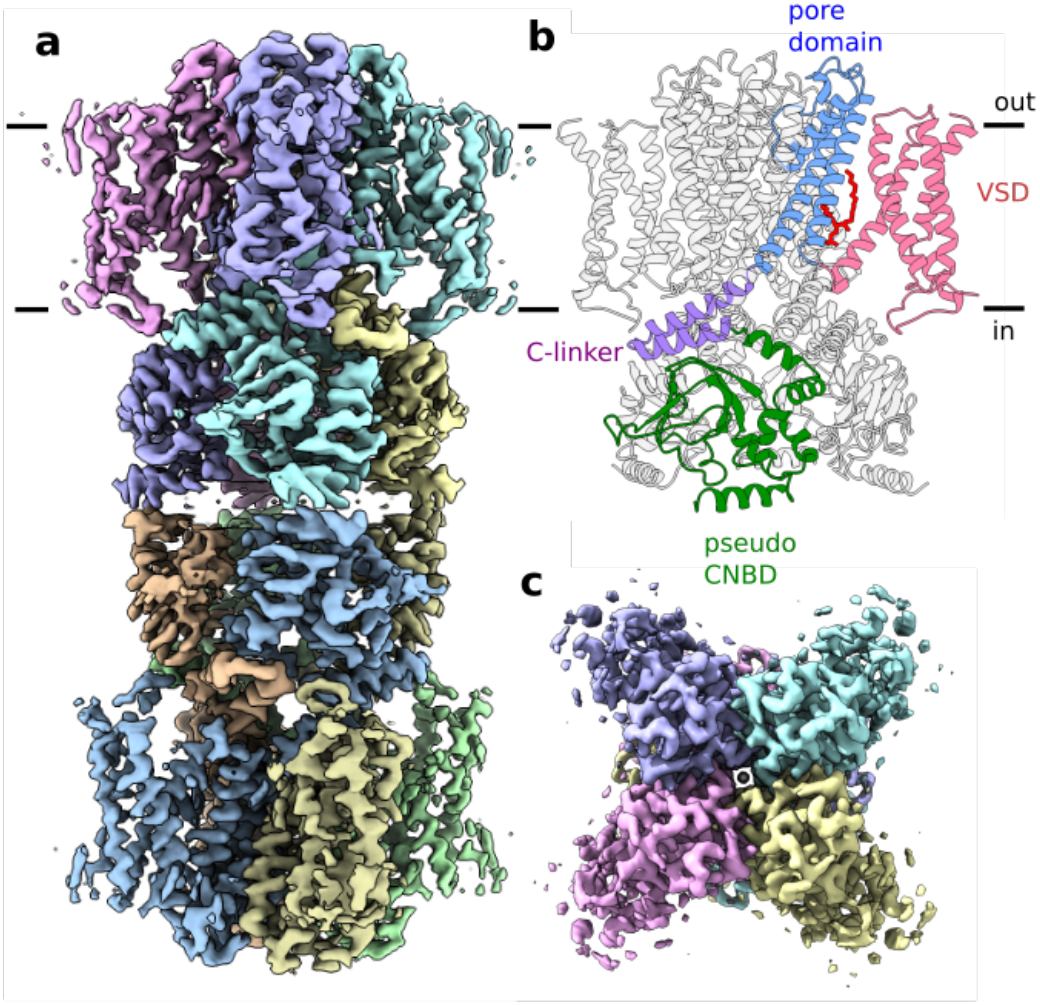

Figure 2-6: Architecture of *Arabidopsis thaliana* KAT1em.

a, Sharpened cryo-EM density map of channel octamer, side view. **b,** Ribbon model of KAT1em, with domains labeled. Phospholipid is shown in red. **c**, Top view of sharpened cryo-EM density.

KAT1em displays a canonical K^+ selectivity filter, a closed inner gate, and a small central cavity

KAT1 has negligible open probability at zero mV when recorded in Xenopus oocytes (**Fig. 2-2**) (Hoshi 1995). Additionally, in the presence of millimolar K^+ (the conditions of our functional and structural experiments), KAT1 does not undergo C-type inactivation (a rearrangement of the selectivity filter seen in some channels which renders the channel nonconductive) (Hurst et al., 2005; Moroni et al., 2000). Thus, we expect that at 0 mV the inner gate of KAT1em should be closed and the selectivity filter in a conductive conformation. Indeed, the structure of the KAT1em selectivity filter (TTGYG, **Fig. 2-7b**), appears to be very similar to that of non-inactivated KcsA (PDB ID: 1K4C) with a backbone RMSD of ~0.32 Å (Zhou et al., 2001), with the caveat that at our current resolution, we might be unable to detect subtle backbone reorientations of the glycines. Future lines of inquiry may be directed towards determining why KAT1 does not inactivate. One possibility is the presence of a robust network of hydrogen bonds that may stabilize the conductive state of the filter, most notably between T257 and Y263 side chains.

Figure 2-7

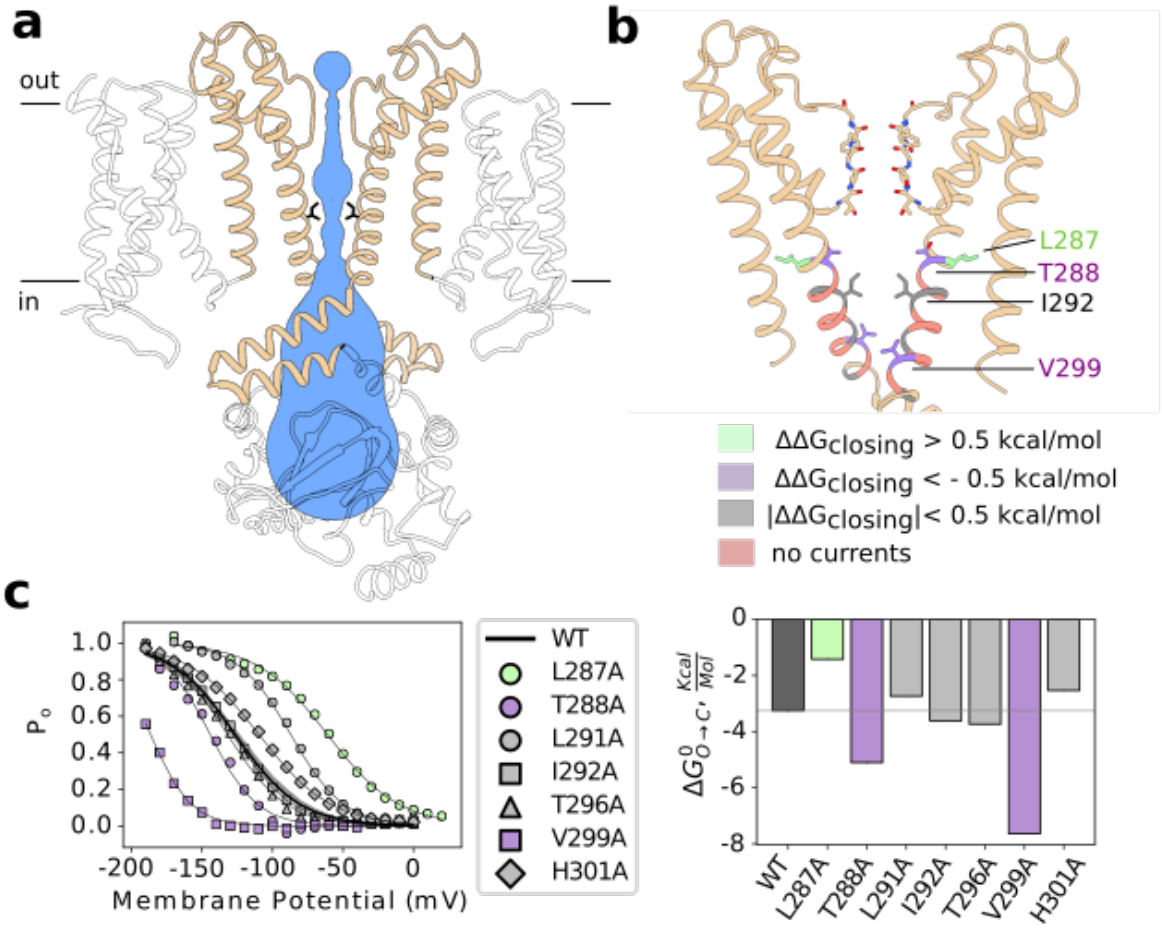

Figure 2-7: KAT1em displays a canonical K^+ selectivity filter, a closed inner gate, and a remarkably small central cavity.

a, View of pore, with only two subunits shown for clarity. Permeation pathway shown in blue, with inner gate radius calculated by MOLE (1.4 Å) or HOLE (1 Å) (Pravda et al., 2018; Smart et al., 1996). **b,** Sticks are shown for selectivity filter residues, as well as inner gate-forming residue I292, as well as key gating residues L287, T288 and V299. Residues are colored by effect of alanine mutagenesis (see legend inset). **c,** P_o-V relations of pore alanine scan. **d,** Deactivation energies of alanine mutants, calculated from P_o-V relations in (**c**), see methods. Electrophysiological data are shown as mean ± SEM.

The inner gate of KAT1em is formed by the tight constriction of hydrophobic side chains of I292 (radius 1 Å by HOLE, 1.4 Å by MOLE, **Figs. 2-7a**), which is significantly smaller than the size of a hydrated K^+ ion (3-4 Å) (Moldenhauer et al., 2016; Pravda et al., 2018; Smart et al., 1996). Strikingly, the Cα of I292 is only 12 Å from the bottom of the reentrant pore helix (T259Cα), so that the location of the KAT1 gate resembles that of HCN, 11 Å from bottom of reentrant pore helix to top of gate (V390Cα), rather than that of Eag1, about 23 Å below the pore helix. Whether this difference in gate position plays any mechanistic role is unknown, however, it does dictate the volume of the internal cavity. KAT1's inner cavity can accommodate roughly 15 water molecules, while KcsA can hold roughly 25 waters (Zhong et al., 2008): we expect KAT1 might be less susceptible to pore blockade by large organic cations than other K^+ channels. It is also conceivable that the position of the gate in the membrane may dictate the amount of mechanical advantage that the VSD might have in pushing or pulling open the gate. Based on gate position relative to the VSD, different channels might require different extents of VSD motion to open/close. In theory, the greater the distance between the gate and the point of the contact of the S4 on the pore domain, the more mechanical leverage the S4 will have and pore opening will require a smaller translational movement of S4.

To evaluate the energetics of this pore opening/closing process, we conducted a local alanine scan of the S6 bundle-crossing / gate region, spanning residues 287-301 but excluding an alanine (A289) and a glycine (G293) (**Fig. 2-7**). Six mutants failed to give currents: Y290A, N294A, M295A, N297A, L298A and V300A, pointing to the possible importance of these side chains in tetramer folding and stability. Seven mutants displayed a range of energetic effects: L287A, T288A, L291A, I292A, T296A, V299A, and H301A. Global analysis of these mutants is complicated by the likely existence of an additional closed state, accessed only via the open state (Zei and Aldrich, 1998), a fact that increases the difficulty of estimating the "default" state

of the pore (Yifrach and MacKinnon, 2002). Thus, we focus our discussion on individual residues displaying major energetic perturbations. On one side, L287A which packs against the S5 helix promotes channel opening. S5-S6 packing interactions have been proposed to stabilize the closed state of the HCN channel (Lee and MacKinnon, 2017) and the potential reduction in van der Waals packing at this position might facilitate gate opening. In contrast, V299A (at the intracellular end of the helical bundle gate, nestled against the neighboring S6) as well as T288A (towards the middle of S6), promote channel closure (**Fig. 2-7**). Together these results suggest reorganization of S5-S6 and S6-S6 inter-helical packing upon channel activation-deactivation. So far, similar results might be expected for the pore of a depolarization-activated ion channel.

The VSD of KAT1em is in an 'up' conformation

KAT1em VSDs are arranged as 4 helix bundles, each with a centrally located hydrophobic gasket (or plug) formed by the side chains of F102 and V70 (**Figs. 2-8a,b**). The S4 helix, which is known to reorient in response to changes in membrane potential (Latorre et al., 2003) is alpha helical at its N and C termini, but adopts a 3-10 geometry for 3 turns in the region spanning the gasket. S4 arginines R0 (165), R1 (171) and R2 (174) are positioned above the gasket, while R3 (176), R4 (177), and R5 (184) are located below the gasket (**Figs. 2-8a,b**). Classical VSDs contain a series of negative countercharges (Asp or Glu residue) forming electrostatic pairs with S4 arginines within the focused electric field (Palovcak et al., 2014; Vargas et al., 2012). However in KAT1em, the putative primary sensing charge, R2, appears to interact instead with N99. Mutational analysis of N99A and N99D indicates that this asparagine, working as a 'counter-dipole', is as functionally effective as a *bona fide* counter charge (**Fig. 2-8c**).

Figure 2-8

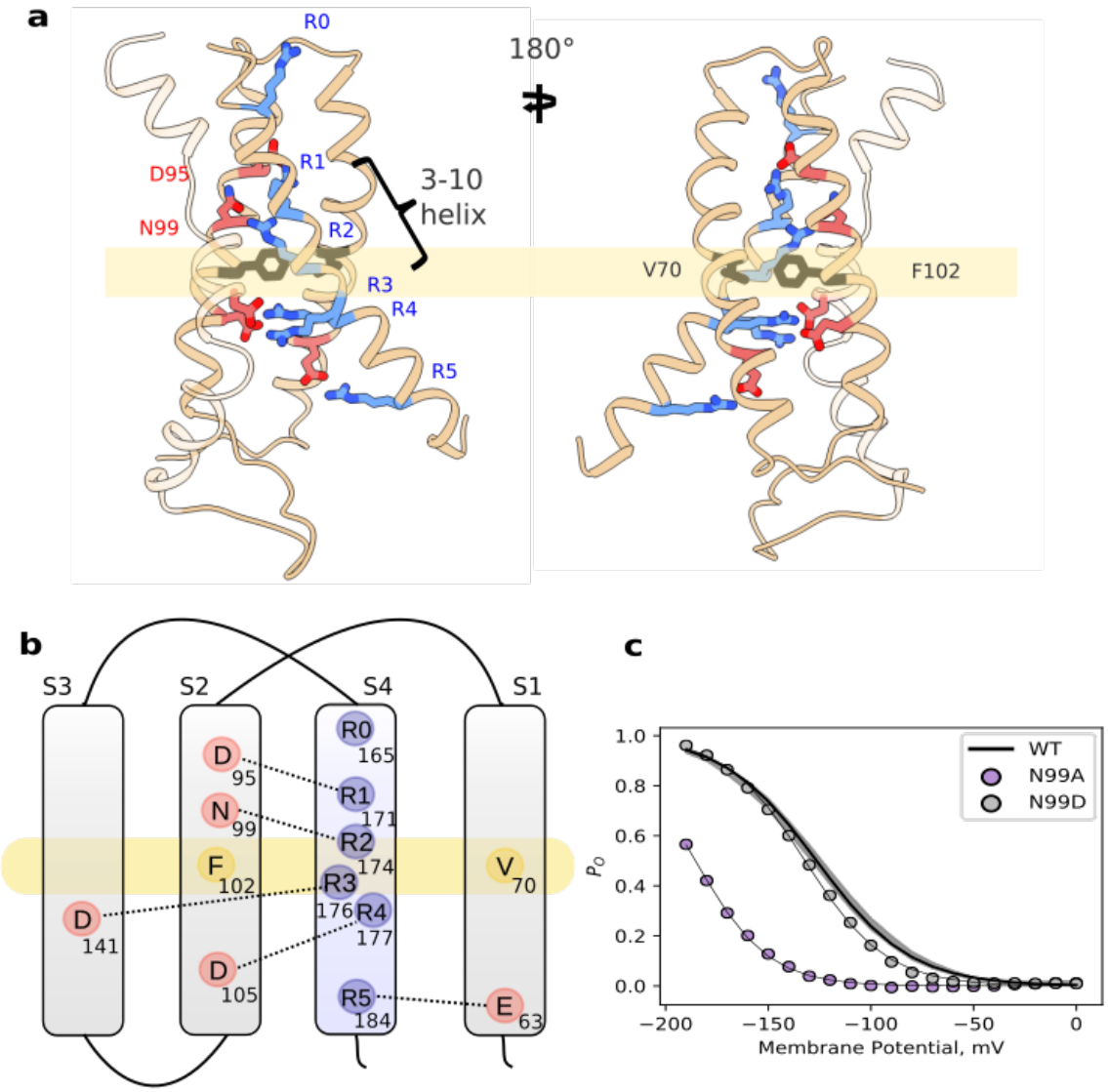

Figure 2-8: The voltage sensing domain of KAT1em is in an 'up' conformation.

a, Rotated views of KAT1em VSD. Stick side chains are shown for the hydrophobic gasket: F102 and V70, for key residues on S4: R165 (R0), R171 (R1), R174 (R2), R176 (R3), R177 (R4), R184 (R5), and for counter-charges/dipoles: E63, D95, N99, D105, D141. **b,** Diagram of key VSD features, showing hydrophobic gasket (F102 and V70, yellow) as well as all S4 charges (blue) and distributed countercharges / counter-dipoles (red). **c,** Electrophysiology of N99D/A mutants. N99A is severely left-shifted, yet N99D has little effect, indicating that N99 is effective as a counter-dipole.

We have assigned the observed KAT1em VSD conformation as 'up' (activated) based on three main lines of evidence. First, neutralization of R4 (R177), immediately below the hydrophobic gasket, does not affect the estimated gating charge (Zei and Aldrich, 1998). Thus, by the process of elimination, the sensing arginines are most likely above the gasket in the present structure and thus, in the 'up' state. Consequently, we expect that R2 (R174) is the primary sensing charge, with R1 (R171) possibly contributing partially to charge transfer, consistent with an effective z of ~0.75 e per sensor as estimated by limiting slope analysis (Latorre et al., 2003). Neutralizing either charge (R174Q or R171Q) generates non-functional channels, though at the moment we cannot eliminate potential trafficking or lack of expression issues (data not shown). The second line of evidence is the observation of a closed intracellular gate in the pore domain of KAT1em, which, based on functional studies, should be coupled to an 'up' VSD (Latorre et al., 2003). Finally, our double mutant cycle data (described in the next section) suggest that R0 (R165) is more strongly coupled to D95 in the 'down' state than in the 'up' state. The present KAT1em structure shows R0 (R165) clearly above D95 (Cα-Cα distance of ~15 Å). A downward movement of S4 by approximately 1-2 helical turns (1-2 clicks) would allow salt-bridge formation between D95 and R165.

The VSDs of KAT1em and HCN1 display two major structural differences at 0 mV. Although both VSDs are characterized by S4 segments of extraordinary length, the S4 segment of hHCN1 extends further extracellularly, while the KAT1em 3-10 region extends an additional half turn intracellularly. This additional stretch of 3-10 helix in KAT1em causes the intracellular ends of the S4 segments of the two channels to diverge: that of KAT1em being bent towards the intracellular end of the S5 (**Fig. 2-9a**). Notably, the gating charge immediately above the gasket in HCN1 (Lee and MacKinnon, 2017) is also stabilized by counter dipoles, rather than an aspartate or glutamate counter charge. In contrast, comparing the VSDs of KAT1em with those of a domain-swapped channel, like K_v1.2/2.1, reveals a more striking difference: the KAT1em

S4 extends an additional two helical turns into the cytoplasm than does the S4 of K_v1.2/2.1, which abruptly bends 90 degrees to transition to a helical S4-S5 linker (**Fig. 2-9b**).

Figure 2-9

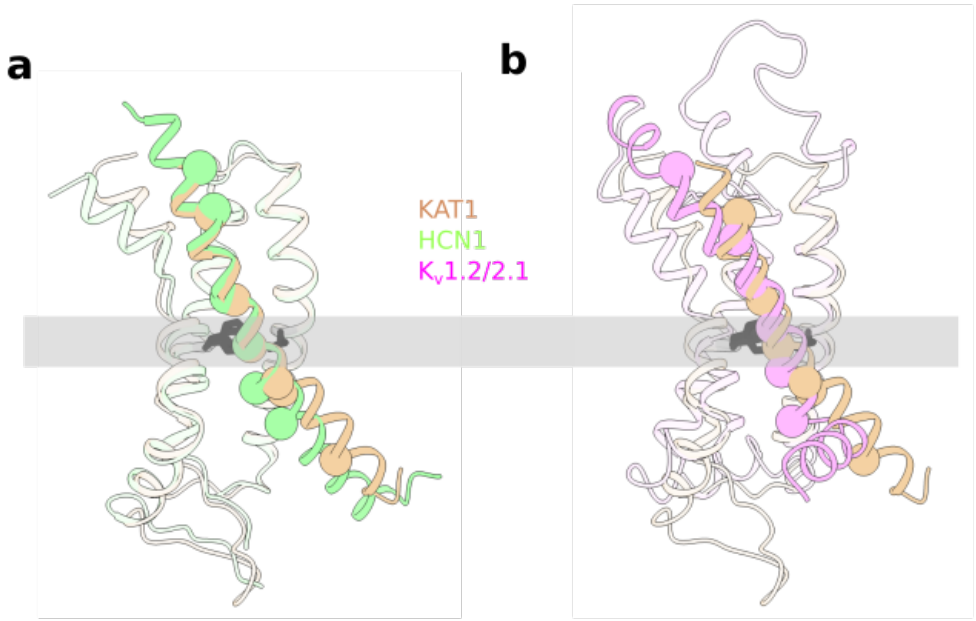

Figure 2-9: Structural comparison between voltage sensors of KAT1em, HCN1 and K_v1.2/2.1 **a,b,** Overlays of KAT1em (tan) with HCN (green, 5U6O) and K_v1.2/2.1 (pink, 2R9R), respectively, highlighting structural differences between S4 helices. Cα atoms of the positively charged residues of S4 are shown as spheres.

The KAT1 VSD-pore interfaces and reversed electromechanical coupling

KAT1em VSD and pore domains interact via two major interfaces: the first near the intracellular face of the channel (**Fig. 2-10**, right side) with the participation of S4 and S5 overlaying the C-linker of the adjacent protomer and the second near the extracellular side formed by the intercalation of S1 between S4 and S5 (**Fig. 2-10**, left side). We first directed our attention to the intracellular S4-S5-C-linker triad as a key structural determinant of reversed electromechanical coupling (**Fig. 2-11**). The interactions between S4, S5, and the C-linker are mediated by the extended length of the KAT1em S4, which extends an extra half turn further into the cytoplasm than does the S4 of depolarization-activated Eag1. The S4 and S5 helices are connected by a short loop-like linker showing well-ordered backbone density in the cryo-EM map (**Fig. 2-5**). The intracellular ends of the S4 and S5 helices are well packed against each other, with several hydrophobic contacts (F182, L185 and I196) and potential charge-charge interactions (K187, K200, R197, E186, D188) forming this surface. The intracellular ends of the S4 and S5 helices come to rest on top of the C-linker. One of the most striking contacts is made by the side chain of R310 from the C-linker, which in an extended rotameric conformation snakes upwards, underneath the S4-S5 linker, to come within 4 Å of the backbone carbonyl of the S4 helix (**Fig. 2-11**). Mutations designed to disrupt this charge to helix-dipole interaction, R310K/Q/N/E/A, failed to yield currents, despite wild-type-like expression for R310K (**Figs. 2-14f,g**), supporting a critical role of R310 in electromechanical coupling. The rest of the S4-S5-C-linker interaction surface appears to be formed by van der Waals contacts, as well as potential hydrogen bonds between S5-Y193 and C-linker-T306 as well as between S5-R197 and C-linker-T303 (**Fig. 2-11**).

Figure 2-10

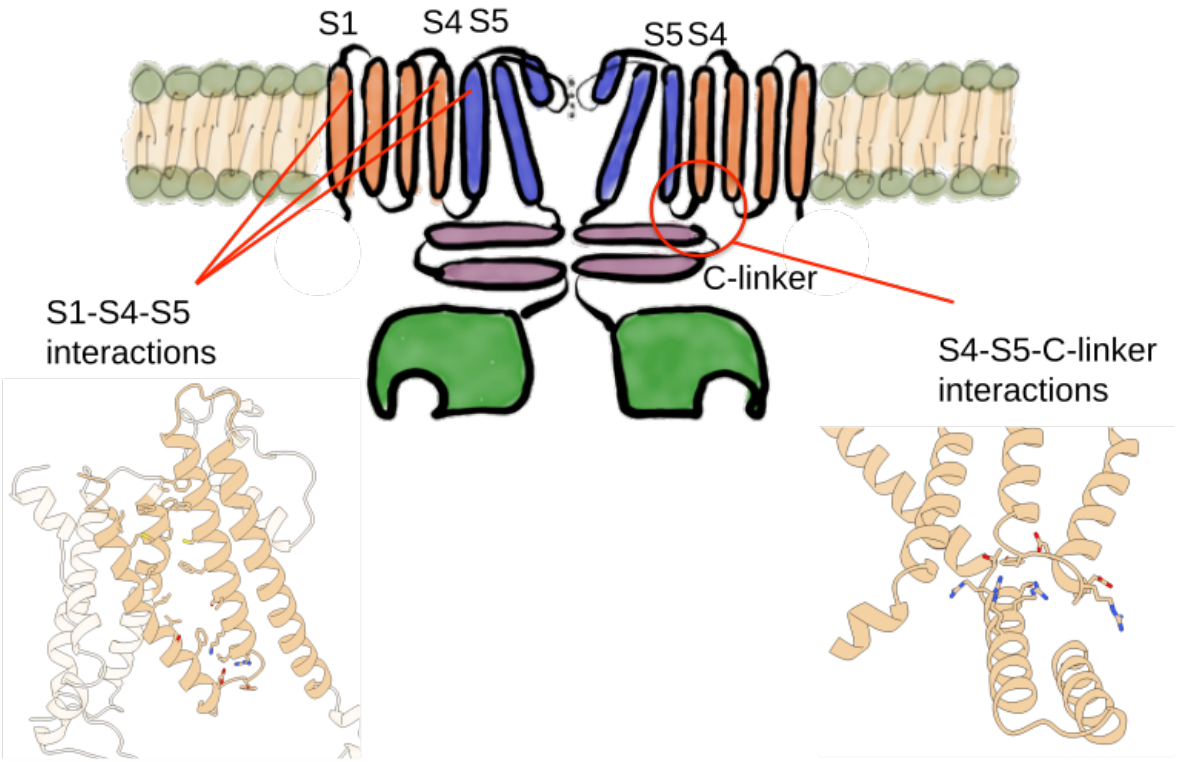

Figure 2-10: Two major interfaces between VSD and pore in KAT1

Cartoon with two subunits shown for clarity. The first (lower, inner) interface is diagrammed on the right, and is formed by the S4 and S5 of one subunit, contacting the C-linker of the neighboring subunit. The second (upper) interface is diagrammed on the left, and is formed by S1, S4 and S5 of the same subunit, within the plane of the membrane.

Figure 2-11

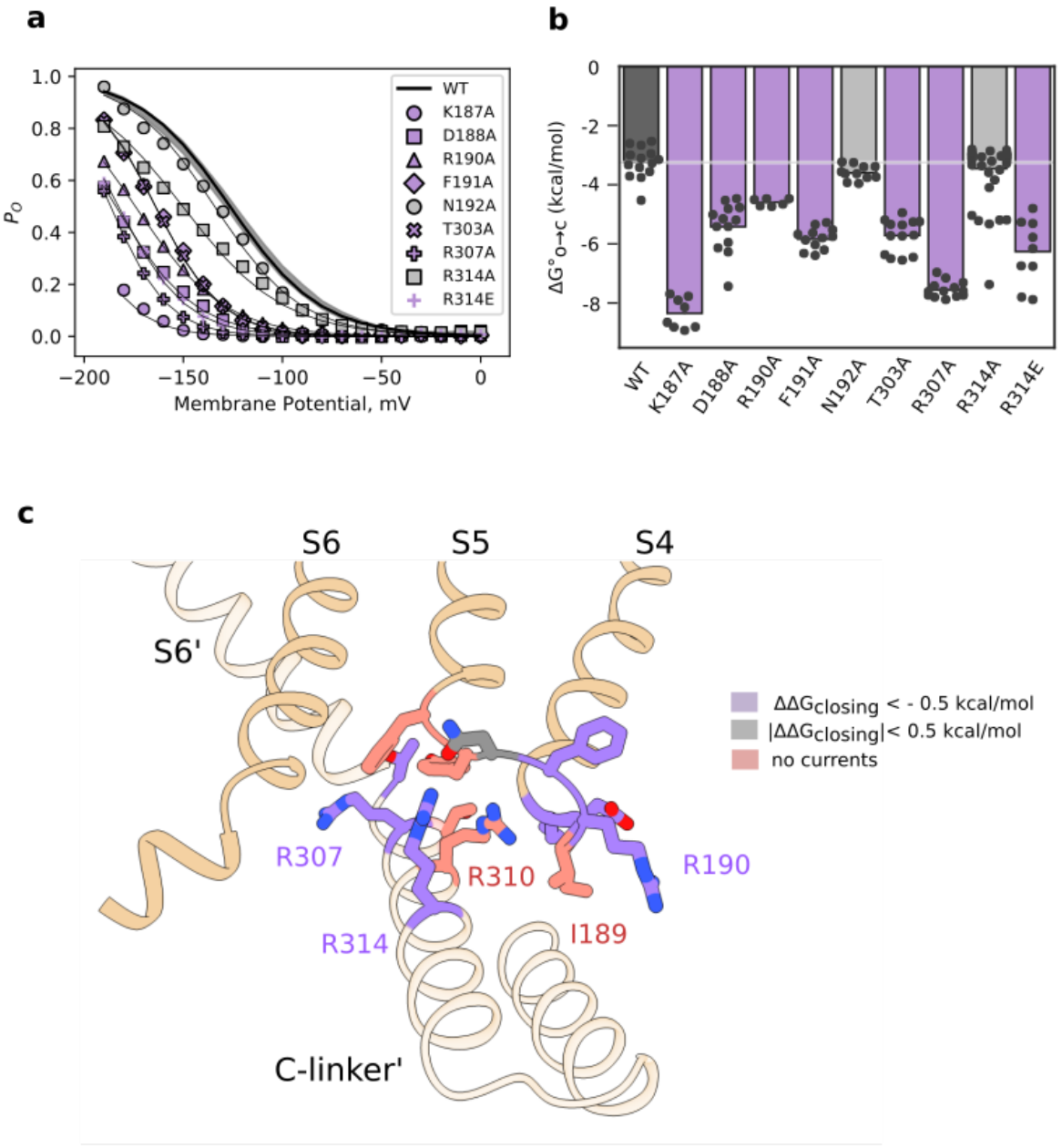

Figure 2-11: Function and structure of the KAT1 lower S4-S5-C-linker interface

a, P_o-V of S4-S5-C-linker interfacial mutants. **b,** Deactivation energies of S4-S5-C-linker interfacial mutants calculated from P_o-V relations in panel **a**. **c,** Mapping of electrophysiology data from **a** colored by the effect of mutation as indicated in legend inset. Shown as sticks are key S4-S5 linker residues: K187, D188, I189, R190, N192, Y193, F194, and key neighboring subunit C-linker residues: T306, R307, R310, R314.

Alanine scanning mutagenesis was carried out on the majority residues making productive interactions at the intracellular interface. Many mutants (I189A, Y193F/A, F194V/A, R197K/Q/A, K200Q/A, T306A, F309A, R310K/Q/N/E/A) failed to give currents (data not shown). Furthermore, all of the mutants that generated currents (K187A, D188A, R190A, F191A, N192A, T303A, R307A, R314A/E) were more difficult to open (**Figs. 2-11a,b**). We interpret these results within a framework where mutations designed to disrupt or weaken coupling make the channel harder to open, i.e. as more energy is required for channel opening, the mid-points of activation shift towards more negative potentials. These results in KAT1 parallel those described in the depolarization-activated Shaker channel: alanine mutants at the VSD-pore interface (Soler-Llavina et al., 2006), as well as the ILT mutant (Ledwell and Aldrich, 1999) yield channels with right-shifted G-V relations, corresponding to channels with a compromised electromechanical coupling (in both cases, the Shaker VSDs are still functional). In Shaker, these results, in combination with explicit assessments of VSD/pore coupling energetics (Yifrach and MacKinnon, 2002), support a model in which the "default" state of the Shaker pore is the closed conformation (Blunck and Batulan, 2012). This implies that the likely role of the VSDs in the depolarization-activated K^+ channels is to perform work to open the pore domain, which in the absence of a bias by the VSD exists in a closed conformation. Based on our VSD-pore interfacial mutagenesis, we propose that the "default" state of the KAT1 pore is also a closed conformation. In this case, a downward/inward movement of the S4 segment is required to stabilize the open state of the pore at negative potentials.

At the extracellular interface, mutagenic perturbations yielded nuanced effects on the VSD/pore coupling energetics. The side chain of F83 on S1, conserved in hERG, rnEag, hHCN1, ceTax-4, and KAT1, intercalates into a hydrophobic crevasse formed by Y217 on S5 and Y247 on the pore helix (**Fig. 2-12**). Mutants F83A and F83L failed to yield any detectable currents (data not shown), indicating an important role for residues at this interface in channel expression,

trafficking, or activation. This result parallels those in the domain-swapped K_v family, demonstrating the necessity of (at least) two points of contact between VSD and pore domain (Lee et al., 2009). Additionally, the extracellular ends of S1, S4, and S5 form productive interactions; the side chain of S1 residue F81 intercalates between the upper ends of the S4 and S5 helices. This is a significant structural divergence from hHCN1, in which the upper ends of the S4 and S5 helices interact directly, forming zipper-like interactions (**Fig. 2-13**). Mutation of F81 to alanine makes the channel slightly harder to open while mutation to leucine has no effect on channel opening/closing (**Fig. 2-12**). In general, perturbing the upper interface had mixed and mild effects. These mutants led to three distinct phenotypes: nonfunctional channels (L172A, F207A, C211A), wild-type behavior (I166A, F215A), or channels that are slightly harder to open (F81A, V178A). We conclude that the upper S1-S4-S5 interface is likely crucial for channel structure (due to the several mutants abrogating current), yet might not represent the major pathway of energy transfer from VSD to pore.

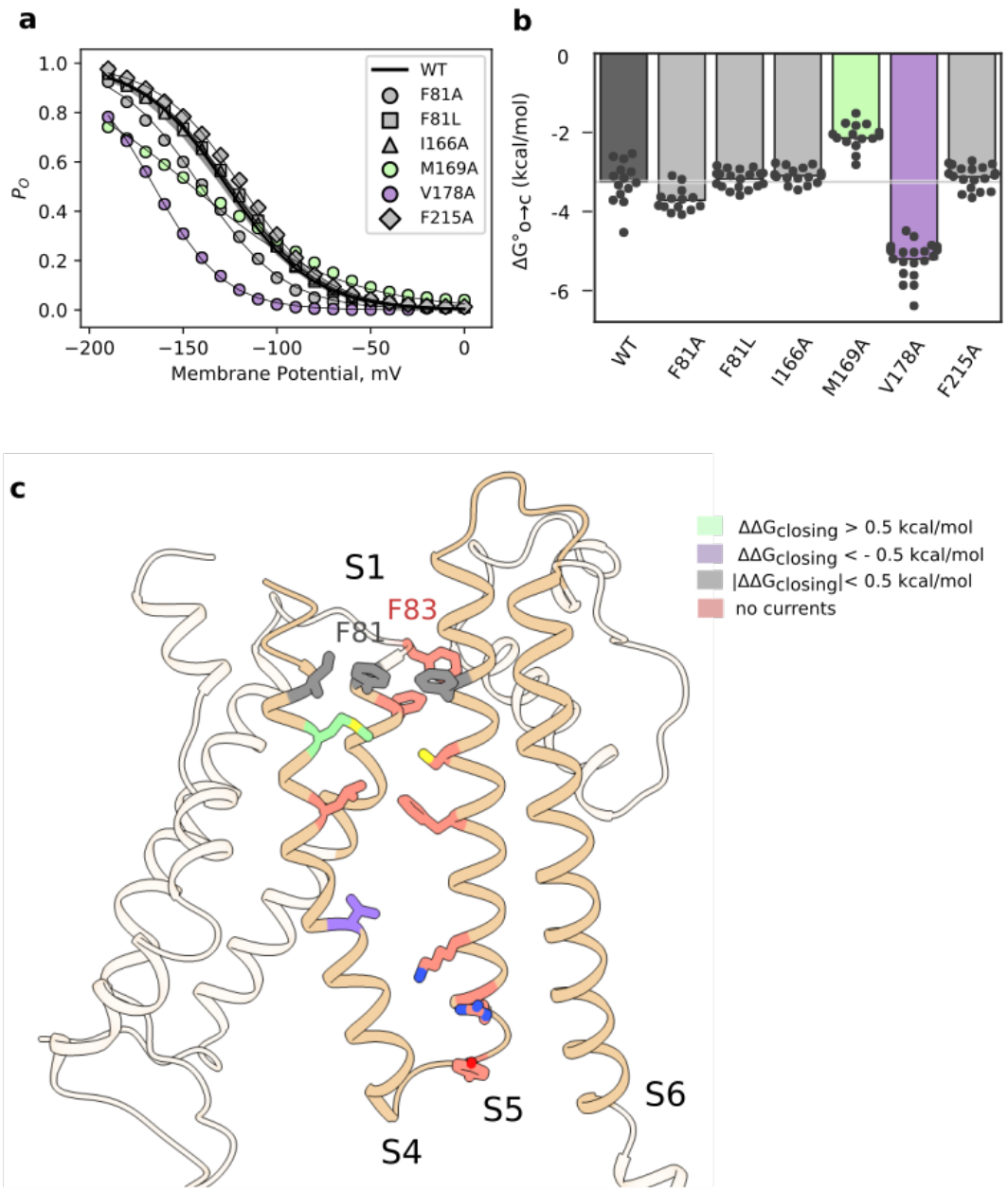

Figure 2-12: Function and structure of the KAT1 upper S1-S4-S5 interface

a, P_o-V relations of upper interface mutants. **b**, Deactivation energies of S4-S5-C-linker interfacial mutants calculated from P_o-V relations in panel **a**. **c**, Mapping of electrophysiology data from **a** colored by the effect of mutation as indicated in legend inset. Displayed as sticks are key residues on S1: F80, F81, F83, key S4 residues: I166, M169, L172, V178, and key S5 residues: Y193, R197, K200, F207, C211, F215.

Figure 2-13

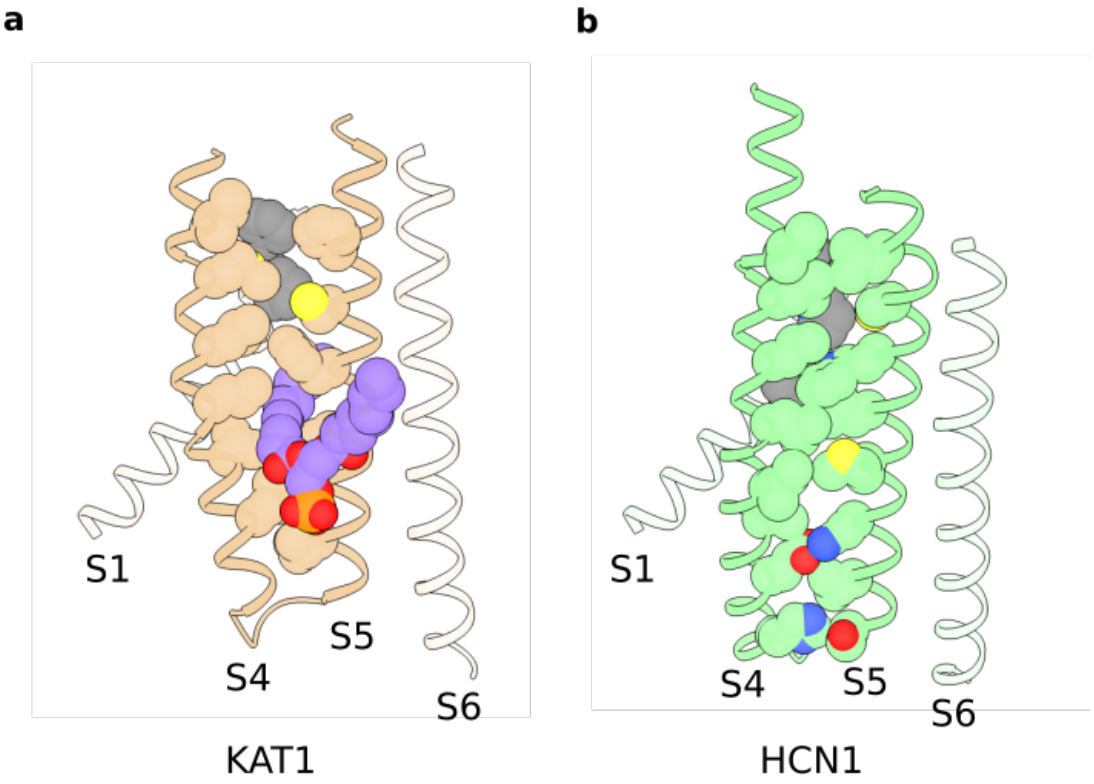

Figure 2-13: Different S4-S5 VSD-pore packing in KAT1 and HCN1

a, KAT1 upper interface (S1, S4, S5) residue packing shown as spheres. Bound phospholipid in the hydrophobic window is shown in purple. **b,** Upper interface of HCN1 (5U6O), shown in analogous view to **a**.

Between the upper and lower interfaces, we find an opening, or “hydrophobic window” between the VSD and pore. This cavity is filled with a tubular density (**Fig. 2-14**), which we have putatively assigned as a phospholipid, despite a final purification step in detergent. One alkyl chain of the lipid snakes through a hydrophobic window formed by the S1, S4, and S5 helices, making extensive van der Waals contacts along its length. The phosphate head group is coordinated via charge-charge and hydrogen-bonding interactions by R197 and K200 on S5 (N-O heteroatom distance of 2.5 Å and 3.5 Å for R197 and K200, respectively) and Y290 on S6 (O-O heteroatom distance 2.5 Å). All mutations introduced to the lipid-coordinating residues (R197K/Q/A, K200Q/A, Y290F/A) abrogated currents (data not shown), despite the fact that R197K and K200Q mutants expressed at near-wild-type levels (**Figs. 2-14f,g**), suggesting a structural or critical functional role for the bound lipid. Furthermore, during the course of a ~3.5 μs MD simulation in which a lipid-less KAT1 was initially placed in a POPC bilayer, lipid molecules from the bulk stably occupied remarkably similar binding poses to that seen in the cryo-EM structure (**Figs. 2-14c,d**). In all four subunits, the phosphate head group is in close proximity to R197, K200, and Y290. In three of four subunits, an alkyl tail of the lipid snakes through the hydrophobic window between S4 and S5. Additional experiments (such as measurement of gating currents from lipid-binding site mutants) will be required to assess the possibility that the bound lipid plays a functional role. However, given the critical placement of the lipid at the functionally important S4-S5-S6 interface, this bound lipid may well be a component of the gating machinery. Moreover, the presence of this lipid is a marked structural departure between KAT1 and HCN1 (**Fig. 2-12**). KAT1 and other plasma membrane plant K_v channels are strongly modulated by PIP_2 via an unknown mechanism (Liu et al. 2005) and this bound lipid may indicate a binding site of PIP_2. Given the placement of this binding site at the functionally critical S4-S5-S6 interface, the bound lipid may well constitute an integral component of the gating machinery. In addition, KAT1 is known to open remarkably slowly: the time constants for gating and ionic currents are separated by approximately three orders of

magnitude (gating current and ionic current activation time constants of ~270 μs and ~120 ms, respectively) (Latorre et al. 2003). A requirement for lipid binding (**Fig. 2-14**) or reorientation upon gating is a speculative, yet testable hypothesis to explain this kinetic disparity.

Figure 2-14

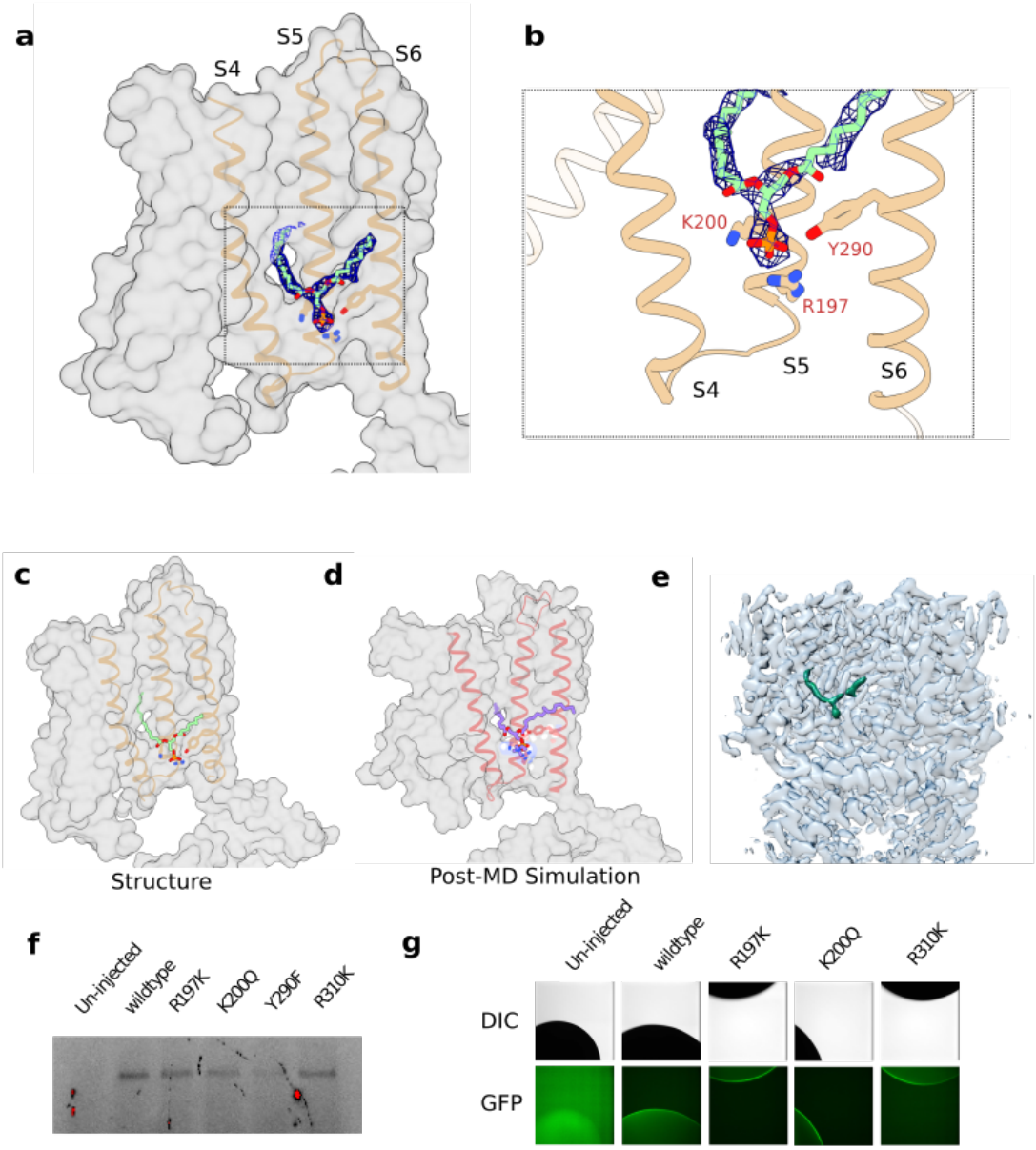

Figure 2-14: A bound phospholipid intercalated between the KAT1 VSD and pore **a,** Surface depiction of putative bound phospholipid density intercalated in the "hydrophobic window" between S4 and S5. **b,** Inset shows lipid head group coordinated by R197, K200, and Y290. **c,d** Comparison of similar lipid binding poses observed in the structure (**c**) and after ~3.5 μs MD simulation (**d**). **e,** Cryo-EM density map, with one bound lipid colored green, contoured at the same contour level as the full map. **f,** SDS-PAGE GFP in-gel imaging result of Xenopus oocyte membrane fractions, extracted in gentle detergent (see methods). **g,** Confocal imaging of Xenopus oocyte animal poles expressing various GFP-tagged constructs.

One striking aspect of KAT1 VSD-pore and lipid-binding residues is their extreme sensitivity to mutation. Despite making the most conservative mutations possible (R to K, for example), current is abrogated. It is worth considering why. Trivial reasons might include abrogation of channel expression, folding/tetramerization, or trafficking to the plasma membrane. At least one of these is likely at play with Y290F, where expression is extremely low when analyzed by GFP-SDS-PAGE (**Fig. 2-14f**). Far more interesting is the possibility that some mutations, which are expressed and trafficked (**Fig. 2-14f,g**), might have an activation threshold that is so negative (left-shifted) that it is outside of our measurement window, thus leading to a loss of function (LOF) phenotype. To assess this possibility, we can make use of the fact that KAT1 is tetrameric, and conduct a classic experiment in which different variant RNAs are mixed. Specifically, we mix RNAs encoding a gain of function (GOF) mutant, with RNAs encoding LOF variants, at near one-to-one ratios. The result will be a distribution of hetero-tetrameric channels in the oocyte membrane, centered around 2:2 stoichiometry (assuming the expression/trafficking of LOF and GOF variants are similar). In the case that the LOF variant is completely incompatible with function, in any configuration/stoichiometry, it will act as a dominant negative, “poisoning” the activity of the GOF channels. Thus, the expected result will be expression of a lower level of GOF channels, which will still have identical biophysical characteristics (eg activation midpoint) to a purely injected/expressed GOF channel. If, however, the GOF and LOF variants co-assemble and traffic, one expects channels to be formed with biophysical characteristics intermediate between the isolate LOF and isolated GOF channels. Indeed this is what we observe with co-injection experiments using several key LOF variants (**Fig. 2-15**).

Figure 2-15

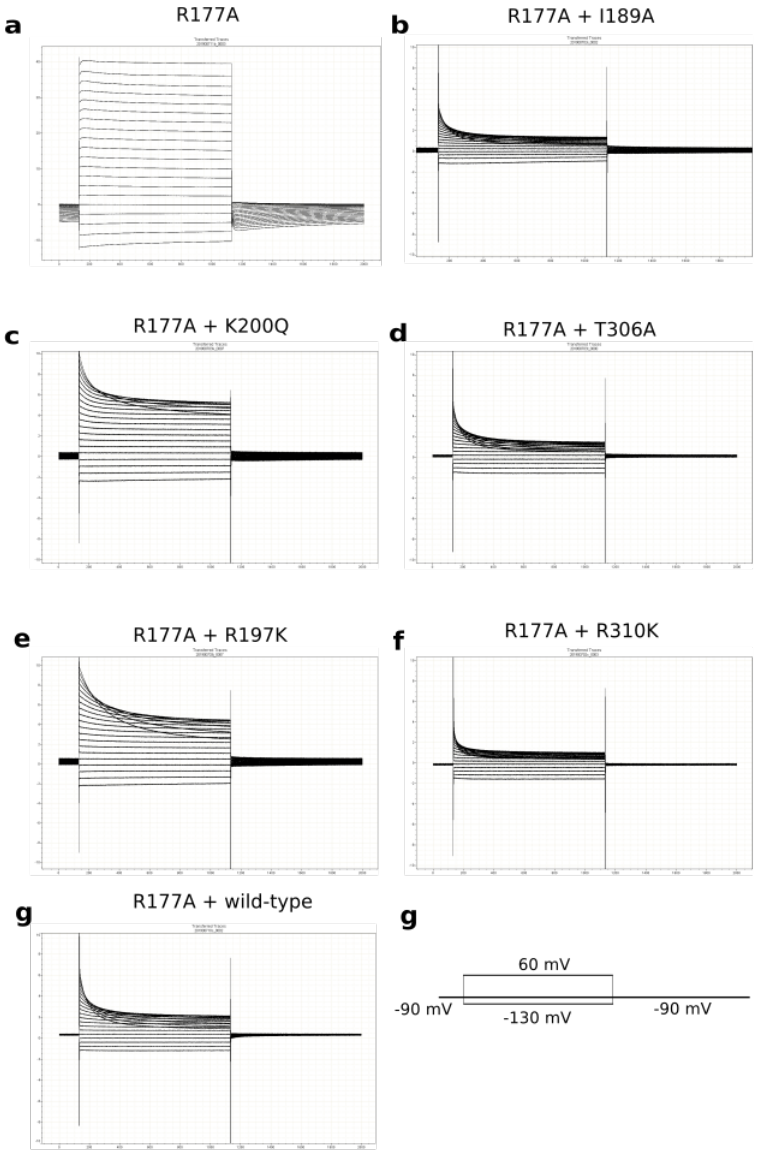

Figure 2-15: RNA mixing experiment to assess mutant trafficking and channel assembly.
a, Raw current trace for gain of function mutant R177A, showing a constitutively open channel, with current reaching a zero value at the K^+ reversal potential of -90 mV. **b-g,** Raw current traces derived from co-injected RNA mixtures of R177A plus loss of function mutants. Loss of function mutants gave no current themselves, but upon co-injection yield channels of an intermediate phenotype. **c,** Pulse protocol used during experiment.

Intriguingly, in HCN channels, the C-linker and CNBD can be deleted, and the channel still activates upon hyperpolarization (Wainger et al. 2001), while in the case of KAT1, even conservative mutations like R310K in the C-linker abrogate channel activity. The S4-S5 zipper-like interactions have been posited as a mechanism for VSD-pore coupling in C-linker-less HCN channels (Lee and MacKinnon 2017), and may indicate a departure between KAT1 in terms of the structural mechanism of VSD-pore coupling (**Fig. 2-13**). Now, with a better understanding of the physical relationship between the VSD and pore of KAT1, we sought to determine the nature and extent of KAT1 VSD motion upon hyperpolarization, as a next step in understanding VSD-pore coupling.

A 'down' state model for the KAT1 VSD based on double mutant cycle analysis and molecular dynamics simulations

We sought to combine structure-based evidence of charge-countercharge pairing and electrophysiological estimates of total charge movement with additional experimental constraints in order to construct a hypothetical 'down' state model, which in turn can guide future experiments. We employed double mutant cycle analysis (Carter et al., 1984), previously used in a similar way in NaChBac and H_v1 (Chamberlin et al., 2013; Yarov-Yarovoy et al., 2012). The extent of non-additivity in a double mutant cycle (**Fig. 2-16**) corresponds to the $\Delta G_{nonadditive}$, between various putatively interacting residue pairs (see methods section). Additionally, the sign of $\Delta G_{nonadditive}$ indicates the direction of the state dependence, here defined as: a positive $\Delta G_{nonadditive}$ points to a stronger residue-residue coupling in the 'up' state relative to the 'down' state, while a negative $\Delta G_{nonadditive}$ suggests the opposite directionality. The KAT1 'up' state VSD structure points to a number of residue interactions that could dynamically change upon hyperpolarization, particularly those charge-countercharge interactions that underlie voltage-dependent gating in VSDs (Bezanilla, 2008; Vargas et al., 2012).

Figure 2-16

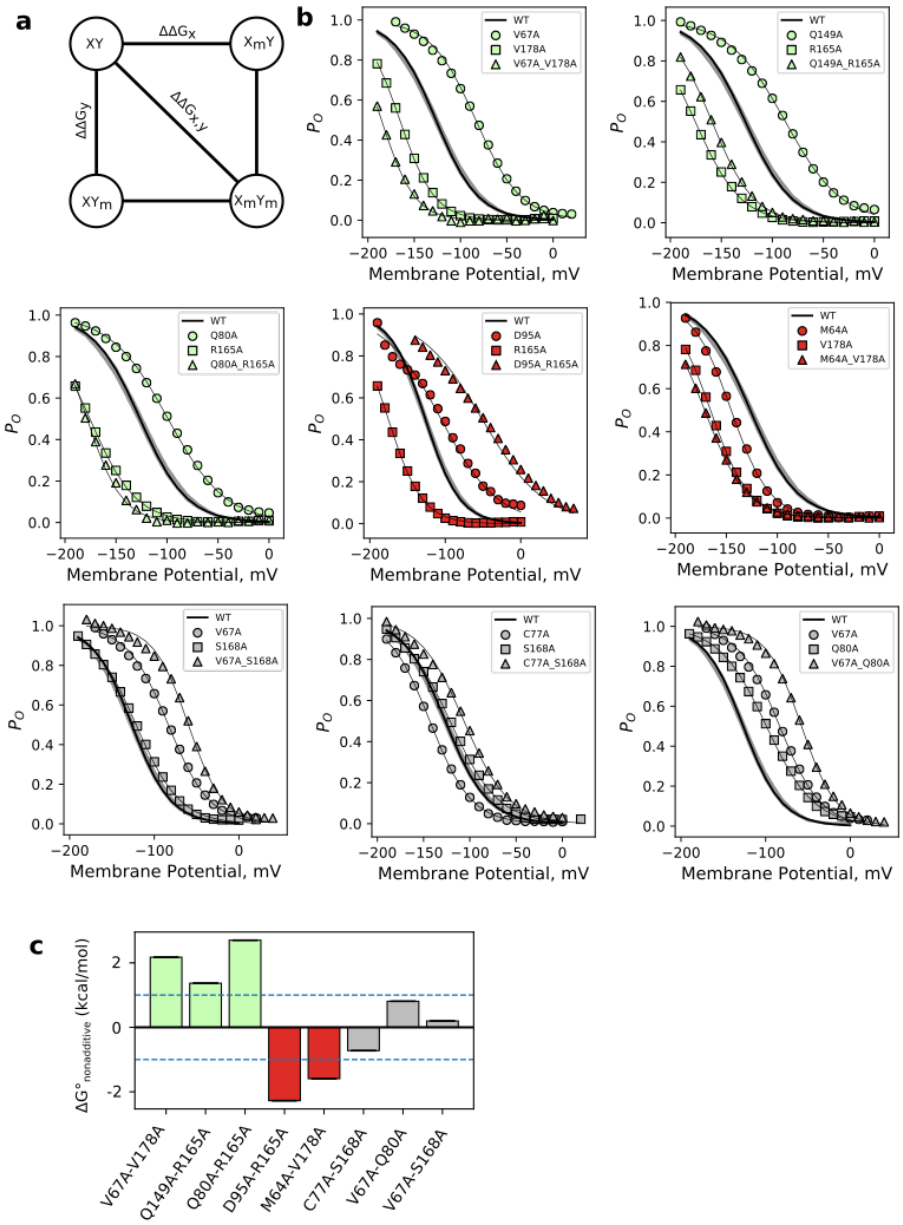

Figure 2-16: Double mutant cycle analysis of the KAT1 VSD

a, Schematic of double mutant cycle analysis. The difference between $\Delta\Delta G_{x,y}$ and the quantity ($\Delta\Delta G_x$ + $\Delta\Delta G_y$) determines the extent of differential interaction between residues x and y, in the up and down states. **b,** P_o-V relations for single and double mutants, illustrating residue-residue pairs displaying additivity (Gray) and non-additivity in different directions (Green, up-state-interaction and Red, down-state-interaction). **c,** Plot of nonadditive energies, with 1 kcal/mol threshold shown as dotted lines, colors scheme same as **b**. Data are shown as mean ± SEM.

To this end, we have tested the energetic interaction around the uppermost charge at position R165 (R0). Based on our results (**Figs. 2-16, 2-17**), R0 interacts more strongly with Q149 in the 'up' state than in the 'down' state, and interacts more strongly with D95 in the 'down' state than in the 'up' state. In the 'up' state structure, Q80 and Q149 both lie above D95, and both the Cα and entire side chain of R0 above Q80 and Q149. Thus, in transitioning to the 'down' state, R165 likely moves underneath Q80 and Q149 to interact with D95. This movement can be accomplished by a single turn of the helix (a 'one-click' transition). Additionally, V67 (on S1) and V178 (on S4) are more strongly coupled in the 'up' state. Structurally, V67 and V178 are well packed in the 'up' state, and a one-click downward S4 movement is sufficient to disrupt their packing, while bringing V178 into direct contact with M64. Indeed, M64 and V178 are more strongly coupled in the 'down' state.

Figure 2-17

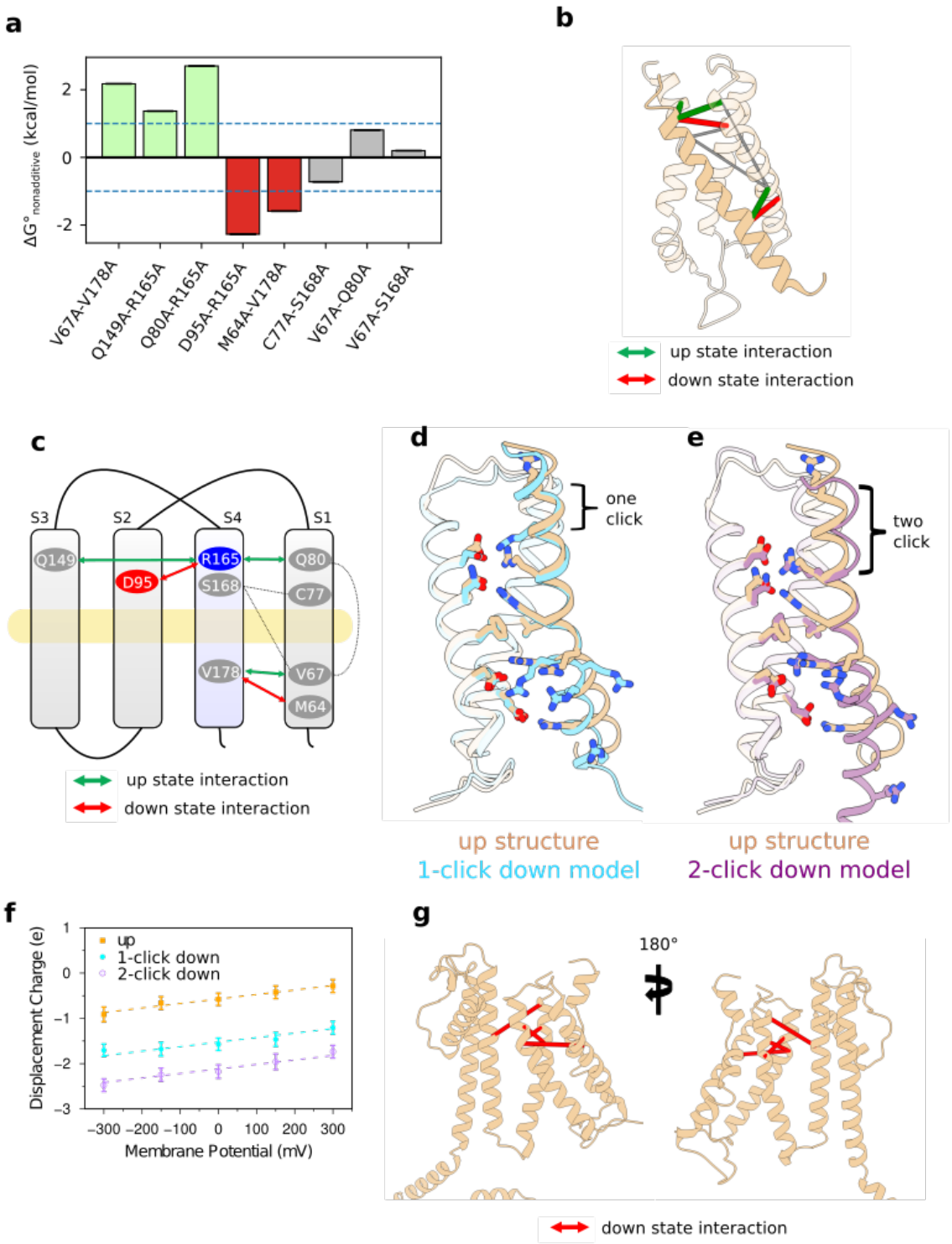

Figure 2-17: An experimentally derived model for the KAT1 VSD in the ‘down’ state.

Figure 2-17, continued.

a, Plot of nonadditive energies, with 1 kcal/mol threshold shown as dotted lines, **b,** Mapping of double mutant cycle constraints onto 'up' VSD structure. Thick Red and green lines connect Cα carbons of interacting pairs. Thin gray lines connect negative control pairs. **c,** Diagram of double mutant cycle pairs, color scheme as in **b**. **d,** One-click-down state model (blue) derived from interacting pairs and equilibrated by MD simulation. **e,** Two-click-down state model (purple) derived from interacting pairs and equilibrated by MD simulation. **f,** Displacement of charge for the isolated VSD in the up, one-click-down, and two-click-down conformations at different transmembrane potentials. Shown are the mean values and standard deviations calculated using the last 40 ns snapshots of 50 ns trajectories. The gating charge is then calculated as the offset constant between the linear fits, resulting in a gating charge of 1.02 e and 0.55 e between the up and one-click down, and one-click down and two-click down states, respectively. **g**, Mapping of literature Kat1 down state interacting pairs (Grabe et al. 2007) onto 'up' structure. Thick red lines connect Cα carbons of interacting pairs.

Next, we conducted metal bridge formation experiments to provide a mutant-cycle-independent assessment of 'down' state interactions. Fortuitously, KAT1 contains an endogenous cysteine (C77) near the extracellular end of its S1 segment. We reasoned that, given the proximity of C77 to residues on S4, we might be able to form cysteine-Cd^{2+}-cysteine cross-bridges between C77 and cysteine mutants on S4. Thus, we tested the ability of R165C (R0) to interact with C77 in a Cd^{2+}-dependent manner, as our double mutant cycle analysis suggested that R0 underwent a conformational change of ~5-10 Å upon membrane hyperpolarization. Indeed, R165C shows a Cd2+-dependent interaction with C77 which, when engaged hinders channel closing / facilitates channel opening (**Fig. 2-18**). A one-click-down motion of the S4 would minimize the Ca-Ca distance between C77 and R165.

Figure 2-18

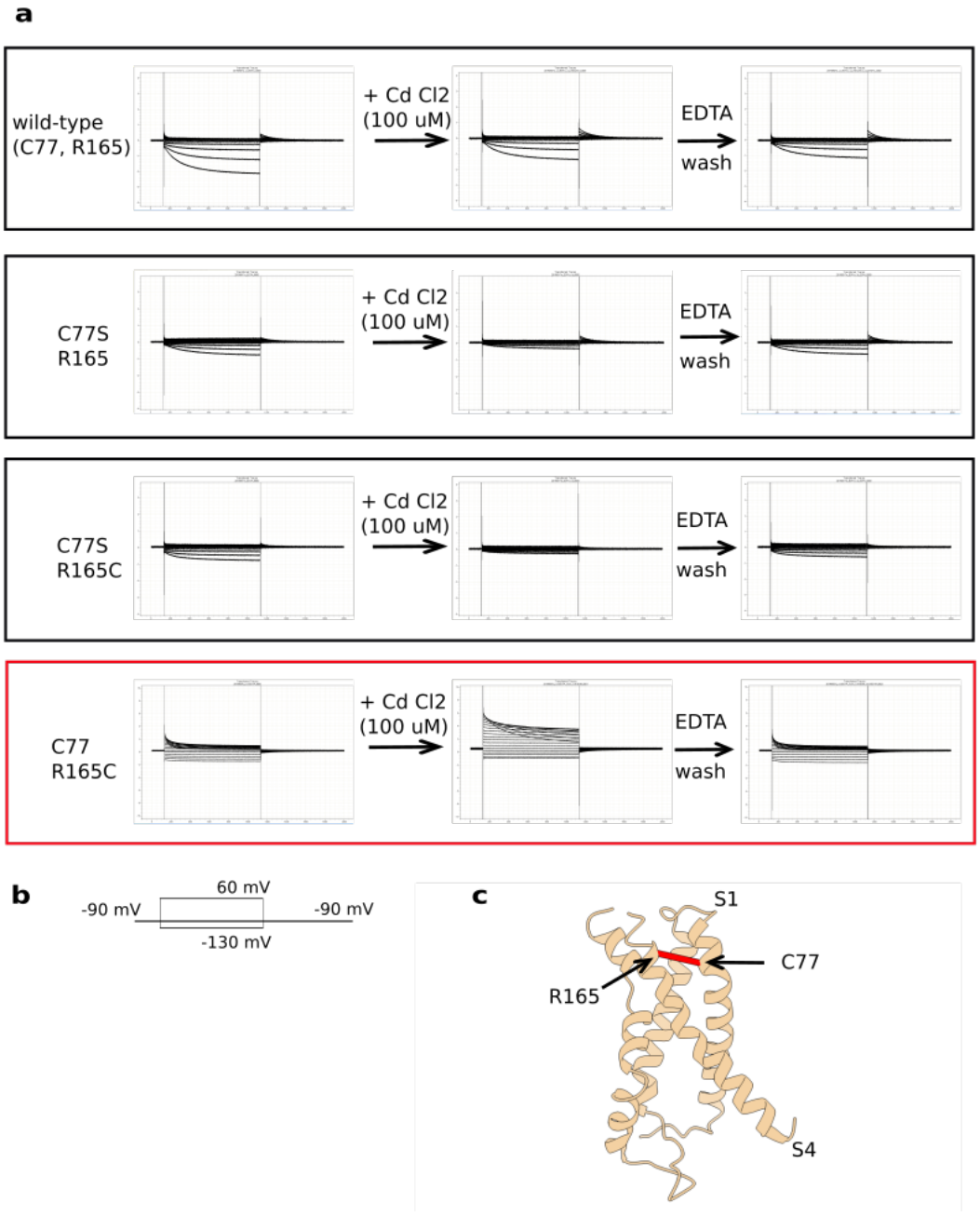

Figure 2-18: A cysteine-Cd^{2+}-cysteine bridge in the KAT1 VSD promotes channel opening. **a,** Raw current traces for all four combination of C77(S) and R165(C). Upon washing with 100 uM $CdCl_2$, current increases only in the C77-R165C condition (red box, middle panel), and then decreases again upon EDTA wash. **b,** Pulse protocol used during experiment **c,** Mapping of C77 (on S1) and R165 (on S4) onto the 'up' VSD structure of KAT1. Alpha carbons are connected by a red line.

During the course of our metal bridge experiments, we found an additional cysteine-cysteine interaction (**Fig. 2-19**). The double mutant C77-S168C channel is significantly harder to close at positive potentials than any of the other 3 mutants in the square (WT, C77S, C77S-S168C), indicating a likely interaction between positions 77 and 168 only when both are cysteines. Washing with 100 uM $CdCl_2$, 100 uM EDTA, or 2mM DTT had no effect on the currents. However, this interaction may still be metal-mediated, and is simply poorly reversible due to the strength of the interaction, or the depth of the C77-S168C pair within the VSD, where it likely not as solvent-accessible as the above described pair C77-R165C. The pair C77-S168C also has a striking effect on the channel kinetics; at negative potentials, the slow opening rise of wild-type and C77S / C77S-S168C is gone, and replaced with a step function, indicating that the C77-S168C mutant channel is already open. Thus, while we cannot determine the molecular nature of the interaction between positions 77 and 168, we conclude that they require both positions to be substituted for cysteine, are refractory to mild EDTA and DTT washes, and stabilize the open state of the channel, and / or destabilize the closed state of the channel.

Figure 2-19

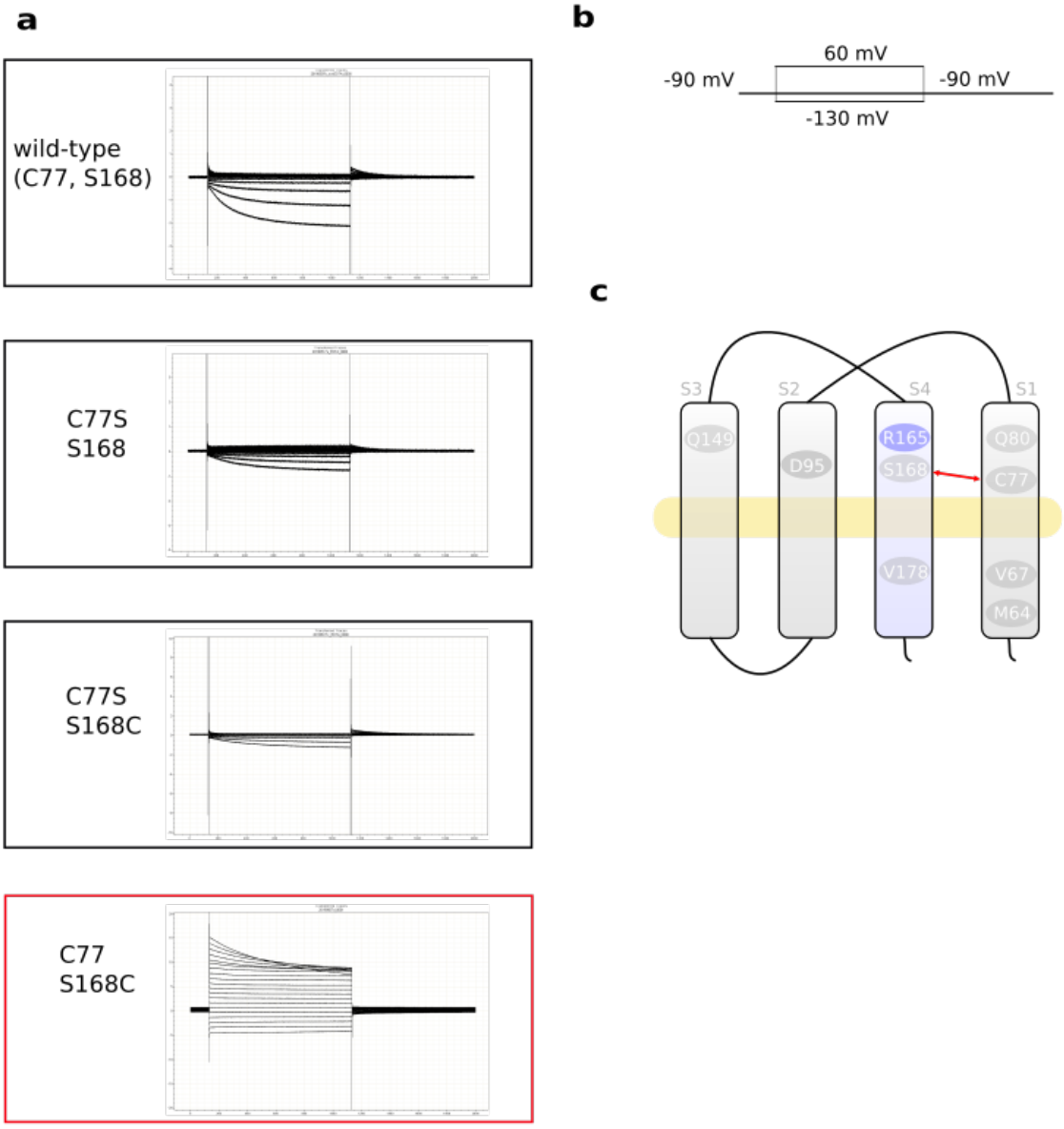

Figure 2-19: A cysteine - cysteine interaction in the KAT1 VSD promotes channel opening. **a,** Raw current traces for all four combination of C77(S) and S168(C). Washing with 100 uM $CdCl_2$, 100 uM EDTA, or 2mM DTT had no effect on the currents. **b,** Pulse protocol used during experiment **c,** Diagram indicating proximity of C77 and S168 in the KAT1 VSD.

Previous studies constructed a putative open state model of KAT1 by employing a second-site suppressor (SSS) approach using a yeast functional complementation (Grabe et al., 2007; Lai et al., 2005). Four SSS constraints from these studies are in general agreement with a one-click S4 motion (**Fig. 2-17g**) and are discussed here. The literature pair C77R-R171E is in excellent agreement with our model, and is also chemically intuitive. This constraint would favor a downward movement of one helical turn, as a downward movement of two helical turns would place R171E below the gasket, and likely too far from C77R to interact. The pair literature R165K-H210E is formally possible given the KAT1em structure, and is chemically reasonable. The final two literature pairs, W75D-M169L and W75E-N99D, are difficult to explain based on our structure, as the side chain of W75 (on S1), is pointing away from the helical bundle, and should be interacting with lipid tails. Unfortunately, we were unsuccessful in measuring KAT1 currents in *Xenopus* oocytes for any of the literature SSS pairs (Grabe et al., 2007; Lai et al., 2005) (data not shown). Thus, while the SSS constraints likely represent real interactions, we give preference to our newly generated constraints from double mutant cycle analysis as these alanine mutants exhibit more similar electrophysiological characteristics as the wildtype channel.

Altogether, a general picture emerges in which a subtle downward S4 movement promotes pore opening. This movement is equivalent to one-to-two clicks of the S4 helix in relation to the existing countercharges (and other stabilizing side chains) in S2 and S3. The extent of S4 movement can also be correlated to the amount of gating charge moved per sensor during the early stages of channel activation. This limiting slope analysis yielded 0.75 e in KAT1 (Latorre et al., 2003), which serves as a lower bound on the total amount of charge moved by the channel upon activation. We performed MD simulations on our hypothetical ‘one-click’ and ‘two-click’ downward VSD models in isolation (**Figs. 2-17d-f**) in order to calculate the amount of gating

charge displaced during these putative transitions, allowing for comparison to limiting slope estimates. We obtained 1.02 e equivalent charge for the one-click mode and 1.57 e for the two-click model (**Fig. 2-17f**). Thus, our hypothetical models, particularly the one-click model, are consistent with the literature limiting slope estimate and our double mutant cycle constraints, and may be either accentuated or attenuated via rotameric rearrangement of S4 arginines (Li et al., 2014). Our proposed KAT1 VSD motion would encompass a ~5-7 Å displacement, similar to that proposed for depolarization-activated channels (Vargas et al., 2012) and as has been observed in other VSD structures (Guo et al., 2016; Li et al., 2014; Xu et al., 2019; Yan et al., 2017). In light of this result, a major question still remains: how is this "canonical" downward VSD motion coupled to pore opening in a hyperpolarization-activated channel (Latorre et al., 2003; Männikkö et al., 2002; Sesti et al., 2003)?

A mechanism for electromechanical coupling in non-domain-swapped channels

The present KAT1 structure follows the physiological configuration expected in the nominal absence of a bias membrane potential: The VSD in its '*up'* conformation, securing a *closed* inner bundle gate (**Figs. 2-7, 2-8**). With this baseline in mind, we have combined structural and functional information to define a plausible mechanism by which canonical downward S4 helix movements, common in all voltage-gated ion channels, can lead to pore opening upon hyperpolarization. Based on our structure-guided VSD-pore interfacial mutagenesis we propose that the "default" state of the KAT1 pore is in fact a *closed* conformation, similar to that of depolarization-activated Shaker (Blunck and Batulan, 2012). Thus, we suggest that the difference between depolarization-activated and hyperpolarization-activated channels need not be the "default" state of the pore. Instead, the structural and energetic relationship between the position of the intracellular gate and the S4-S5-C-linker triad in KAT1 likely allows a minimal downward movement of the S4 segment to stabilize the open state of the pore at negative potentials.

In explaining KAT1's reversed coupling, two observations need to be highlighted. First, the unusual length of the KAT1 S4 helix (**Fig. 2-8**) is reminiscent of the extra-long S4 reported in the HCN1 structure (Lee and MacKinnon, 2017). Second, the S4-S5 hairpin engages in a closely packed interface with the C-linker of the neighboring subunit, even under depolarizing conditions (0 mV). It is this tight packing that we suggest is a critical determinant of hyperpolarization-activation. We predict that, if other hyperpolarization-activated ion channels are to use the S4-S5-C-linker interface for coupling, they will also show a tightly packed interface. It is still conceivable that an S4 segment shorter than that seen in HCN1 and KAT1 is still compatible with hyperpolarization-activation. In the case of the hypothetical hyperpolarization-activated channel with short S4, we suspect that the S4-S5-C-linker tight packing would still be conserved, either by a lower "resting setpoint" of the S4, or by a higher "resting setpoint" of the C-linker, such that the S4 and the C-linker remain in contact, even in the resting/closed state. Indeed, in KAT1, the S4-S5/C-linker interaction interface is much more tightly-packed than other non-domain-swapped channels (even HCN1). This may be due in part to the possibility of HCN1 employing alternate modes of coupling (as illuminated by C-linker deleted HCN mutants) (Wainger et al. 2001) as well as drastic Eag1-HCN1 VSD-pore chimeras (Cowgill et al. 2019).

In our model of KAT1 activation, upon hyperpolarization a downward movement of S4 is directly coupled to a subsequent lateral reorientation of the C-linker of the neighboring subunit, ultimately opening the S6 gate (**Fig. 2-20**). In the structure of depolarization-activated Eag1 (also captured with an 'up' voltage sensor and closed intracellular gate), the S4 is disengaged from the C-linker (Fig. 4x). According to our model, a downward movement of the S4 of Eag1 would be unable to trigger channel opening upon membrane hyperpolarization (**Fig. 2-20c**). It is also worth noting that although KAT1 is nominally non-domain-swapped, the tight interaction

between S4 and C-linker in an adjacent subunit at rest (0 mV) ultimately leads to a process of activation gating dominated by direct communication between subunits.

Figure 2-20

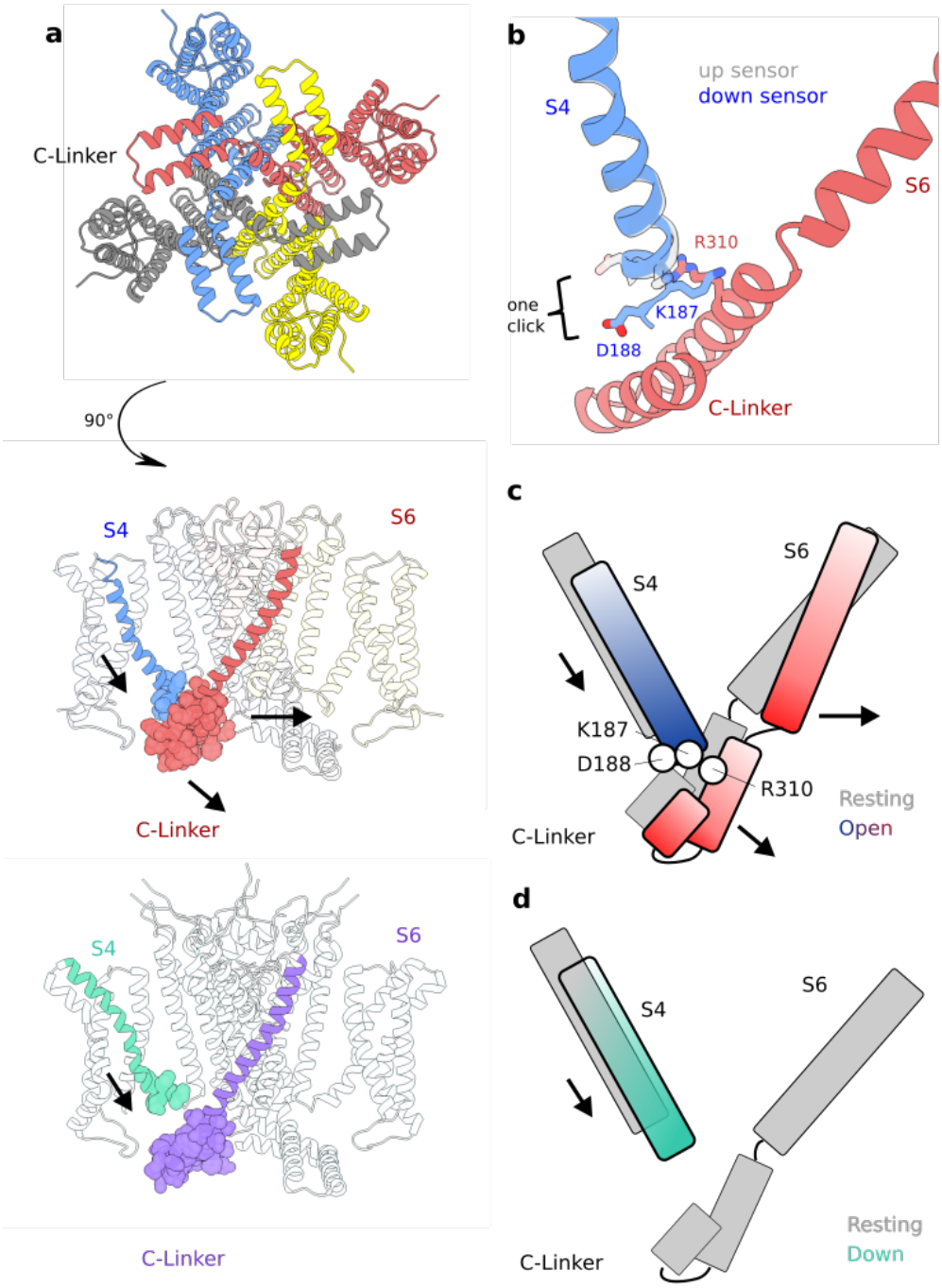

Figure 2-20: A mechanism for electromechanical coupling in KAT1.

Figure 2-20, continued.

a, Bottom and side view of KAT1em, with pCNBDs removed for clarity. Van der Waals sphere representation highlights tight packing between the 'up' S4 and closed C-linker. **b,** Zoomed-in view of the up (gray) S4 and one-click down (blue) S4 and C-linker clashes, which may trigger pore opening. **c,** Cartoon of S4-C-linker coupling, indicating key interactions. **d,** left side: structure of depolarization-activated channel rnEag1 (Whicher and MacKinnon 2016), highlighting disengagement of S4 and C-linker when the sensor is 'up' and the intracellular gate closed. N and C-terminal cytosolic domains removed for clarity. Right side: cartoon of S4-C-linker coupling in rnEag1, highlighting how the increased separation between S4 and C-linker might preclude hyperpolarization activation.

The present gating mechanism points to basic differences between HCN and KAT1 channels that better classifies KAT1 channels as "reversed K_v10-12 channels," rather than HCN-like channels. Also, it contrasts with the allosterically coupled nature of voltage-sensitive gating reported for HCN channels (Altomare et al., 2001; Alvarez-Baron et al., 2018; Chen et al., 2007; Kusch et al., 2010), where coupling might not be as strong as suggested for KAT1 (Latorre et al., 2003). Instead, KAT1 is mechanistically closer to a "reversed" directly-coupled channel like Eag (Whicher and MacKinnon, 2016) or domain swapped VGICs (Bezanilla et al., 1994; Islas and Sigworth, 1999), even if the structural nature of the coupling between S4 and S6 is intrinsically different (Blunck and Batulan, 2012; Chowdhury et al., 2014; Fernández-mariño et al., 2018). In line with this difference, phylogenetic analysis suggests that the evolutionary trajectory of plant K^+ channels may diverge significantly from that of their animal (K_v and HCN) counterparts (Riedelsberger et al., 2015). In view of these results, the present proposal is likely to have direct implications to the mechanism of gating and electromechanical coupling in non-

domain swapped channels like Eag and hERG channels, where electric field transduction (and not nucleotide binding) represents the sole driving force for channel gating.

The pseudo-CNBD structure rationalizes KAT1 insensitivity to ligand

In line with our direct coupling mechanism, KAT1 does not show canonical sensitivity to cyclic nucleotide monophosphates (cNMPs) like CNG and HCN channels do (Hoshi, 1995), despite the fact that C-terminal domain of KAT1 adopts a canonical C-linker-CNBD fold (**Figs. 2-1, 2-6, 2-21.**). The present structure clearly shows that the ligand-binding pocket in KAT1em is empty (**Fig. 2-21**). In cNMP-regulated channels, a conserved arginine within the binding pocket (R549 in hHCN1, R575 in ceTax-4) endows the ligand binding pocket with a strong electropositive nature (**Figs. 2-21d,e**) and forms a charge-charge interaction with the phosphate moiety of the cNMP (Lee and MacKinnon, 2017; Li et al., 2017). KAT1em has a glutamine in this position (Q455), resulting in an electroneutral pocket unable to form strong interactions with a cNMP (**Figs. 2-21d,e**). In cNMP-insensitive Eag/ERG channels (with a CNB-homology-domain, CNBHD), the ligand binding pocket is occupied by an "intrinsic ligand," a portion of a loop extending from the final "C" helix of the CNBHD (Brelidze et al., 2012) (**Fig. 2-21b**). KAT1em, however contains a continuous "C" helix, and lacks an intrinsic ligand (**Fig. 2-21b**), supporting a distinct mechanism of ligand insensitivity.

Figure 2-21

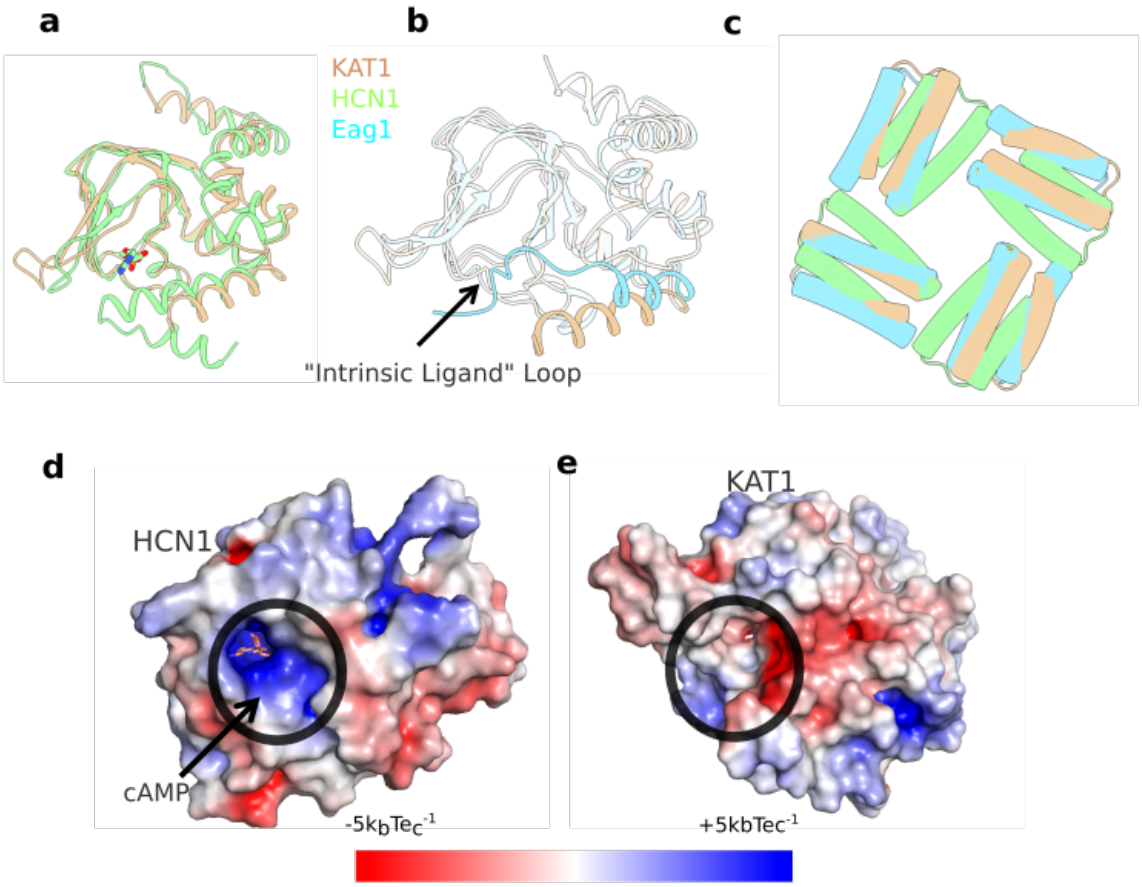

Figure 2-21: KAT1em pseudo-CNBD structure rationalizes ligand insensitivity.

a, Overlay of KAT1em pseudo-CNBD (tan) and holoHCN1 CNBD (green, 5U6P). The ligand, HCN1-cAMP is shown as sticks in cAMP binding pocket. **b,** Overlay of KAT1em (tan) and Eag1 (blue, 5K7L). KAT1 lacks “intrinsic ligand” loop of Eag1. **c,** Top-down view of KAT1em (tan), holoHCN1 (green) overlay, and Eag1 (blue). Structures were aligned / superimposed based on TMD helices. Only C-linker hairpins are shown for clarity to compare relative rotation of the C-linker to TMD, for each structure. The relative rotation of the KAT1 C-linker matches that of Eag1, not HCN1. **d,e,** Surface electrostatic potential of HCN1 (**d**) and KAT1 (**e**), respectively. Ligand binding pockets are circled in black. KAT1 lacks a deep electropositive (blue) pocket as seen in HCN1.

In HCN and CNG channels, ligand binding is thought to involve rotation of the CNBDs relative to the TMDs (Lee and MacKinnon, 2017). A counterclockwise (top-down) rotation of the C-linker/CNBD is then thought to promote channel opening (James and Zagotta, 2018). Within this context, an overlay of KAT1em, with the holo-hHCN1, and rnEag1 TMDs clearly show that the CNBD/C-linker of KAT1em appears further rotated than even the holo-hHCN1 structure, and matches almost exactly the rotation of rnEag1 (**Fig. 2-21c**). Given this, it is likely that even if KAT1 possessed a binding-competent CNBD (for instance, by making the Q455R mutant), the pseudo-CNBD might not be capable of further rotation relative to the TMD upon ligand binding and therefore might not be able to modulate the gating machinery. This suggests that the relative position of the pseudo-CNBD in KAT1 is already energetically compatible with an open conformation and thus, the key reason why KAT1 is solely activated by voltage.

Structure of the KAT1em octamer interface

The back-to-back octamer arrangement is supported by a hydrophobic interface formed by the final "C" helix of the pseudo-CNBD, packed at a 45 degree angle against its partner "C" helix from the partner tetramer (**Fig. 2-22**). KAT1em is predominantly octameric in digitonin, yet KAT1em and full-length KAT1 are present as mixtures of tetramer and octamer when purified in other gentle detergents, or when reconstituted in protein-lipid nanodiscs (**Fig. 2-4c**). The physiological role, if any, of this octamerization is unknown. We note that KAT1 octamer formation *in vivo* would require a remarkably close apposition of two membrane patches, with an estimated distance of ~140 Å from center to center of the two membranes. This is, however, on the order of membrane spacing in the thylakoid, ~40 Å (Kirchhoff et al., 2011) and thus is not without precedent. Furthermore, the hydrophobicity of residues forming the octameric interface is conserved in several other plant channels (**Fig. 2-22**). Thus, the hydrophobic face of the "C" helix could play a role in the localization and topology of closely packed membranes in plant

cells, though not necessarily the thylakoid, or more likely may serve as an interaction surface for an unknown binding partner.

Figure 2-22

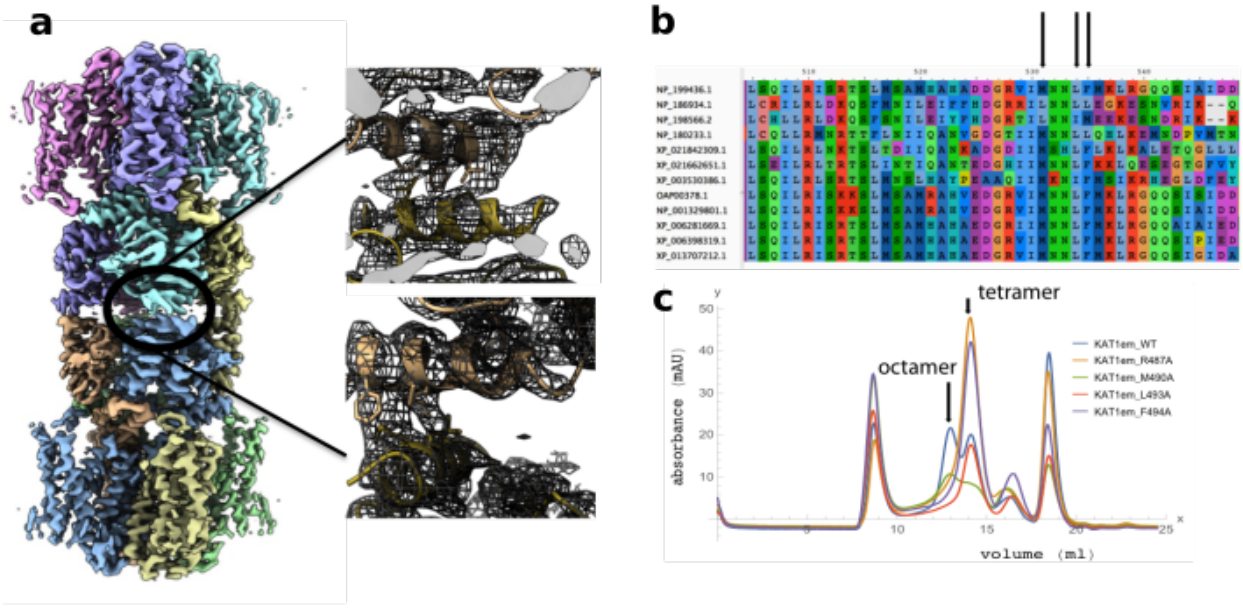

Figure 2-22: KAT1em octamer assembly.

a, Map and model for octamer. Insets show hydrophobic residues at interface. **b,** Sequence alignment of multiple plant channels, arrows indicate the hydrophobic residues at the octameric interface, which are conserved. **c,** FSEC chromatograms of “C”-helix mutants designed to break the octameric interface, indicating differential octamer to tetramer peak ratios.

Conclusion

We have determined the closed state of KAT1 by cryo-EM. Using double mutant cycle analysis, metal bridging, and literature second site suppressor data, we constructed hypothetical models to estimate the extent of motion of the VSD upon hyperpolarization. Our data are consistent with a subtle, 'one-click' downward motion of S4 which, when considered in the context of the tightly packed VSD-pore interface, may trigger pore opening. We suggest that VSD-pore coupling in KAT1, as well as in depolarization-activated sibling channels like Eag1, hERG, and SKOR (discussed in the next chapter), may follow a similar, direct mechanism. Thus, allosteric coupling like that which is described for the HCN channels might be the outlier, and thus not necessary for endowing a channel with hyperpolarization-activation. In our search for a unified direct-coupling mechanism, we should pursue structural characterization of the open state of KAT1, as well as understand the structural and functional relationship between KAT1 and its depolarization-activated siblings. Indeed, the next chapter will be devoted to our preliminary progress in understanding these questions.

Methods

Molecular Biology and Biochemistry

A DNA construct encoding amino acids M1-S502 was codon optimized for sf9 expression and synthesized by Integrated DNA Technologies. This gene was subcloned into a modified pfastBac vector containing a C-terminal 3C protease site, eGFP, and His8 using restriction sites 5'NotI and 3'XbaI. Baculovirus was generated via the Bac-to-Bac method (Invitrogen). P0 virus was amplified once to yield P1 baculovirus, which was used to infect sf9 cells at a 1:50 v/v ratio. Cells were harvested 36-40hrs post infection, washed in phosphate-buffered saline pH 7.4, dounce homogenized in hypotonic buffer A (20mM HEPES pH7.4, 20mM KCl, 10mM $MgCl_2$) and ultracentrifuged. This hypotonic lysis cycle was repeated four times and was subsequently followed by one cycle in hypertonic buffer (buffer A plus 800mM NaCl). Membranes were resuspended in 50mM HEPES pH7.4, 200mM KCl supplemented with 40% glycerol and flash frozen. For purification all steps were performed at 4°C. Membranes were thawed, diluted with glycerol-free buffer and detergent-extracted in 50mM HEPES pH7.4, 200mM KCl, 1% DDM (anatrace), 0.2% CHS (steraloids), asolectin (Sigma, crude) 0.05mg/ml for 90min. Solubilized supernatant was isolated by ultracentrifugation and diluted with low-detergent buffer to drop DDM/CHS concentration to ~0.5%. Supernatant was batch bound to Cobalt IMAC Talon beads (clontech) for 2-3hrs with 5mM imidazole present. Beads were collected by low speed centrifugation and washed in batch with 50mM HEPES pH7.4, 200mM KCl, 0.05% DDM (anatrace) 0.01% CHS (anatrace), asolectin (avanti) 0.05mg/ml, 15mM imidazole. Beads were transferred to plastic column and further washed exchanging stepwise to buffer containing digitonin 0.05% (millipore) and eluted in 50mM HEPES pH7.4, 200mM KCl, 0.05% digitonin, 250mM imidazole. Protein was cleaved by HRV 3C protease (Shaya et al., 2011) for 3hrs, concentrated and subjected to size exclusion chromatography on a superose 6 column (GE)

with running buffer: 50mM HEPES pH7.4, 200mM KCl, 0.05% digitonin, 2mM CaCl2. Peak fractions were collected and concentrated to 4-5mg/ml (millipore concentrator unit).

CryoEM analysis

Quantifoil 200mesh 1.2/1.3 grids (Quantifoil) were plasma cleaned for 30sec in an air mixture in a Solarus Plasma Cleaner (Gatan). Grids were frozen in liquid nitrogen-cooled liquid ethane in a Vitrobot Mark IV (FEI) using the following parameters: sample volume 3.5ul, blot time 2.5sec, blot force 3, humidity 100%, temperature 22C and double filter papers on each side of the vitrobot.

Grids were screened on a 200 kV Talos side entry microscope (FEI) equipped with K2 summit direct detector (Gatan) using a Gatan 626 single-tilt holder. Replicate grids from the same preparation were shipped to the National Cryo-Electron Microscopy Facility at the National Cancer Institute. Grids were imaged on a Titan Krios with K2 detector (super-resolution mode) and GIF energy filter (set to 20eV) at a nominal magnification of 130,000 corresponding to a super-res pixel size 0.532 Å/pix. The dose rate was roughly 4.7e-/pix/s and the exposure time was 12 seconds, yielding a total post-GIF dose of 38-43 e-/$Å^2$. 1502 movies were collected using Latitude (Gatan). Data were processed using motioncor2, Ctffind4, and Relion 2 (Kimanius et al., 2016; Rohou and Grigorieff, 2015; Scheres, 2012; Zheng et al., 2017). 1,500 particles were manually picked and classified in 2D to generate autopicking templates. Autopicking in Relion2 using a threshold of 0.5 gave ~120k Particles, which were subjected to 2D classification. 110k particles were selected from good classes, and 10k of these particles were used to generate an initial model with C4 symmetry imposed. All 110k particles were then subjected to autorefinement, yielding a 4.3 Å nominal resolution map. Inspection of the two tetramers within the octamer indicates that they are nearly indistinguishable, and are related by ~45 degree rotation at the pCNBD-pCNBD interface. Classification of all 110k particles in C1

recapitulated the overall architecture of the C4-imposed map, albeit with lower resolution and a slight tilt of the two micelles with respect to one another. The best two classes from the C1 job were combined, yielding ~90k particles, which were then subjected to autorefinement in C4. Refinement of the octamer yielded a map that was used for model building of the cytosolic domains. Focused refinement on the tetramer and subsequently the transmembrane (TM) region of the tetramer gave a reconstruction with improved map quality supporting confident building of the TM regions. Postprocessing of the focused TM map was performed in Relion 2 using the star file of the K2 detector at 300 kV and calculated a masked nominal resolution of 3.5 Å by 0.143 FSC criterion (Chen et al., 2013; Rosenthal and Henderson, 2003; Scheres and Chen, 2012). Local resolution was calculated by ResMap (Kucukelbir et al., 2013), and particle orientation distribution calculated by Relion 2 (Kimanius et al., 2016). A B-factor of -134 was used for sharpening and visualization.

Model building

Swiss-model (Arnold et al., 2006; Biasini et al., 2014) was used to generate homology models of Kat1em using hsHCN1 and rnEag1 as templates (Lee and MacKinnon, 2017; Whicher and MacKinnon, 2016). The hsHCN1-template model was then truncated to poly alanine using Chainsaw (Stein, 2008), and all loops were deleted. Secondary structural elements were rigid body fit to the density, and then refined in real space without secondary structure restraints using phenix.real_space_refine (Adams et al., 2010; Afonine et al., 2018b). Subsequent manual building in Coot (Brown et al., 2015; Emsley et al., 2010; Emsley and Cowtan, 2004) registered secondary structural elements using bulky residues and built loops where appropriate. Residues that did not show side chain density were stubbed at the Cβ. Final refinement of the transmembrane and cytosolic domains were conducted independently, against the TMD-focused map or the full-molecule map, respectively. Strong NCS constraints in

phenix.real_space_refine were used to immobilize the domain that was not currently being refined (ie the cytosolic domain during the TMD-focused map refinement).

The tetramer model was generated by applying symmetry operations to the monomer in UCSF Chimera (Pettersen et al., 2004). The octamer model was generated by docking two tetramers in Chimera using the fit-in-map tool. Side chains of the "C" helices at the octamer interface could not be assigned definite rotamers likely due to pseudo-symmetry and were stubbed at the Cβ.

Molecular Biology and Electrophysiology

The full-length, native Kat1 cDNA from Arabidopsis Thaliana was obtained from the Arabidopsis Biological Resource Center, and DNA was cloned into the pBSTA vector (Carvalho-de-Souza and Bezanilla, 2018; Shih et al., 1998). Mutations were introduced via site-directed mutagenesis and confirmed by Sanger sequencing. cRNA was synthesized using the T7 RNA expression Kit (Ambion, Invitrogen). Approximately 24hr post surgical removal from adult frogs, in accordance with animal usage protocol 71475 of the University of Chicago Institutional Animal Care and Use Committee, 50-100ng cRNA in 50nl RNAse-free water was injected into enzymatically-defolliculated oocytes. Oocytes were maintained at 18°C in Standard Oocyte Solution (SOS), a solution containing 10 mM HEPES pH 7.5, 100mM NaCl, 5mM KCl, 2mM $CaCl_2$, and 50 μg/ml gentamycin.

Macroscopic currents were recorded 36-48hrs post injection on a two electrode voltage clamp (TEVC) setup, comprising a OC-720C (Warner Instruments), Digidata 1322A 16 bit digitizer (Axon Instruments) and a Windows XP PC running Clampex10.3. Oocytes were impaled with two 3M KCl-filled Ag/AgCl electrodes with resistances in the range 0.2–1.0 MΩ, in bath containing SOS. For each mutant, more than 4 recordings were obtained, each from a different oocyte. Non-expression of a mutant was determined by absence of tail currents for more than 10 oocytes, and was confirmed in an independent injection session. KAT1 K^+ currents were

evoked by voltage steps of 1 s, going from 0 to -190 mV in 10-mV steps. The holding potential was set at 0 mV except for extremely right-shifted mutants, the holding potential was set to +20 mV or +70 mV in order to measure the full activation curve. Raw data were analyzed by in-house Python scripts.

The conductance-voltage relation (GV) was obtained by fitting the isochronal tail current to:

$$G(V) = A_2 + \frac{(A_1 - A_2)}{1 + e^{(V - V_h)zF/RT}}$$

Where V_h is the half-activation voltage, *R* is the gas constant, *T* is absolute temperature, *z* is the apparent gating charge, and *F* is Faraday's number. Data were normalized by A1 and A2 values from the fit. Recordings were excluded from analysis if leak or endogenous currents prevented analysis. A record was determined to be an outlier, and thus excluded, if the V_h was more than 10 mV (approximately two standard deviations) outside the mean of the normalized ensemble, or if the z was more than two standard deviations outside the mean of the normalized ensemble. In all figures data are presented as mean values, with error bars depicting SEM. For the majority of experiments, the error bars are sufficiently small to fall within the symbols in the figures.

Double mutant cycle analysis

Three types of residue-residue pair were selected by visual inspection of the structure: up-state pairs, down-state pairs, and negative control pairs (residues whose interactions are expected to be similar in both states). Data were processed as in the section above, and $\Delta G_{o->c}$ values extracted. These $\Delta G_{o->c}$ values were then used to calculate $\Delta G_{nonadditive}$, as follows:

$$\Delta G_{o\to c} = -zFV_h$$

$$\Delta\Delta G_{mut} = \Delta G_{o\to c}^{wt} - \Delta G_{o\to c}^{mut} = -z^{wt}FV_h^{wt} + z^{mut}FV_h^{mut}$$

$$\Delta G_{nonadditive} = \Delta\Delta G_{mut1} + \Delta\Delta G_{mut2} - \Delta\Delta G_{mut1,2}$$

Residue-residue pairs for which the magnitude of $\Delta G_{nonadditive}$ was greater than 1 kcal/mol were considered to interact, and were used in modeling. Selection of the 1 kcal/mol threshold is based on previous double mutant cycle work (Yarov-Yarovoy et al., 2012).

Oocyte membrane expression test and confocal imaging

Oocytes for each construct (wildtype, R197K, K200Q, Y290F, and R310K) were injected as described above. After 48hrs, wildtype oocytes were recorded and confirmed to give 1-2 μA of tail current. Then, 10 oocytes for each construct, as well as 10 uninjected oocytes, were washed in SOS, mechanically lysed in hypotonic lysis buffer A via pipette tip aspiration. Lysate was cleared of debris by centrifugation (10min, 1,000g), and the supernatant was isolated and ultracentrifuged (30min, 100,000g). The resulting membrane pellet was resuspended in 40 μl extraction buffer (50mM HEPES pH 7.4, 200mM KCl, 1.5/0.3% DDM/CHS), rotated at 4°C for 90 min and subsequently cleared by centrifugation (30 min, 12,000g). Supernatant was then subjected to SDS-PAGE followed by in-gel GFP imaging using a ChemiDoc Imaging System (BioRad).

For confocal imaging, oocytes were first injected and expression confirmed by recording a subset as above. Oocytes submerged in SOS were placed in a glass bottom dish (MatTek), and imaged in an Olympus DSU spinning disk confocal microscope using a 10X objective. Regions

of the animal (dark) pole were imaged to avoid intrinsic autofluorescence of the vegetal (light) pole. Each sample received identical GFP channel exposures (5 sec) and DIC exposures (47 msec). Images were batch normalized in SlideBook6 (3i) to allow for fair comparison between samples, and GFP images were false-colored in ImageJ (Schneider et al. 2012).

System construction and molecular dynamics simulations

The deposited tetramer model was prepared for MD simulations by first manually building the missing S3-S4 loop, and selecting reasonable rotamers for stubbed residues in Coot. This model was then embedded into a 1-palmitoyl-2-oleoyl-sn-glycero-3-phosphocholine (POPC) lipid bilayer solvated with a salt solution of 100 mM KCl. The symmetry axis of the protein was aligned along the z-axis. Three K^+ ions were placed at the selectivity filter ion binding sites: 'S0', 'S2' and 'S4' of the selectivity filter, separated by two additional water molecules occupying the binding sites 'S1' and 'S3'. The final system is in an electrically neutral state with orthorhombic periodic box dimensions of ~126 × 126 × 142 $Å^3$, consisting of ~227,000 atoms.

First, the all-atom system was energy minimized for 5000 steps, followed by a 50 ns equilibration simulation with gradually decreasing harmonic restraints being applied to the protein and the K^+ ions and the oxygen atoms of water in the selectivity filter. Then, a further 450 ns simulation was carried out with all restraints being removed. After this, the well-equilibrated system was simulated longer, up to 3 μs, using the special-purpose supercomputer ANTON2 (Shaw et al., 2008).

A single VSD (residues: 50−189) was used to estimate the gating charge, ΔQ, corresponding to the conformational change of the VSD between different states by calculating the average displacement charge, $\langle Q_d \rangle$, of the system. The one-click down and two-click down homology models of the VSD were built using the program MODELLER (Šali and Blundell, 1993), by

shifting the S4 helix 3 and 6 residues downwards, respectively, from the up state VSD in the cryo-EM structure.

The up state VSD was inserted into a pure POPC lipid bilayer and the z-coordinates of the Cα atoms of the two aromatic residues F111 and F155 were used to adjust the position of the VSD along the normal axis of the membrane, which was then solvated in a 100 mM KCl solution. The final neutralized system contains ~31,000 atoms. The one-click down and two-click down systems were constructed by only replacing the up state VSD protein with the one-click down and the two-click down VSD proteins, respectively. Thus, the three VSD systems have exactly the same size and components, with different protein conformations.

Each VSD system was energy minimized for 5000 steps and equilibrated for 20 ns with the restraints applied on the protein been gradually decreased from 5 to 0 kcal/mol/$Å^2$ at 0 mV. The equilibrated systems were then simulated at -300 mV, -150 mV, 0 mV, 150 mV, and 300 mV for 50 ns. Snapshots from the last 40 ns trajectories were used to calculate the average displacement charge of each system at different transmembrane voltages, using the partial charge and unwrapped z coordinate of all the atoms (Khalili-Araghi et al., 2010). The offset constant between the linearly fitted $<Q_d>$ of the systems is the gating charge associated with the conformational change between different states.

All the systems were built using the program VMD (Humphrey et al., 1996), and all the normal MD simulations were performed with the program NAMD (Phillips et al., 2005). The CHARMM36 force field (Best et al., 2012; Klauda et al., 2010) was used for proteins, phospholipids and ions, and the TIP3P model (Jorgensen et al., 1983) for water molecules. All simulations were carried out in an NPT ensemble with periodic boundary conditions and a time step of 2 fs. The temperature was kept at 300 K using the Langevin dynamics and the pressure

was kept at 1 atm using the Nose-Hoover Langevin piston method (Feller et al., 1995; Martyna et al., 1994). The long rang electrostatic force was calculated with the particle-mesh Ewald method (Essmann et al., 1995), and the van der Waals interaction was smoothly switched off at 10−12 Å. An electric field scaled by cell basis vectors was applied along the z-axis to simulate the membrane potential (Roux, 2008).

The ANTON2 simulation condition was essentially the same as that of NAMD simulations. A time step of 2 fs was used, and the temperature and pressure were controlled at 300 K and 1 atm, respectively, using the Nose-Hoover thermostat and the semi-isotropic MTK barostat (Martyna et al., 1994; 1992). Long-range electrostatic interactions were calculated using the k-space Gaussian split Ewald method (Shan et al., 2005).

Figure preparation

Structural figures were prepared with ChimeraX (Goddard et al., 2017) and Chimera (Pettersen et al., 2004), with the aid of Segger (Pintilie et al., 2010; 2016), and MOLE (Pravda et al., 2018).

Quantification and Statistical Analysis

See methods for details of statistics used for cryo-EM, electrophysiology and simulation data.

References

Adams, P.D., Afonine, P.V., Bunkóczi, G., Chen, V.B., Davis, I.W., Echols, N., Headd, J.J., Hung, L.W., Kapral, G.J., Grosse-Kunstleve, R.W., et al. (2010). PHENIX: a comprehensive Python-based system for macromolecular structure solution. Acta Crystallogr. D Biol. Crystallogr. *66*, 213–221.

Afonine, P.V., Klaholz, B.P., Moriarty, N.W., Poon, B.K., Sobolev, O.V., Terwilliger, T.C., Adams, P.D., and Urzhumtsev, A. (2018a). New tools for the analysis and validation of cryo-EM maps and atomic models. Acta Crystallogr. D Biol. Crystallogr. *74*, 814–840.

Afonine, P.V., Poon, B.K., Read, R.J., Sobolev, O.V., Terwilliger, T.C., Urzhumtsev, A., and Adams, P.D. (2018b). Real-space refinement in PHENIX for cryo-EM and crystallography. Acta Crystallogr. D Biol. Crystallogr. *74*, 531–544.

Altomare, C., Bucchi, A., Camatini, E., Baruscotti, M., Viscomi, C., Moroni, A., and Difrancesco, D. (2001). Integrated Allosteric Model of Voltage Gating of HCN Channels. J. Gen. Physiol. *117*, 519–532.

Alvarez-Baron, C.P., Klenchin, V.A., and Chanda, B. (2018). Minimal molecular determinants of isoform-specific differences in efficacy in the HCN channel family. J. Gen. Physiol. *150*, 1203–1213.

Arnold, K., Bordoli, L., Kopp, J., and Schwede, T. (2006). The SWISS-MODEL workspace: a web-based environment for protein structure homology modelling. Bioinformatics *22*, 195–201.

Best, R.B., Zhu, X., Shim, J., Lopes, P.E.M., Mittal, J., Feig, M., and MacKerell, A.D., Jr. (2012). Optimization of the Additive CHARMM All-Atom Protein Force Field Targeting Improved Sampling of the Backbone ϕ, ψ and Side-Chain χ 1and χ 2Dihedral Angles. J. Chem. Theory. Comput. *8*, 3257–3273.

Bezanilla, F., Perozo, E., and Stefani, E. (1994). Gating of Shaker K+ channels: II. The components of gating currents and a model of channel activation. Biophys. J. *66*, 1011–1021.

Bezanilla, F. (2008). How membrane proteins sense voltage. Nat. Rev. Mol. Cell Biol. *9*, 323–332.

Biasini, M., Bienert, S., Waterhouse, A., Arnold, K., Studer, G., Schmidt, T., Kiefer, F., Cassarino, T.G., Bertoni, M., Bordoli, L., et al. (2014). SWISS-MODEL: modelling protein tertiary and quaternary structure using evolutionary information. Nucleic Acids Res. *42*, W252–W258.

Blunck, R., and Batulan, Z. (2012). Mechanism of electromechanical coupling in voltage-gated potassium channels. Front. Pharmacol. *3*, 1–16.

Brelidze, T.I., Carlson, A.E., Sankaran, B., and Zagotta, W.N. (2012). Structure of the carboxy-terminal region of a KCNH channel. Nature *481*, 530–533.

Brown, A., Long, F., Nicholls, R.A., Toots, J., Emsley, P., and Murshudov, G. (2015). Tools for macromolecular model building and refinement into electron cryo-microscopy reconstructions. Acta Crystallogr. D Biol. Crystallogr. *71*, 136–153.

Carter, P.J., Winter, G., Wilkinson, A.J., and Fersht, A.R. (1984). The Use of Double Mutants to Detect Structural Changes in the Active Site of the Tyrosyl-tRNA Synthetase (Bacillus stearothermophilus). Cell *38*, 835–840.

Carvalho-de-Souza, J.L., and Bezanilla, F. (2018). Nonsensing residues in S3–S4 linker's C terminus affect the voltage sensor set point in K+ channels. J. Gen. Physiol. *150*, 307–321.

Chamberlin, A., Qiu, F., Rebolledo, S., Wang, Y., Noskov, S.Y., and Larsson, H.P. (2013). Hydrophobic plug functions as a gate in voltage-gated proton channels. Proc. Natl. Acad. Sci. U.S.A *111*, E273–E282.

Chen, S., Wang, J., Zhou, L., George, M.S., and Siegelbaum, S.A. (2007). Voltage Sensor Movement and cAMP Binding Allosterically Regulate an Inherently Voltage-independent Closed − Open Transition in HCN Channels. J. Gen. Physiol. *129*, 175–188.

Chen, S., McMullan, G., Faruqi, A.R., Murshudov, G.N., Short, J.M., Scheres, S.H.W., and Henderson, R. (2013). High-resolution noise substitution to measure overfitting and validate resolution in 3D structure determination by single particle electron cryomicroscopy. Ultramicroscopy *135*, 24–35.

Chowdhury, S., and Chanda, B. (2012). Perspectives on: conformational coupling in ion channels: thermodynamics of electromechanical coupling in voltage-gated ion channels. J. Gen. Physiol. *140*, 613–623.

Chowdhury, S., Haehnel, B.M., and Chanda, B. (2014). Interfacial gating triad is crucial for electromechanical transduction in voltage-activated potassium channels. J. Gen. Physiol. *144*, 457–467.

Cowgill, J., Klenchin, V. A., Alvarez-baron, C., Tewari, D., Blair, A., & Chanda, B. (2019). Bipolar switching by HCN voltage sensor underlies hyperpolarization activation. *Proceedings of the National Academy of Sciences of the United States of America*, *116*, 670–678. http://doi.org/10.1073/pnas.1816724116

Emsley, P., Lohkamp, B., Scott, W.G., and Cowtan, K. (2010). Features and development of Coot. Acta Crystallogr. D Biol. Crystallogr. *66*, 486–501.

Emsley, P., and Cowtan, K. (2004). Coot: model-building tools for molecular graphics. Acta Crystallogr. D Biol. Crystallogr. *60*, 2126–2132.

Essmann, U., Perera, L., Berkowitz, M.L., Darden, T., Lee, H., and Pedersen, L.G. (1995). A smooth particle mesh Ewald method. J. Chem. Phys. *103*, 8577–8593.

Feller, S.E., Zhang, Y., Pastor, R.W., and Brooks, B.R. (1995). Constant pressure molecular dynamics simulation: The Langevin piston method. J. Chem. Phys. *103*, 4613–4621.

Fernández-mariño, A.I., Harpole, T.J., Oelstrom, K., Delemotte, L., and Chanda, B. (2018). Gating interaction maps reveal a noncanonical electromechanical coupling mode in the Shaker K + channel. Nat. Struct. Mol. Biol. *25*, 320–326.

Goddard, T.D., Huang, C.C., Meng, E.C., Pettersen, E.F., Couch, G.S., Morris, J.H., and Ferrin, T.E. (2017). UCSF ChimeraX: Meeting modern challenges in visualization and analysis. Protein

Sci. *27*, 14–25.

Grabe, M., Lai, H.C., Jain, M., Jan, Y.N., and Jan, L.Y. (2007). Structure prediction for the down state of a potassium channel voltage sensor. Nature *445*, 550–553.

Guo, J., Zeng, W., Chen, Q., Lee, C., Chen, L., Yang, Y., Cang, C., Ren, D., and Jiang, Y. (2016). Structure of the voltage-gated two-pore channel TPC1 from Arabidopsis thaliana. Nature *531*, 196–201.

Hedrich, R., Moran, O., Conti, F., Busch, H., Becker, D., Gambale, F., Dreyer, I., Kuch, A., Neuwinger, K., and Palme, K. (1995). Inward rectifier Potassium channels in plants differ from their animal counterparts in response to voltage and channel modulators. Eur. Biophys. J. *24*, 107–115.

Hedrich, R. (2012). Ion channels in plants. Physiol. Rev. *92*, 1777–1811.

Hoshi, T. (1995). Regulation of Voltage Dependence of the KAT1 Channel by Intracellular Factors. J. Gen. Physiol. *105*, 309–328.

Humphrey, W., Dalke, A., and Schulten, K. (1996). VMD: Visual Molecular Dynamics. J. Mol. Graph. *14*, 33–38.

Hurst, A., Moroni, A., and Thiel, G. (2005). KAT1 inactivates at sub-millimolar concentrations of external potassium. J. Exp. Bot. *56*, 3103–3110.

Islas, L.D., and Sigworth, F.J. (1999). Voltage Sensitivity and Gating Charge in Shaker and Shab Family Potassium Channels. J. Gen. Physiol. *114*, 723–742.

James, Z.M., and Zagotta, W.N. (2018). Structural insights into the mechanisms of CNBD channel function. J. Gen. Physiol. *150*, 225–244.

Jorgensen, W.L., Chandrasekhar, J., Madura, J.D., Impey, R.W., and Klein, M.L. (1983). Comparison of simple potential functions for simulating liquid water. J. Chem. Phys. *79*, 926–935.

Khalili-Araghi, F., Jogini, V., Yarov-Yarovoy, V., Tajkhorshid, E., Roux, B., and Schulten, K. (2010). Calculation of the gating charge for the Kv1.2 voltage-activated potassium channel. Biophys. J. *98*, 2189–2198.

Kimanius, D., Forsberg, O., Scheres, S.H.W., and Lindahl, E. (2016). Accelerated cryo-EM structure determination with parallelisation using GPUs in RELION-2. eLife 1–21.

Kirchhoff, H., Hall, C., Wood, M., Herbstová, M., Tsabari, O., Nevo, R., and Charuvi, D. (2011). Dynamic control of protein diffusion within the granal thylakoid lumen. Proc. Natl. Acad. Sci. U.S.A *108*, 20248–20253.

Klauda, J.B., Venable, R.M., Freites, J.A., O'Connor, J.W., Tobias, D.J., Mondragon-Ramirez, C., Vorobyov, I., MacKerell, A.D., Jr., and Pastor, R.W. (2010). Update of the CHARMM All-Atom Additive Force Field for Lipids: Validation on Six Lipid Types. J. Phys. Chem. B *114*, 7830–7843.

Kucukelbir, A., Sigworth, F.J., and Tagare, H.D. (2013). Quantifying the local resolution of cryo-EM density maps. Nat. Methods *11*, 63–65.

Kusch, J., Biskup, C., Thon, S., Schulz, E., Nache, V., Zimmer, T., Schwede, F., and Benndorf, K. (2010). Interdependence of Receptor Activation and Ligand Binding in HCN2 Pacemaker Channels. Neuron *67*, 75–85.

Lai, H.C., Grabe, M., Yuh, N.J., and Lily, Y.J. (2005). The S4 voltage sensor packs against the pore domain in the KAT1 voltage-gated potassium channel. Neuron *47*, 395–406.

Latorre, R., Olcese, R., Basso, C., Gonzalez, C., Muñoz, F., Cosmelli, D., and Alvarez, O. (2003). Molecular Coupling between Voltage Sensor and Pore Opening in the Arabidopsis Inward Rectifier K+ Channel KAT1. J. Gen. Physiol. *122*, 459–469.

Ledwell, J.L., and Aldrich, R.W. (1999). Mutations in the S4 Region Isolate the Final Voltage-dependent Cooperative Step in Potassium Channel Activation. J. Gen. Physiol. *113*, 389–414.

Lee, C.-H., and MacKinnon, R. (2017). Structures of the Human HCN1 Hyperpolarization-Activated Channel. Cell *168*, 111–120.

Lee, S.-Y., Banerjee, A., and MacKinnon, R. (2009). Two separate interfaces between the Voltage sensor and pore are required for the function of Voltage-dependent K+ channels. PLOS Biol. *7*, 0676–0686.

Li, M., Zhou, X., Wang, S., Michailidis, I., Gong, Y., Su, D., Li, H., Li, X., and Yang, J. (2017). Structure of a eukaryotic cyclic- nucleotide-gated channel. Nature *542*, 60–65.

Li, Q., Wanderling, S., Paduch, M., Medovoy, D., Singharoy, A., McGreevy, R., Villalba-Galea, C.A., Hulse, R.E., Roux, B., Schulten, K., et al. (2014). Structural mechanism of voltage-dependent gating in an isolated voltage-sensing domain. Nat. Struct. Mol. Biol. *21*, 244–252.

Liu, K., Li, L., & Luan, S. (2005). An essential function of phosphatidylinositol phosphates in activation of plant shaker-type K + channels. *The Plant Journal*, *1*, 433–443.

Long, S.B., Campbell, E.B., and MacKinnon, R. (2005). Voltage sensor of Kv1.2: structural basis of electromechanical coupling. Science *309*, 903–908.

MacKinnon, R. (1991). Determination of the subunit stoichiometry of a voltage-activated potassium channel. Nature *350*, 232–235.

Marten, I., and Hoshi, T. (1998). The N-terminus of the K channel KAT1 controls its voltage-dependent gating by altering the membrane electric field. Biophys. J. *74*, 2953–2962.

Martyna, G.J., Klein, M.L., and Tuckerman, M. (1992). Nosé–Hoover chains: The canonical ensemble via continuous dynamics. J. Chem. Phys. *97*, 2635–2643.

Martyna, G.J., Tobias, D.J., and Klein, M.L. (1994). Constant pressure molecular dynamics algorithms. J. Chem. Phys. *101*, 4177–4189.

Männikkö, R., Elinder, F., and Larsson, H.P. (2002). Voltage-sensing mechanism is conserved among ion channels gated by opposite voltages. Nature *419*, 837–841.

Moldenhauer, H., Diaz-Franulic, I., González-Nilo, F., and Naranjo, D. (2016). Effective pore size and radius of capture for K + ions in K-channels. Sci. Rep. *6*, 1–5.

Moroni, A., Gazzarrini, S., Cerana, R., Colombo, R., Sutter, J.-U., Difrancesco, D., Gradmann, D., Thiel, G., and Biologia, D. (2000). Mutation in Pore Domain Uncovers Cation- and Voltage-Sensitive Recovery from Inactivation in KAT1 Channel. Biophys. J. *78*, 1862–1871.

Palovcak, E., Delemotte, L., Klein, M.L., and Carnevale, V. (2014). Evolutionary imprint of activation: The design principles of VSDs. J. Gen. Physiol. *143*, 145–156.

Pettersen, E.F., Goddard, T.D., Huang, C.C., Couch, G.S., Greenblatt, D.M., Meng, E.C., and Ferrin, T.E. (2004). UCSF Chimera A visualization system for exploratory research and analysis. J. Comput. Chem. *25*, 1605–1612.

Phillips, J.C., Braun, R., Wang, W., Gumbart, J., Tajkhorshid, E., Villa, E., Chipot, C., Skeel, R.D., Kalé, L., and Schulten, K. (2005). Scalable molecular dynamics with NAMD. J. Comput. Chem. *26*, 1781–1802.

Pintilie, G.D., Zhang, J., Goddard, T.D., Chiu, W., and Gossard, D.C. (2010). Quantitative analysis of cryo-EM density map segmentation by watershed and scale-space filtering, and fitting of structures by alignment to regions. J. Struc. Biol. *170*, 427–438.

Pintilie, G., Chen, D.-H., Haase-Pettingell, C.A., King, J.A., and Chiu, W. (2016). Resolution and Probabilistic Models of Components in CryoEM Maps of Mature P22 Bacteriophage. Biophys. J. *110*, 827–839.

Pravda, L., Sehnal, D., Tousek, D., Navratilova, V., Bazgier, V., Berka, K., Varekova, R.S., Koca, J., and Otyepka, M. (2018). MOLEonline : a web-based tool for analyzing channels , tunnels and pores (2018 update). Nucleic Acids Res. *46*, 368–373.

Riedelsberger, J., Dreyer, I., and Gonzalez, W. (2015). Outward rectification of voltage-gated K+ channels evolved at least twice in life history. PloS One *10*, 1–17.

Rohou, A., and Grigorieff, N. (2015). CTFFIND4: Fast and accurate defocus estimation from electron micrographs. J. Struc. Biol. *192*, 216–221.

Rosenthal, P.B., and Henderson, R. (2003). Optimal Determination of Particle Orientation, Absolute Hand, and Contrast Loss in Single-particle Electron Cryomicroscopy. J. Mol. Biol. *333*, 721–745.

Roux, B. (2008). The Membrane Potential and its Representation by a Constant Electric Field in Computer Simulations. Biophys. J. *95*, 4205–4216.

Schachtman, D.P., Schroeder, J.I., Lucas, W.J., Anderson, J.A., and Gaber, R.F. (1992). Expression of an Inward-Rectifying Potassium Channel by the Arabidopsis KAT1 cDNA. Science *258*, 1654–1658.

Scheres, S.H.W. (2012). RELION: Implementation of a Bayesian approach to cryo-EM structure determination. J. Struc. Biol. *180*, 519–530.

Scheres, S.H.W., and Chen, S. (2012). Prevention of overfitting in cryo-EM structure

determination. Nat. Methods *9*, 853–854.

Sesti, F., Rajan, S., Gonzalez-Colaso, R., Nikolaeva, N., and Goldstein, S.A.N. (2003). Hyperpolarization moves S4 sensors inward to open MVP, a methanococcal voltage-gated potassium channel. Nat. Neurosci. *6*, 353–361.

Shan, Y., Klepeis, J.L., Eastwood, M.P., Dror, R.O., and Shaw, D.E. (2005). Gaussian split Ewald: A fast Ewald mesh method for molecular simulation. J. Chem. Phys. *122*, 054101–054114.

Shaw, D.E., Chao, J.C., Eastwood, M.P., Gagliardo, J., Grossman, J.P., Ho, C.R., Lerardi, D.J., Kolossvary, I., Klepeis, J.L., Layman, T., et al. (2008). Anton, a special-purpose machine for molecular dynamics simulation. Commun. ACM. *51*, 91–97.

Shaya, D., Kreir, M., Robbins, R.A., Wong, S., Hammon, J., Brüggemann, A., and Minor, D.L. (2011). Voltage-gated sodium channel (NaV) protein dissection creates a set of functional pore-only proteins. Proc. Natl. Acad. Sci. U.S.A *108*, 12313–12318.

Shih, T.M., Smith, R.D., Toro, L., and Goldin, A.L. (1998). High-Level Expression and Detection of Ion Channels in *Xenopus* Oocytes. Meth. Enzymol. *293*, 529–556.

Sigworth, F.J. (1993). Voltage gating of ion channels. Q. Rev. Biophys. *27*, 1–40.

Smart, O.S., Neduvelil, J.G., Wang, X., Wallace, B.A., and Sansom, M.S.P. (1996). HOLE : A program for the analysis of the pore dimensions of ion channel structural models. J. Mol. Graph. *14*, 354–360.

Soler-Llavina, G.J., Chang, T.H., and Swartz, K.J. (2006). Functional Interactions at the Interface between Voltage-Sensing and Pore Domains in the Shaker Kv Channel. Neuron *52*, 623–634.

Stein, N. (2008). CHAINSAW: a program for mutating pdb files used as templates in molecular replacement. J. Appl. Crystallogr. *41*, 641–643.

Swartz, K.J. (2008). Sensing voltage across lipid membranes. Nature *456*, 891–897.

Šali, A., and Blundell, T.L. (1993). Comparative Protein Modelling by Satisfaction of Spatial Restraints. J. Mol. Biol. *234*, 779–815.

Tao, X., Hite, R.K., and MacKinnon, R. (2017). Cryo-EM structure of the open high-conductance Ca2+-activated K+ channel. Nature *541*, 46–51.

Tombola, F., Pathak, M.M., and Isacoff, E.Y. (2006). How Does Voltage Open an Ion Channel? Annu. Rev. Cell Dev. Biol. *22*, 23–52.

Vardanyan, V., and Pongs, O. (2012). Coupling of voltage-sensors to the channel pore: A comparative view. Front. Pharmacol. *3*, 1–10.

Vargas, E., Yarov-Yarovoy, V., Khalili-Araghi, F., Catterall, W.A., Klein, M.L., Tarek, M., Lindahl, E., Schulten, K., Perozo, E., Bezanilla, F., et al. (2012). An emerging consensus on voltage-dependent gating from computational modeling and molecular dynamics simulations. J. Gen.

Physiol. *140*, 587–594.

Wainger, B. J., Degennaro, M., Santoro, B., Siegelbaum, S. A., & Tibbs, G. R. (2001). Molecular mechanism of cAMP modulation of HCN pacemaker channels. *Nature*, *411*, 805–810.

Wang, W., and MacKinnon, R. (2017). Cryo-EM Structure of the Open Human Ether-à-go-go-Related K+ Channel hERG. Cell *169*, 422–430.

Whicher, J.R., and MacKinnon, R. (2016). Structure of the voltage-gated K+ channel Eag1 reveals an alternative voltage sensing mechanism. Science *353*, 664–669.

Xu, H., Hackos, D.H., Koth, C.M., Xu, H., Li, T., Rohou, A., Arthur, C.P., Tzakoniati, F., Wong, E., and Estevez, A. (2019). Structural Basis of Nav1.7 Inhibition by a Gating-Modifier Spider Toxin. Cell *176*, 702–715.

Yan, Z., Zhou, Q., Wang, L., Wu, J., Zhao, Y., Huang, G., Peng, W., Shen, H., Lei, J., and Yan, N. (2017). Structure of the Nav 1.4-**β**1 Complex from Electric Eel. Cell *170*, 470–482.

Yarov-Yarovoy, V., Decaen, P.G., Westenbroek, R.E., Pan, C.-Y., Scheuer, T., Baker, D., and Catterall, W.A. (2012). Structural basis for gating charge movement in the voltage sensor of a sodium channel. Proc. Natl. Acad. Sci. U.S.A *109*, 93–102.

Yifrach, O., and MacKinnon, R. (2002). Energetics of pore opening in a voltage-gated K+ channel. Cell *111*, 231–239.

Zei, P.C., and Aldrich, R.W. (1998). Voltage-dependent gating of single wild-type and S4 mutant KAT1 inward rectifier potassium channels. J. Gen. Physiol. *112*, 679–713.

Zheng, S.Q., Palovcak, E., Armache, J.-P., Verba, K.A., Cheng, Y., and Agard, D.A. (2017). MotionCor2: anisotropic correction of beam-induced motion for improved cryo-electron microscopy. Nat. Methods *14*, 331–332.

Zhong, W., Guo, W., and Ma, S. (2008). Intrinsic aqueduct orifices facilitate K+ channel gating. FEBS Lett. *582*, 3320–3324.

Zhou, Y., Morais-Cabral, J.H., Kaufman, A., and MacKinnon, R. (2001). Chemistry of ion coordination and hydration revealed by a K+ channel-Fab complex at 2.0 A resolution. Nature *414*, 43–48.

Chapter 3: Preliminary structural and functional characterization of the open state of plant voltage-gated K^+ channels

Multiple scientists contributed to the work presented here. They include Gustavo F. Contreras, Raymond Hulse and Rick Huang.

Abstract

The structural basis for electromechanical coupling in non-domain-swapped channels is unknown; due in part to the difficulties associated with observing a single VGIC in multiple native gating states. We address this question here by pursuing the open state structure of KAT1. We used protein engineering to generate mutant KAT1 channels with significant open probability at 0 mV (the condition of structural experiments). We then purified these mutant channels and subjected them to preliminary cryo-EM characterization. At subnanometer resolution, we observe a putative rotation of the mutant VSDs relative to the pore domain, however the mutant pore domain remains closed. Future work will attempt to alter the thermodynamic of the closed to open transition via introduction of mutants in the pore domain, increasing the likelihood of observing an open structure. Additionally, early development of a complementation assay, capable of high-throughput mutagenic characterization of the KAT1 open state, will be discussed.

The molecular basis of VGIC gating polarity, whether a channel opens via depolarization or hyperpolarization, is poorly understood due to lack of structures of maximally similar VGICs of opposite gating polarity. We also address this question here by attempting a mutagenic walk between KAT1 and SKOR, hyperpolarization and depolarization-activated K_v channels, respectively, sharing 47% identity within their transmembrane domains. Our results uncover several crucial positions in the S4 and S6 that may influence gating polarity. Furthermore,

preliminary biochemical and cryo-EM experiments on SKOR have revealed cytoplasmic domain flexibility that precludes further structural analysis.

Introduction

A major goal of structural biology is the direct determination of structures of each state in the conformational cycle of each macromolecule of interest. Such work has yielded insights into the mechanisms of enzymes, transporters and ligand-gated channels that are for the most part unparalleled in the voltage-gated channel field. With the exception of one remarkable case, the Na_vAb-toxin complex (Xu et al. 2019), it has been impossible to structurally-capture more than one physiologically-relevant voltage-gated state of the same channel (in which VSD and pore remain natively coupled). This is due in large part to a lack of techniques available to apply voltage during structural biology experiments. Thus, instead one must rely on pharmacology and/or mutagenesis to remodel the response of a given channel to an electric field nominally fixed at 0mV. Here, we describe our preliminary efforts in the mutagenic engineering of KAT1 variants that will trap the physiologic open state at 0mV. We also discuss our efforts and future directions in structurally characterizing such variants using cryo-EM. A critical advantage to single particle cryo-EM is the ability to resolve heterogeneity by classification of particles in different conformational states in the same sample preparation (*in silico* purification). Thus, even if a fraction of KAT1-variants are open at 0mV, we may be able to observe them (Xu et al. 2019).

KAT1 was originally cloned from *Arabidopsis* cDNA using a yeast complementation assay (Schachtman et al. 1992). Using a *Saccharomyces cerevisiae* strain that is deficient in K+ uptake, due to knockout of K+ transporters *trk1* and *trk2* (Ko and Gaber 1991), it was found that

that KAT1 forms a K+ channel open at the extremely negative resting potential of this yeast strain (~ -300 mV) (Schachtman et al. 1992). This same strain was used by the Jan lab to conduct second site suppressor experiments (Grabe et al. 2007; Lai et al. 2005) and now, with the newly-available KAT1 structure, presents an attractive methodology for high-throughput screening of saturation mutagenesis libraries. Using such an approach, the fitness effect of every single point mutation can be assessed (Firnberg et al. 2014), providing general insights into ion channel function. Moreover, as the assay is conducted at the negative resting potential of the yeast strain, the mutations will preferentially probe the open state of KAT1, for which we presently have limiting data. Thus, this approach may provide structural data complementary to our closed cryo-EM structure, and may help uncover the conformational changes KAT1 undergoes upon activation by membrane hyperpolarization. Here we discuss our preliminary work in the characterizing of this complementation system with the ultimate goal of conducting a saturation mutagenesis fitness experiment.

Reasoning that the determinants of gating polarity may be complex and distributed across the primary structure (sequence) of an ion channel, we sought a minimal model system. Previous work in Eag1 and HCN1 (~25% sequence identity within TMDs) relied on chimeric approaches (Cowgill et al. 2019). These were likely necessary due to major differences between Eag1 and HCN1 in terms of ligand binding, the presence of an N-terminal ‘HCN domain’, and even putative coupling mechanisms (Lee and MacKinnon 2017; Altomare et al. 2001). Such an approach offered interesting insights, culminating in a model in which the HCN VSD was termed ‘bipolar’, capable of gating upon depolarization and hyperpolarization, driving the pore to two different open states (Cowgill et al. 2019).

In plants, hyperpolarization-activated KAT1 and depolarization-activated SKOR share 47% sequence identity within the transmembrane regions. While conducting a mutagenic walk

between HCN1 and Eag1 would be prohibitively difficult, and likely unsuccessful due to low sequence identity, and poor structural similarity between the two (see chapter 2; Eag1 and HCN1 are even more structurally dissimilar than KAT1 and HCN1), it seems quite feasible in KAT1-SKOR. It is worth noting that chimeric approaches had also been previously employed in unsuccessful attempts to interconvert between KAT1 and SKOR (Porée et al. 2005). Random mutagenesis between plant channels SKOR and LKT1 generated a putatively-flipped channel, but this required introduction of a proline, and may not represent a physiologically-relevant mode of flipping (Li et al. 2008). These experiments, however, were done in the absence of a KAT1 structure. Thus, given the caveats of chimeric approaches, and with a structure of KAT1 in hand, we utilized structure-guided point substitutions to conduct a mutagenic walk between KAT1 and SKOR.

To further understand gating polarity, and facilitate comparison between KAT1 and SKOR, we attempted to determine the cryo-EM structure of *Arabidopsis thaliana* SKOR. While unsuccessful, the work suggests future directions in the structural characterization of this channel.

Results and Discussion

Preliminary functional and structural characterization of the KAT1 open state: Semi-rational protein engineering of the KAT1 VSD

The goal of our engineering was to stabilize the KAT1 ‘down’ VSD, mimicking the effect of a hyperpolarizing voltage step the channel might experience during our functional experiments. In an optimal case, if the VSD is trapped ‘down’ at 0 mV, and the VSD remains fully coupled to the

pore domain throughout the biochemical and structural analysis, it should be possible to directly determine the structure of the open pore, coupled to a 'down' VSD. Comparison of this structure with the above discussed 'up' VSD, closed pore structure would give significant insights into electromechanical coupling, as both endpoints would be known, for the 'same' channel (Blunck and Batulan 2012). Thus, we began by introducing mutations into the VSD, in the hope of right-shifting the G-V curve. Mutations were characterized individually, and then in combination by TEVC electrophysiology. Promising combinations of mutations were then introduced into the insect cell overexpression system, and protein yield and quality monitored by FSEC. This process was necessarily iterative, as multiple substitutions which gave large right shifts in the G-V reduced protein expression / stability in detergent. An illustrative example of this process is shown in **Fig 3-1**. A subset of mutations tested was rationally designed based on the logic of charge-counter charge pairing. This framework is based on the consensus mechanism of VSD activation, and posits that S4 charges exchange countercharge pairs as the S4 moves downward upon hyperpolarization (Vargas et al. 2012). Thus, generation of additional net positive charge above the gasket (either by introducing positive charges, or removing/neutralizing negative charges/dipoles in the extracellular-facing vestibule of the VSD)

This strategy was successful in generating right-shifting mutants Q80A (~$V_{1/2}$ -100), D95A (~$V_{1/2}$ -80), Q149A (~$V_{1/2}$ -90), S168A (~$V_{1/2}$ -120), S168K (~$V_{1/2}$ > -120). For reference, wildtype has ~$V_{1/2}$ -140. Alternatively, generation of additional net negative charge below the gasket (either by removing positive charges, or adding negative charges/dipoles in the intracellular-facing vestibule of the VSD) should also similarly bias the S4 to be 'down'. This strategy was successful in generating right-shifting mutants R177K (~$V_{1/2}$ -80) and R177A (channel constitutively open). In addition, we serendipitously discovered right-shifting mutants for which we lack a mechanism. An example of such a mutant is V67A (~$V_{1/2}$ -90).

In one case, we were able to generate a triple mutant, Q80A-S168K-R177K (QSR), and still purify protein to homogeneity and subject the mutant to preliminary cryo-EM analysis (**Fig. 3-1**). It was difficult to generate a quantitative P_o-V curve for QSR, as standard protocols with positive holding potentials up to 70 mV showed large currents at the holding potential. Thus, we employed a protocol holding at the K+ reversal potential, and pulsing upwards to monitor channel closure at positive potentials. The QSR mutant remains open until potentials greater than zero mV (**Fig. 3-1b**). The QSR mutant was expressed in sf9 cells following the KAT1 wildtype protocol, however the purification of QSR was significantly different. Interestingly, the QSR mutant, unlike wild-type KAT1, is unstable in digitonin (data not shown), the first indication that QSR behaves biochemically differently than wild-type, prompting us to continue with cryo-EM analysis in another condition, DDM/CHS/asolectin detergent lipid mixed micelles. The resolution of the cryo-EM analysis was severely limited, likely due to increased protein aggregation, ice thickness, and compositional heterogeneity. Even at low resolution (nominally ~10 Ang), some differences between QSR and wildtype are observed. While the inner gate of both wildtype and QSR appear to be closed, the VSDs look grossly different (**Fig. 3-1e**). Due to the low resolution, as well as the different sample conditions (digitonin vs DDM/CHS/asolectin), we are hesitant to interpret this change as physiologically relevant. Such an interpretation will require higher resolution, as well as the collection of a cryo-EM dataset of wildtype KAT1em in DDM/CHS/asolectin to control for detergent / lipid effects.

Figure 3-1

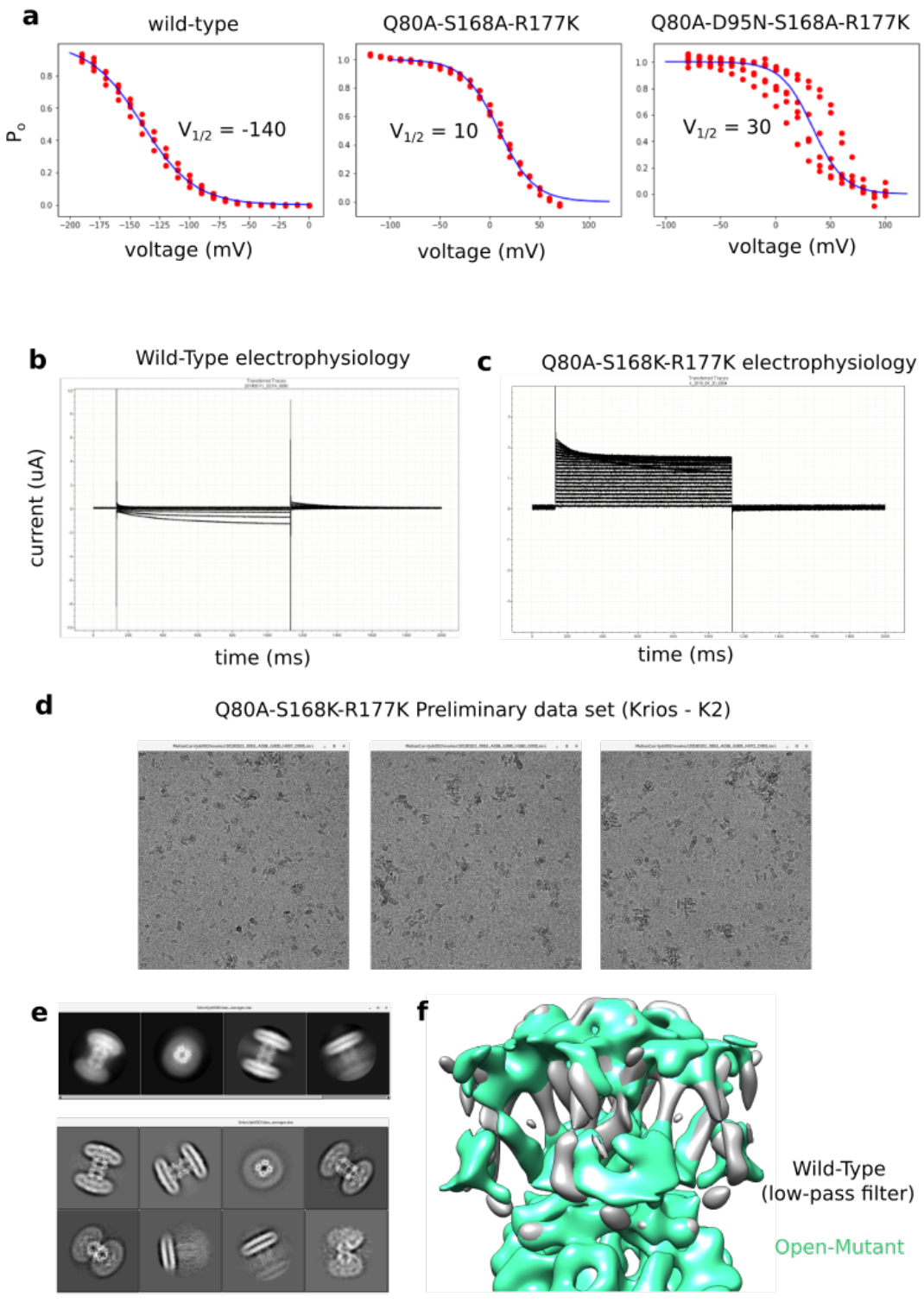

Figure 3-1: Preliminary functional and structural characterization of the KAT1 open state using a triple mutant.

Figure 3-1, continued.

a, P_o-V relations of wildtype (left panel), a right-shifted triple mutant Q80A-S168A-R177K (middle panel), and a right shifted quadruple mutant Q80A-D95N-S168A-R177K (right panel). **b,c** Raw current traces for wild-type (**b**) and a different, right-shifted triple mutant Q80A-S168K-R177K (**c**). **d,** Representative cryo-EM micrographs of triple mutant purified in DDM/CHS/asolectin. **e,** Reference-free 2D class averages from this dataset. **f,** Overlay of 3D classes for wild-type (gray) and triple mutant (green). Note poor correspondence of peripheral VSDs, possibly corresponding to a rotation of the mutant VSDs, relative to wild-type.

In another case, we exploited a single mutant (R177A) which when recorded in oocyte TEVC, gives large currents without any observed rectification / channel closure, and has zero current at the K^+ reversal potential of -90 mV in our setup. R177 is the S4 charge immediately below the hydrophobic gasket, and we suspect that it's neutralization creates a significant driving force for the S4 to translate downward to fill the electronegative "hole" created by neutralization of R177. The biochemistry of R177A was similar to that of QSR, however R177A gave higher protein yields during the extraction step. Again, similar to QSR, the cryo-EM analysis of R177A was severely limited, likely due to increased protein aggregation, ice thickness, and compositional heterogeneity (**Fig. 3-2**). However, the final resolution of R177A was better than that of QSR, showing clearer evidence of secondary structure in the 2D classes, as well as sausage-like transmembrane helices in the 3D map (**Figs. 3-2d,e**). While the same caveats of low resolution, as well as the different sample conditions (digitonin vs DDM/CHS/asolectin), still exist; in this case the comparison with wildtype is slightly more productive. Again, the inner gate appears to be closed, but, an obvious rotation of the R177A VSD with respect to the pore domain is seen, a marked difference between mutant and wildtype. Further interpretation will a cryo-EM dataset of wildtype KAT1em in DDM/CHS/asolectin to control for detergent / lipid effects. Even assuming

the VSD rotation is not a result of detergent / lipid effects, the physiological significance is not immediately obvious.

Figure 3-2

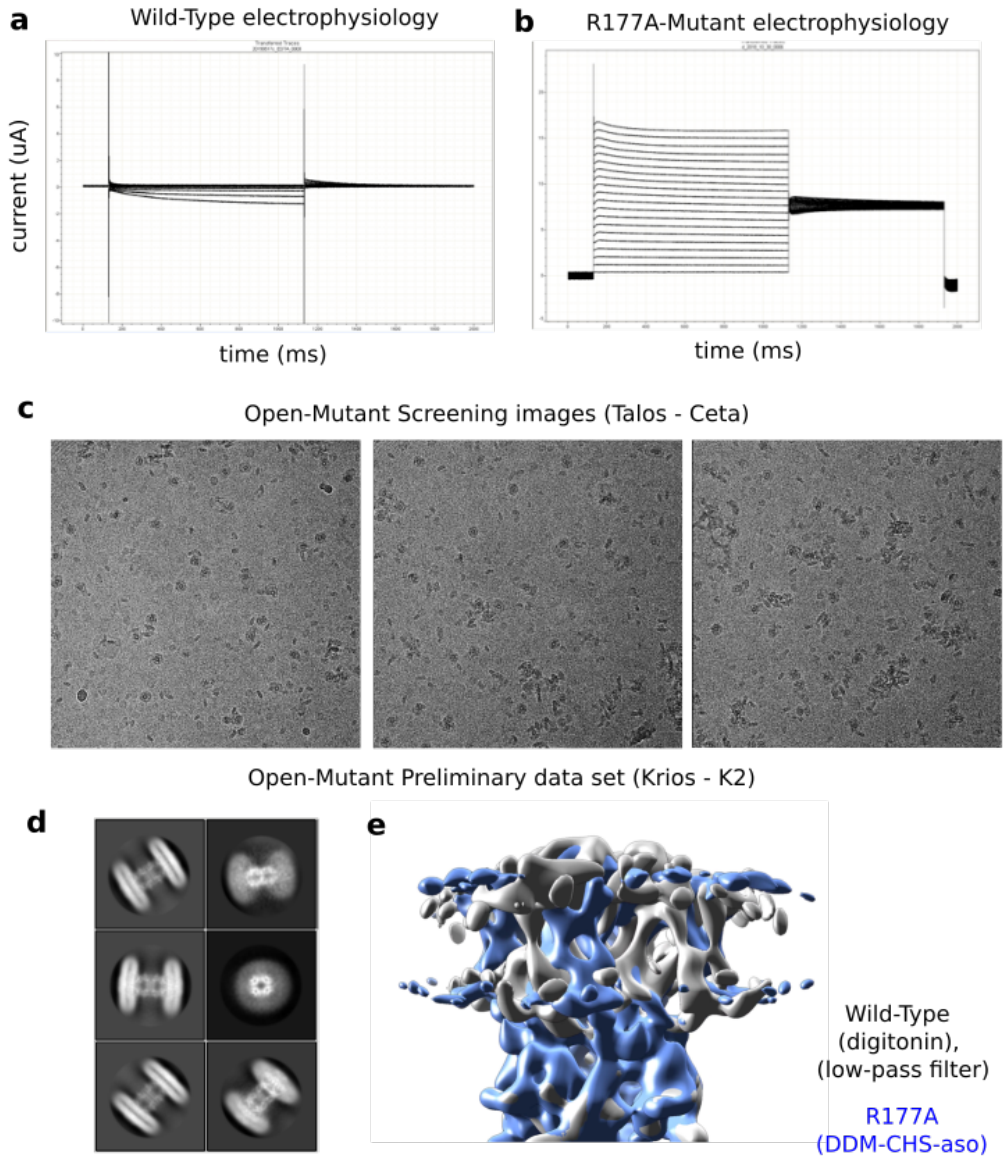

Figure 3-2: Preliminary functional and structural characterization of the KAT1 open state using a single mutant.

Figure 3-2, continued.

a,b Raw current traces for wild-type (**a**) and a single mutant R177A, which is open at all potentials, and has zero current at the K^+ reversal potential -90 mV (**b**). **c,** Representative cryo-EM micrographs of triple mutant purified in DDM/CHS/asolectin. **d,** Reference-free 2D class averages from this dataset. **e,** Overlay of 3D classes for wild-type (gray) and triple mutant (blue). Note poor correspondence of peripheral VSDs, possibly corresponding to a rotation of the mutant VSDs, relative to wild-type.

As the R177A cryo-EM map has a closed inner gate, a much higher resolution structure would be required to convincingly assign the rotated state as a *bona fide* 'down' state. Another possibility is that the rotated state might represent an intermediate state, however it is difficult to distinguish this from the possibility that the rotation is a response to an inability to open the pore. In this case the rotated state might represent a 'decoupled' state.

After two attempts (QSR and R177A) of capturing the open state, yet observing a closed inner gate, we have reconsidered our experimental approach. While the introduction of mutations exclusively in the VSD, leaving the pore domain and VSD-pore interface unperturbed, facilitates the analysis of electromechanical coupling by virtue of "changing only one thing at a time", the approach may be destined for failure if the coupling between VSD and pore domain is weakened during the purification process. Indeed, our functional mutagenesis data of the VSD-pore interface suggests that when coupling is weakened, the channel is harder to open, consistent with a thermodynamic preference of the pore domain for a closed state. Thus, in addition to mutations in the VSD, we intend to introduce mutations in the pore domain in order to alter the intrinsic stability of the pore domain. We expect that this approach may allow us to capture a more 'native' conformation in which the R177A mutation promotes a 'down' VSD and

opens a 'weaker' inner gate. To this end, preliminary biochemical characterization of R177A-pore-mutant constructs is underway.

Preliminary functional assay by yeast complementation and implications for saturation mutagenesis screening

Two methods are used to complement the K+ uptake deficiency and allow growth of the *trk1* and *trk2* knockout yeast strain. The trivial method is supplementation of the media with high (100 mM) KCl. The nontrivial method is to transform the yeast strain with a functional K+ channel or transporter, open / functional at negative membrane potentials, and a steep K+ gradient (0.5 mM KCl in the media). We first followed literature protocols to transform the strain with wildtype KAT1 full length, as well as a mouse K_{ir} channel previously shown to rescue the strain (Bagriantsev and Minor 2013). Vector containing a K_{ir} channel with stuffer sequence was also transformed as a negative control (Bagriantsev and Minor 2013), which failed to complement. Interestingly, several isolated pore domain constructs of KAT1 (starting at different points in the S4-S5 linker or S5) were also transformed and failed to complement (**Figs. 3-3c**). While we have not yet confirmed expression and trafficking, the results are not inconsistent with the default state of the KAT1 pore domain being a closed conformation. Future work will examine the expression and trafficking of these isolated pore domain constructs using GFP-fusions.

With these controls in hand, we set out to construct a calibration curve, like that schematized in **Figs. 3-3a,b**. We cloned several pore domain mutants, with known P_o-V relations determined by the gold standard of oocyte TEVC, and transformed them into the deficient strain. All mutants complemented, however the mutant which we expected to complement the most, L287A; right-shifted, actually complemented less than V299A; left-shifted (data not shown). Thus, it appears

that if a channel has too high P_o, it may hinder complementation, or alternatively L287A has some other LOF effect, independent of P_o. We favored the former explanation and attempted to reduce, and better control in general, the expression level of the channels, with the thought that the ability to tune expression levels would allow us to optimize the dynamic range of the assay for LOF versus GOF mutants. To this end, we compared KAT1 rescue efficiency using pYes2 (MET promoter) and pCM190 (tet-ON promoter) (Urlinger et al. 2000) under un-induced conditions to minimize expression. Unfortunately, both promoters yield similar rescue phenotypes (**Figs. 3-3e**). We are currently exploring additional promoter systems to find an expression level at which KAT1 fails to complement. From there, we will titrate expression to find a range in which complementation results faithfully reproduce those from electrophysiology.

Figure 3-3

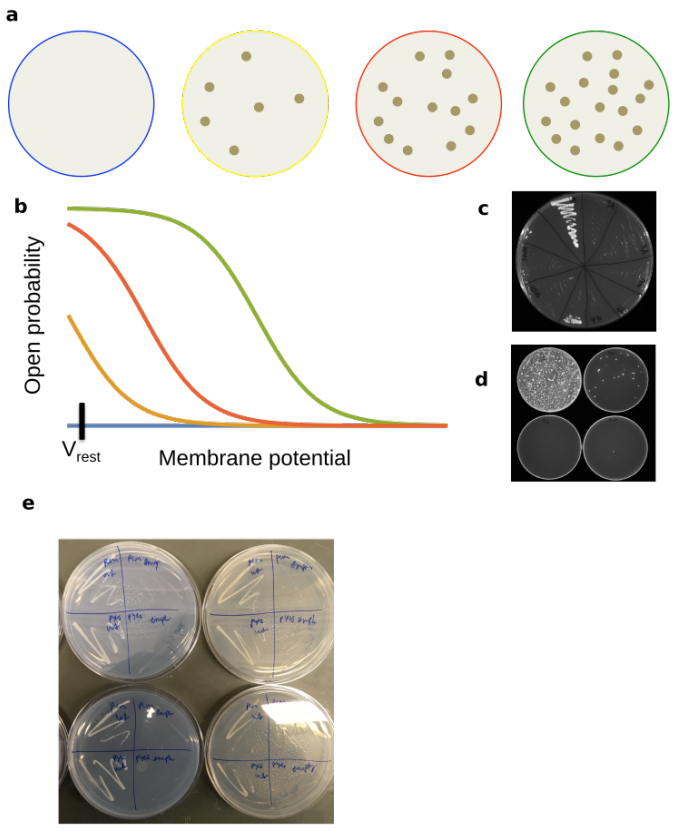

Figure 3-3: Preliminary functional assay by yeast complementation and implications for saturation mutagenesis screening

Figure 3-3, continued.

a,b Schematic of idealized results for yeast complementation assay. Mutants with high open probability will be able to better complement the K+-uptake deficiency of the strain. Plates in (**a**) are color-coded to match mutant curves in (**b**). **c,** Trial of complementation assay, in which wild-type KAT1 and mmK_{ir} rescue, while empty vector and isolated KAT1 pore domain do not. **e,** Comparison of KAT1 rescue efficiency using pYes2 (MET promoter) and pCM190 (tet-ON promoter) under un-induced conditions to minimize expression. Both promoters yield similar rescue phenotypes.

Exploring the determinants of gating polarity using KAT1 and SKOR

We utilized point mutation to conduct a mutagenic walk between KAT1 and SKOR, substituting residues from SKOR into KAT1 (**Fig. 3-4**). Substitutions were selected and prioritized based on several criteria, starting with a multiple sequence alignment of multiple plant channels (**Figs. 3-5** and **3-6**). *Criterion one*: substitutions should be in "functionally critical regions" of the channel. These regions are informed by our structure-guided mutagenesis of KAT1 (chapter 2), and include the distal S6 and proximal C-linker, the bottom of the S4, the surface of the S4 that faces the pore domain and the bound lipid, and finally the S5. Thus, already the search space is narrowed considerably: S1-S3 are excluded, as are the selectivity filter/turret helices and CNBD. *Criterion two*: we more strongly prioritize non-conservative mutations (e.g. tryptophan to glycine). *Criterion three:* we prefer to introduce substitutions that occur in clusters of interacting residues (termed SKOR Clusters, or SCs). Propensity to interact was determined by physical proximity, as well as loosely assessed by manual covariation analysis. Thus, in the case of KAT1-SKOR, whenever a substitution was found meeting criteria one and two, residues in close structural proximity were checked for any evidence of covariation with the original substitution identified. If covarying residues were identified, then they were grouped together as a single SC.

Figure 3-4

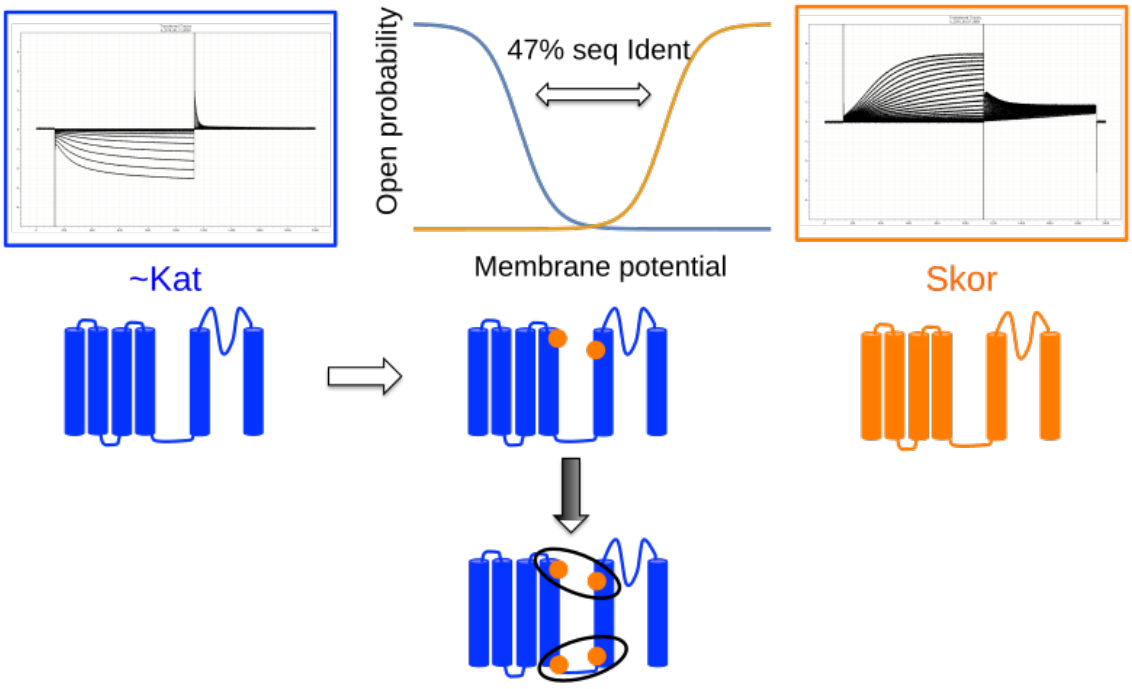

Figure 3-4: Schematic framework for KAT1 – SKOR flipping experiments
Raw current traces are shown for KAT1 (blue box), and for SKOR (orange box). Corresponding G-V relations are color coded for KAT1 (blue) and SKOR (orange). Below current traces, domain cartoons are shown to represent the mutagenic walk between KAT1 and SKOR. Starting with the sequence of KAT1 (blue), single amino acid substitutions from SKOR (orange), will be introduced (orange circles), with the goal of functionally converting KAT1 to SKOR (flipping; convert from hyperpolarization-activated to depolarization-activated). Mutations will be introduced as clusters of residues that may interact (black ovals surrounding orange circles), based on the KAT1 structure.

The SC concept is diagrammed in **Fig. 3-4**, where the two orange circles represent two substitutions, found in SKOR, but not in KAT1, which are in close physical proximity. It makes sense to introduce the two substitutions together. A list of substitutions within various clusters is shown below in **Table 3-1**. Representative, raw TEVC traces for the clusters are shown in **Fig. 3-7**. Note that SC1,2 indicates the introduction of SC1 and SC2 together in the same construct.

Figure 3-5

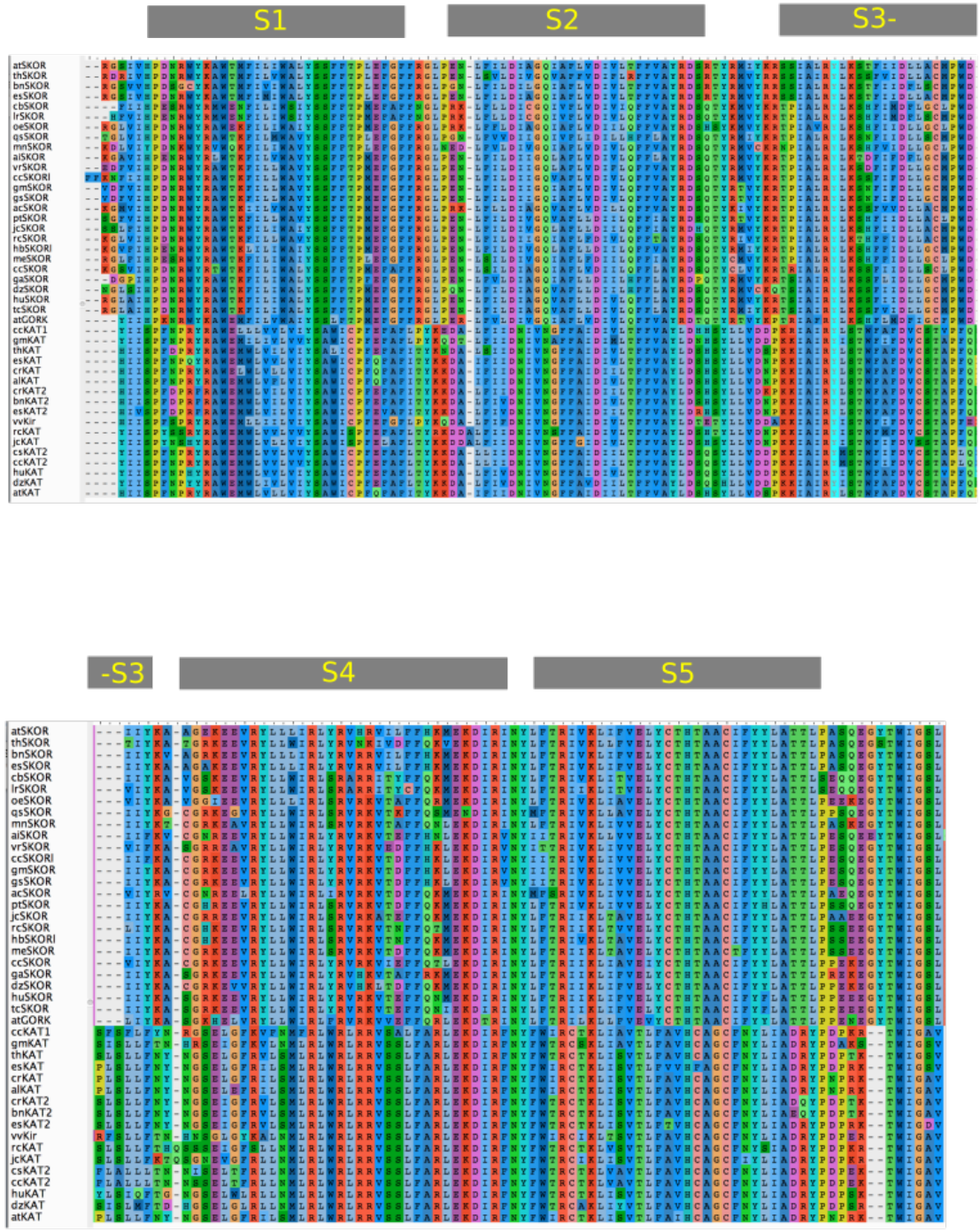

Figure 3-5: Plant Kv channel multiple sequence alignment – part 1

Figure 3-6

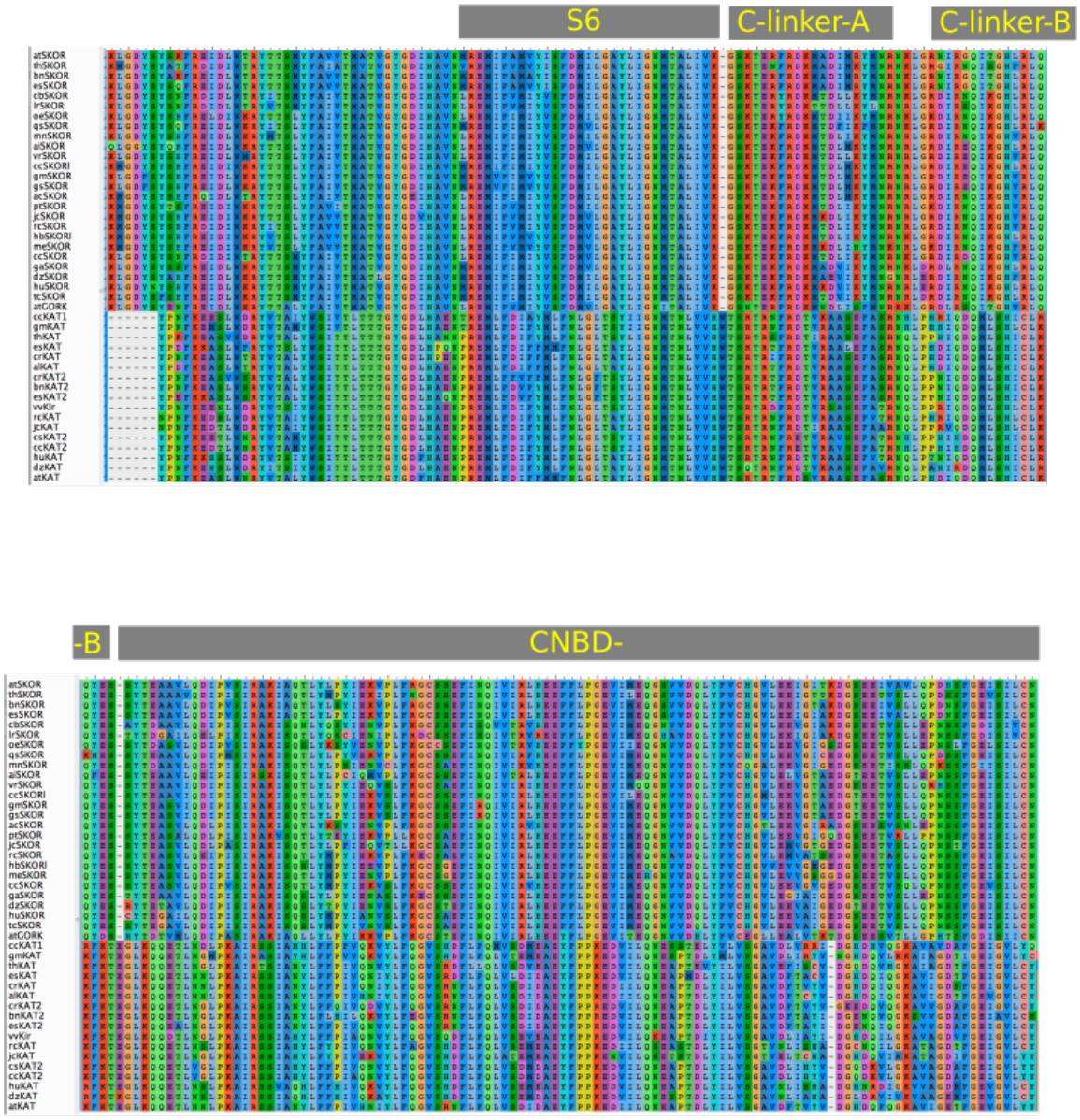

Figure 3-6: Plant Kv channel multiple sequence alignment – part 2

Note that the full pCNBD is not shown.

Table 3-1: SKOR cluster (SC) construct nomenclature

SC construct name (1st gen.)	Mutation(s)
SC1	N297A, H301K, W302G, T303deletion
SC2	R305K, R307E, E318R
SC3	F194L, I196T, C198I
SC4	T205E
SC5	G286I, T288G
SC6	N284D, L258M

SC construct name (2nd gen.)	Mutation(s)
SC7	A208C
SC8	R314A
SC9	S179I, S203F
SC10	I209T, M282S
SC11	L218Y
SC12	N216F, D277A, W253F, A250S

Table 3-1: List of SKOR Cluster (SC) substitution mutations. Only first generation mutants were cloned and characterized.

Figure 3-7

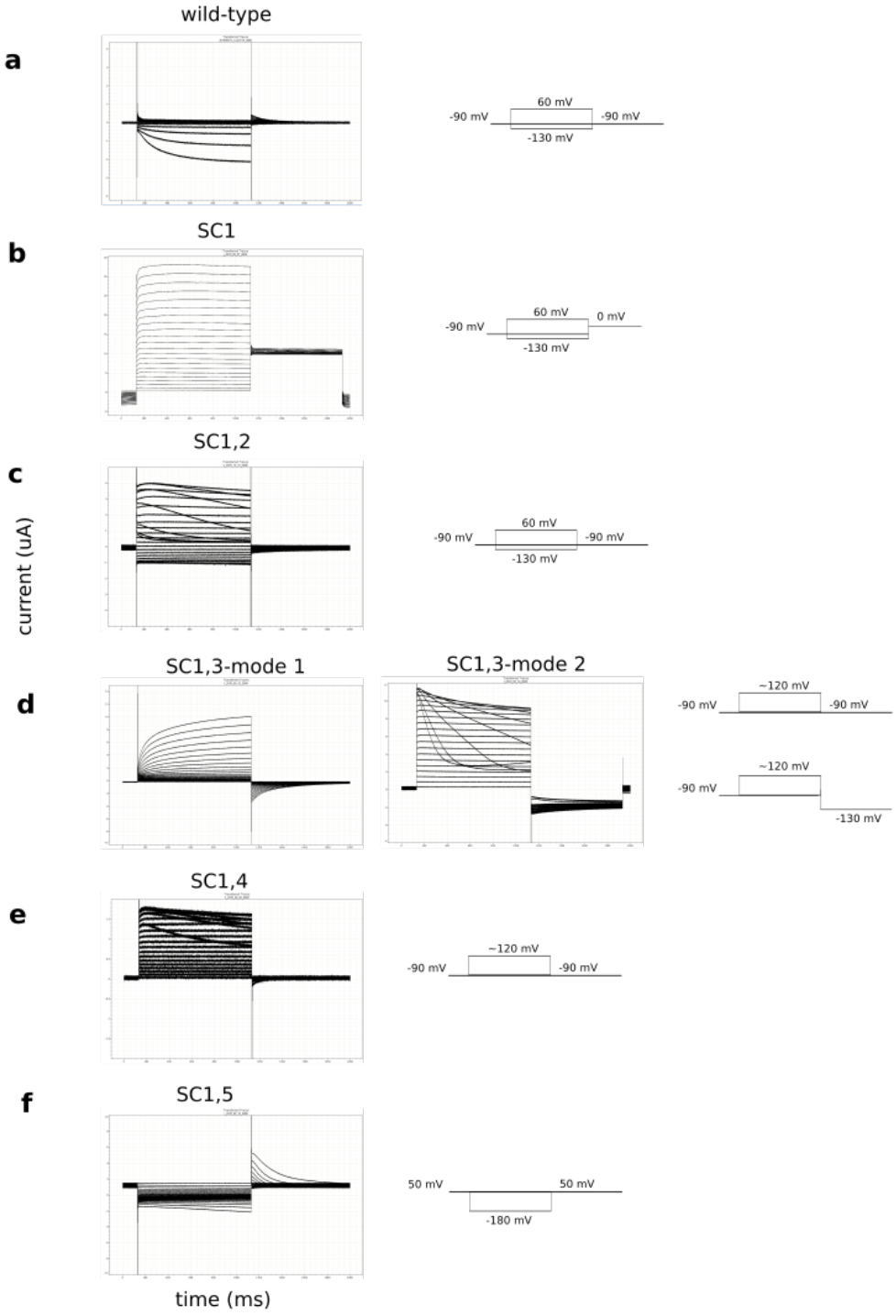

Figure 3-7: Electrophysiological characterization of flipping mutants

Raw current traces are shown for wild type (**a**), SC1 (**b**), SC1,2 (**c**), SC1,3 (**d**), SC1,4 (**e**), SC1,5 (**f**). Approximate pulse protocols used are shown to the right of each trace. Note the observation of two distinct channel types (modes) in SC1,3 (**d**).

Here, the SC electrophysiological data are discussed. We began with SC1, right at the junction where the S6 transitions to become the C-linker, due to the severe non-conservative nature of the substitutions, which include a stutter / single residue deletion. Indeed, SC1 has a striking effect; generating channels open over the entire range of measurement, with a zero current point crossing at the -90 mV K+ reversal potential. Using this background, additional SC's were introduced in combination with SC1. Introduction of SC2, several charged mutations, including two charge reversals, in the C-linker, rescued in part the effect of SC1, allowing SC1,2 to close at very positive potentials. Introduction of SC3 substitutions, several residues on S5, facing the VSD and the pore, endowed the construct SC1,3 with fascinating phenotypes. For SC1,3, two distinct types of channel activity were observed (n > 5 for each mode). The two modes correspond, roughly, to depolarization-activation (mode 1, which seems to open more at positive potentials), and hyperpolarization-activation (mode 2, which seems to close at positive potentials). However, the appearance of two such different phenotypes in different oocytes from the same injection batch is mysterious to say the least. While we do not yet have a conclusive explanation, preliminary experiments show that mode 1 is favored at low temperature (~12C) and mode 2 is favored at higher temperatures (~25C). We are actively investigating these two modes, as well as dissecting the substitutions within SC1,3 that are necessary and sufficient for giving this dual mode activity. Moving on, SC1,4 (substitution of a charged residue into S5) showed a similar phenotype to SC1,2, albeit with significantly lower channel current magnitudes for SC1,4, possibly due to expression or trafficking. SC1,5 (moving a glycine, which forms a putative gating hinge, to a different position on the opposite face S6) gave hyperpolarization-activated channels that required very negative voltages to open.

Towards structural characterization of SKOR using cryo-EM

A direct structural comparison of KAT1 and SKOR would offer several fascinating insights into gating polarity. First, we might expect SKOR to be captured in an open state at 0mV, which would give us a high confidence template for homology modeling of the KAT1 open pore. Second, KAT1 and SKOR have S4 segments of very similar lengths, and a comparison of the VSD-pore interfaces between the two channels may allow us to elucidate the minimal determinants of gating polarity. We conducted preliminary biochemical screening of SKOR (**Fig. 3-8**). Construct design was based on KAT1em, which gave SKORem, and LKT1em (LKT1 is another plant hyperpolarization-activated K_v channel). SKORem expressed at high levels in human suspension cells (HEK293 GntI-), and could be stably purified in several gentle detergents (**Fig. 3-8c**). Screening cryo-EM micrographs (**Figs. 3-8d-g**) indicated that digitonin gave superior particle distribution and contrast. A Krios-K2 dataset was collected on the digitonin sample (**Fig. 3-9**), which despite many particles, could not be processed to high resolution. The C-terminal domain (corresponding to the pCNBD in sibling KAT1em) is totally unresolved in the 2D class averages. While we do not know why this is the case, we suspected that either the domain is poorly folded, the domain becomes denatured at the air-water interface during grid preparation, or perhaps the C-terminal domain does not adopt a fixed conformation, relative to the TMD. The first two possibilities are technical issues, while the third possibility might be physiologically important.

Figure 3-8

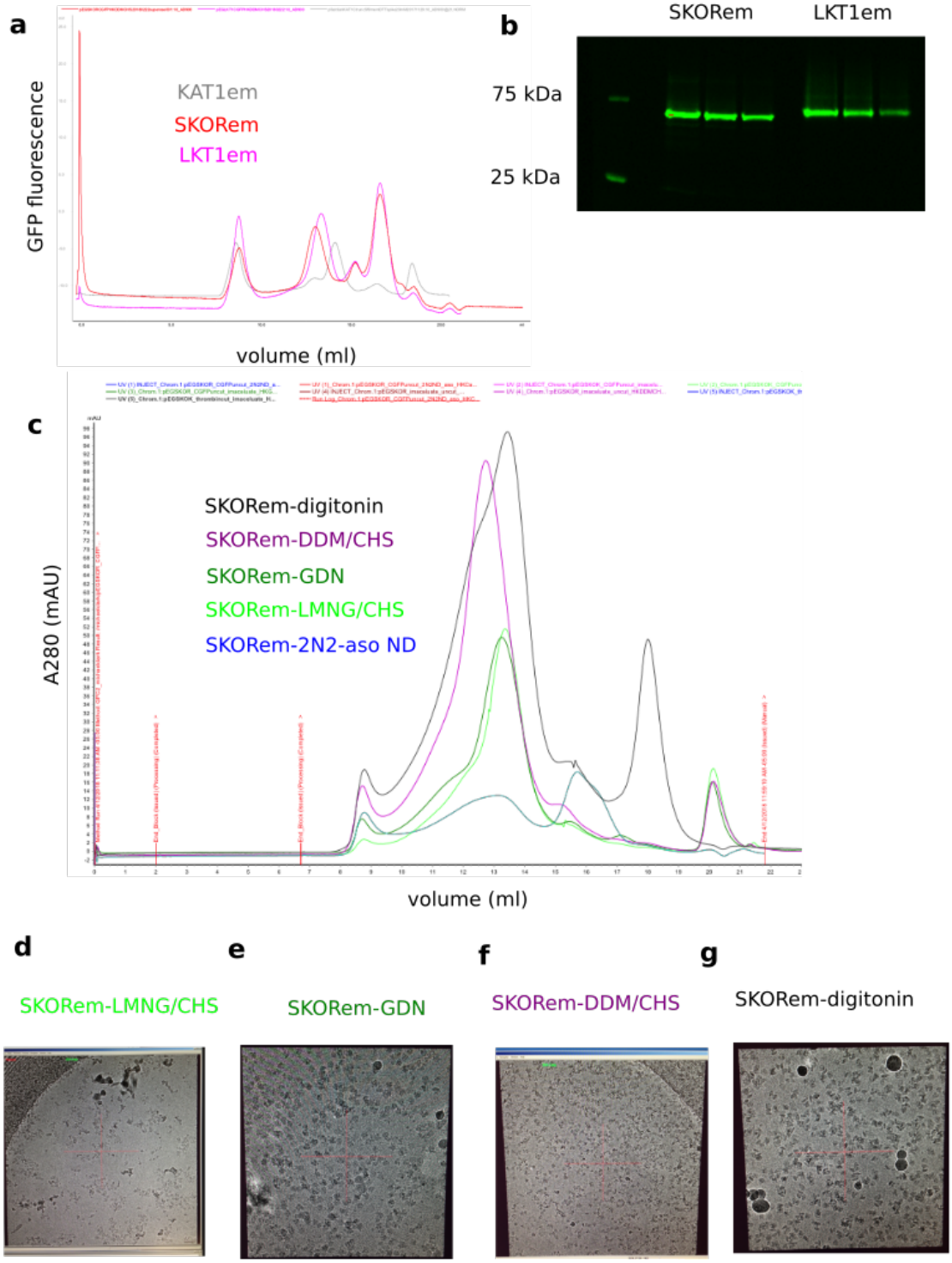

Figure 3-8: Preliminary biochemistry and cryo-EM screening of plant K_v channels SKOR and LKT1

Figure 3-8, continued.

a, FSEC traces for KAT1em (gray), SKOR (red), and LKT1 (magenta) **b,** GFP-fluorescence SDS-PAGE of SKORem-GFP and LKT1em-GFP. Three bands for each sample correspond to viral induction titers of 1:20, 1:50, and 1:100 v/v. **c,** Preparative SEC traces of SKOR under multiple conditions: digitonin (black) DDM/CHS (magenta), GDN (dark green), LMNG/CHS (light green), and reconstituted into protein lipid nanodiscs-2N2-asolectin (blue). **d-g,** Screening cryo-EM micrographs in detergents indicated.

Figure 3-9

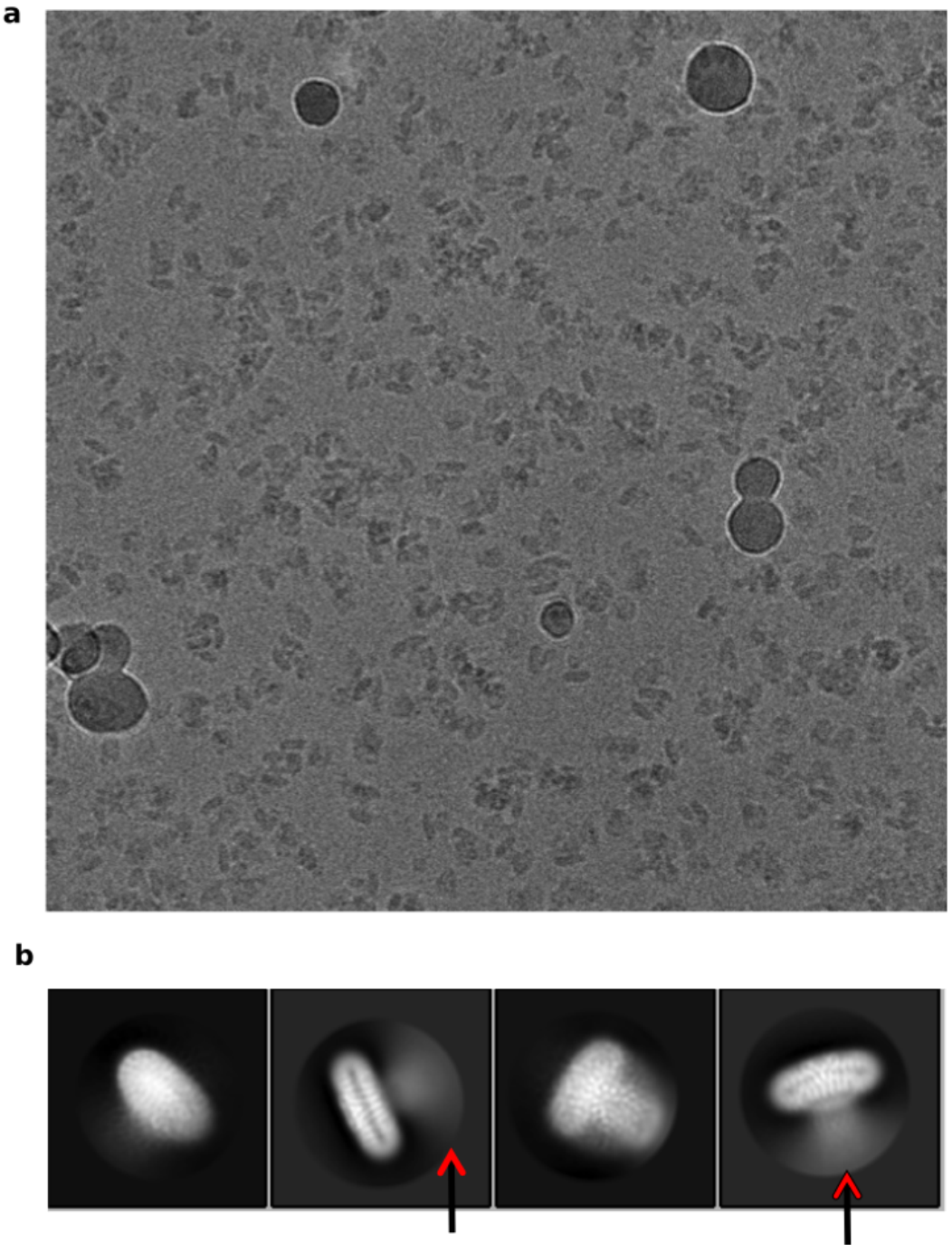

Figure 3-9: SKORem digitonin cryo-EM dataset

a, Representative cryo-EM micrograph **b,** Reference-free 2D class average of SKORem, note that the region which should correspond to the cytoplasmic domain is blurred (arrows).

To distinguish between technical (folding/denaturation) and physiological (disengagement and flexibility), we generated a SKOR-KAT1 chimera (**Fig. 3-10**), in which the pCNBD of KAT1 is joined to the TMD and C-linker of SKOR. The chimeric channel (SKchim1) is activated by depolarization in oocyte TEVC (**Figs. 3-10a,b**). Biochemical and cryo-EM analyses were conducted in a manner analogous to that of SKORem, and unfortunately yielded similar results. A Krios-K2 dataset was collected on SKchim1 in digitonin (**Fig. 3-10c,d**), which despite many particles, could not be processed to high resolution. Again the C-terminal domain (corresponding directly to the pCNBD in sibling KAT1em) is totally unresolved in the 2D class averages. Notably, the SKchim1 does not form rigid octamers like KAT1em, perhaps the first sign that the protein is in a different conformation or set of conformations. Thus, we speculate that in the open state of SKOR (and perhaps in the open state of KAT1), the pCNBD may disengage from the TMDs. This speculation of course, makes several assumptions, primarily that the KAT1em pCNBD is still folded in the context of the SKchim1 construct. However, given that the SKchim1 construct is still functional in oocytes, such an assumption is not unreasonable. If indeed the pCNBD does disengage upon channel opening, then alternate strategies must be employed to facilitate particle alignment and improve the resolution of cryo-EM analysis. One possibility might be to add mass tags / protein binders at the extracellular region of the channel. Another strategy to test the disengagement mechanism might be to engineer SKOR to be closed at 0mV, in which case the pCNBD should then repack against the C-linker and pore, adopting a stable tetrameric (or even octameric) arrangement. These are future directions in the laboratory.

Figure 3-10

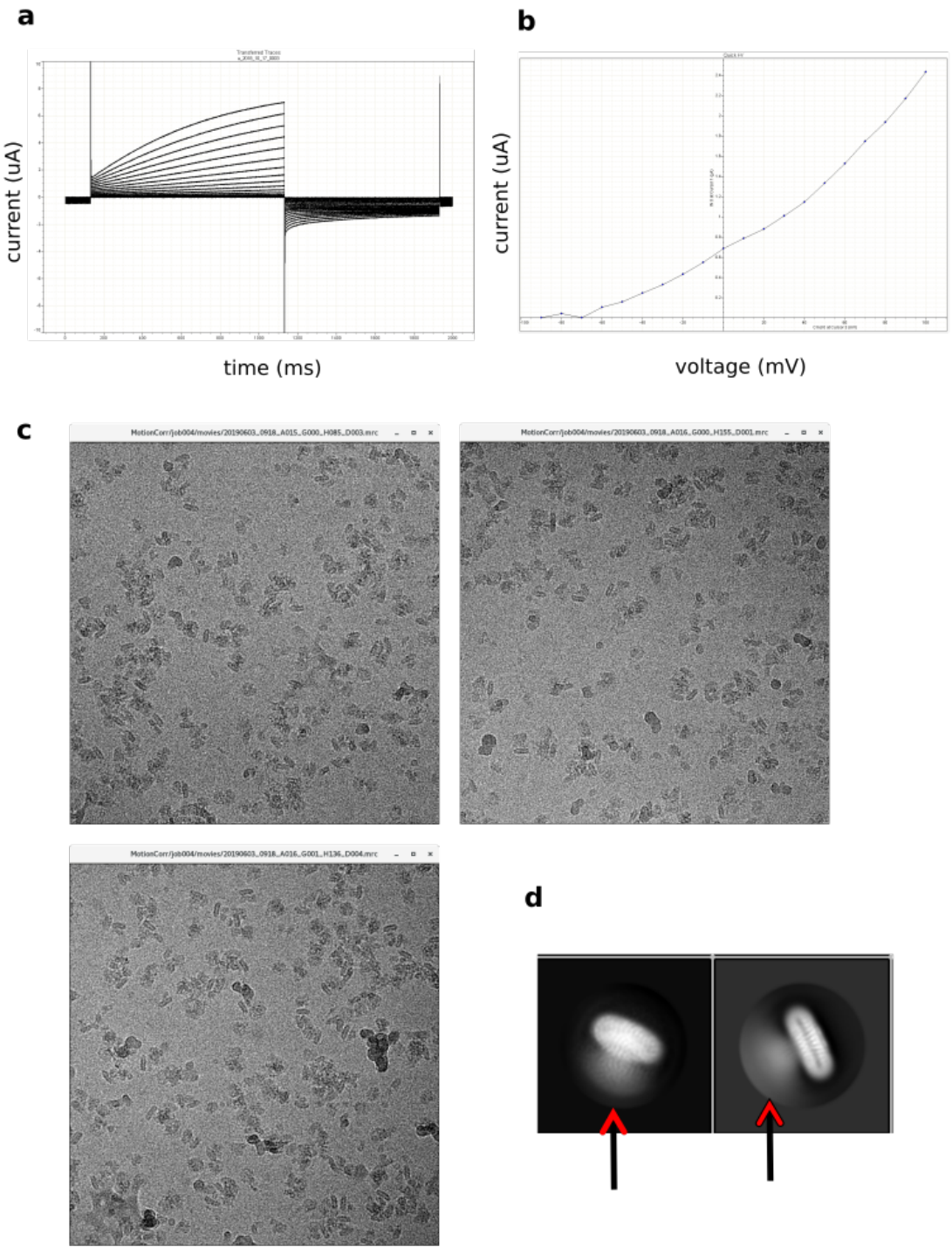

Figure 3-10: SKOR-KAT1em chimera function and digitonin cryo-EM dataset

Figure 3-10, continued.

a, Raw current trace of SKOR-KAT1em chimera, in which the CNBD of SKOR is exchanged for that of KAT1em **b,** I-V plot (generated based on an isochronal plot of the tail amplitude in **a**) **c,** Representative cryo-EM micrographs of SKOR-KAT1em chimera in digitonin. **d,** Reference-free 2D class average of SKOR-KAT1em chimera, note that the region which should correspond to the cytoplasmic domain is blurred (arrows).

Conclusion

Much of the work in this chapter is preliminary, and will hopefully form the basis for further productive inquiry. Engineering of the KAT1 open state, and/or structural determination of a depolarization-activated plant Kv channel will greatly advance our understanding of the basic conformational cycle of non-domain-swapped Kv channels: up-sensor-open-pore, up-sensor-closed-pore, down-sensor-open-pore, down-sensor-closed-pore. Presently as a scientific field, we lack both down-sensor variants, and our understanding remains incomplete. Even in the absence of high-resolution structures, site saturation mutagenesis experiments and mutagenic walks can provide insight into the down-states and gating polarity, respectively. In particular, our SC1,3 KAT1-SKOR variant is an intriguing step in this direction.

Methods

Molecular Biology and Biochemistry

DNA constructs encoding TMD-pCNBD of channels *Arabidopsis thaliana* SKOR (M1-N528) and *Solanum lycopersicum* LKT1 (M1-K503), and DNA constructs encoding full-length *Arabidopsis thaliana* SKOR and *Arabidopsis thaliana* GORK, were codon optimized for sf9 expression and synthesized by Integrated DNA Technologies. Genes were subcloned into a modified pfastBac vector containing a C-terminal 3C protease site, eGFP, and His8 using restriction sites 5'NotI and 3'XbaI. Genes were subcloned into a modified pEG vector (for human cell expression) (Goehring et al. 2014) containing a C-terminal 3C protease site, eGFP, and His8 using restriction sites 5'NotI and 3'XbaI.

For both pFastBac and pEG constructs, baculovirus was generated via the Bac-to-Bac method (Invitrogen). P0 virus was amplified once to yield P1 baculovirus, which was used to infect suspension HEK293 Gnti-/- cells at a 1:20 v/v ratio. Cells were cultured in suspension at 37C with 8% CO_2 in Freestyle media, with 2% v/v FBS and 1:1000 pen/strep antibiotic solution. Cells at were infected at a density of 3E6 cells/ml, and shifted to 30C 8-12hrs post infection, and harvested 60hrs post infection. Cells were washed in phosphate-buffered saline pH 7.4, dounce homogenized in hypotonic buffer A (20mM HEPES pH7.4, 20mM KCl, 10mM $MgCl_2$) and ultracentrifuged. Membranes were resuspended in 50mM HEPES pH7.4, 200mM KCl supplemented with 40% glycerol and flash frozen. For purification all steps were performed at 4°C. Membranes were thawed, diluted with glycerol-free buffer and detergent-extracted in 50mM HEPES pH7.4, 200mM KCl, 1% DDM (anatrace), 0.2% CHS (steraloids), asolectin (Sigma, crude) 0.05mg/ml for 90min. Solubilized supernatant was isolated by ultracentrifugation and diluted with low-detergent buffer to drop DDM/CHS concentration to ~0.5%. Supernatant was batch bound to Cobalt IMAC Talon beads (clontech) for 2-3hrs with 5mM imidazole

present. Beads were collected by low speed centrifugation and washed in batch with 50mM HEPES pH7.4, 200mM KCl, 0.05% DDM (anatrace) 0.01% CHS (anatrace), asolectin (avanti) 0.05mg/ml, 15mM imidazole, 10mM $MgCl_2$, 5mM ATP (to remove bound heat-shock proteins). Beads were transferred to plastic column and further washed exchanging stepwise to buffer containing digitonin 0.05% (millipore) and eluted in 50mM HEPES pH7.4, 200mM KCl, 0.05% digitonin, 250mM imidazole. For detergent exchange/screening experiments, other detergents were used in the place of digitonin, also at 0.05% w/v. Notably, KAT1em mutants QSR and R177A were not exchanged to digitonin, and the purification continued in 0.05% DDM (anatrace) 0.01% CHS (anatrace), asolectin (avanti) 0.05mg/ml. Proteins were cleaved by HRV 3C protease (Shaya et al., 2011) for 2-3hrs at 4C, concentrated and subjected to size exclusion chromatography on a superose 6 column (GE) with running buffer: 50mM HEPES pH7.4, 200mM KCl, 0.05% digitonin, 2mM $CaCl_2$. Peak fractions were collected and concentrated to 4-5mg/ml (millipore concentrator unit).

Nanodisc reconstitution of SKOR was based on published protocols (Dominik et al. 2016), and utilized a SKOR(monomer):2N2:asolectin ratio of 1:3:300. Reconstitution was initiated by addition of biobeads, which were rotated with the sample overnight. Biobeads were changed twice the following morning, and the sample concentrated and run on the SEC in detergent-free 50mM HEPES pH7.4, 200mM KCl, 2mM $CaCl_2$ buffer.

CryoEM analysis

Quantifoil 200mesh 1.2/1.3 grids (Quantifoil) were plasma cleaned for 30sec in an air mixture in a Solarus Plasma Cleaner (Gatan). Grids were frozen in liquid nitrogen-cooled liquid ethane in a Vitrobot Mark IV (FEI) using the following parameters: sample volume 3.5ul, blot time 2.5sec, blot force 3, humidity 100%, temperature 22C and double filter papers on each side of the vitrobot.

Grids were screened on a 200 kV Talos side entry microscope (FEI) equipped with K2 summit direct detector (Gatan) using a Gatan 626 single-tilt holder. Replicate grids from the same preparation were shipped to the National Cryo-Electron Microscopy Facility at the National Cancer Institute (except R177A dataset, which was collected at Janelia Farms Research Campus). Grids were imaged on a Titan Krios with K2 detector (super-resolution mode) and GIF energy filter (set to 20eV) at a nominal magnification of 130,000 corresponding to a super-res pixel size 0.532 Å/pix. The dose rate was roughly 4.7e-/pix/s and the exposure time was 12 seconds, yielding a total post-GIF dose of 38-43 e-/Å^2. Movies were collected using Latitude (Gatan), or Serial EM. Data were processed using motioncor2, Ctffind4, and Relion 3 (Kimanius et al., 2016; Rohou and Grigorieff, 2015; Scheres, 2012; Zheng et al., 2017). One to three thousand particles were manually picked and classified in 2D to generate autopicking templates.

For QSR: from 1414 movies, ~93k particles were picked, between 60k and 90k survived 2D classification, and 36k gave rise to the 3D map (3D class with C4 symmetry imposed). For R177A: from 9375 movies, ~364k particles were picked, ~165k survived 2D classification, and ~78k gave rise to the 3D map (3D class with C4 symmetry imposed). For SKOR: from 1923 movies, ~135k particles were picked, ~125k survived 2D classification. 3D classification was unsuccessful, yielding maps that resembled empty micelles. For SKOR-KAT1 chimera 1: from 2709 movies, ~220k particles were picked, ~190k survived 2D classification. 3D classification was unsuccessful, yielding maps that resembled empty micelles.

Molecular Biology and Electrophysiology

The full-length, native Kat1 and SKOR cDNAs from *Arabidopsis Thaliana* was obtained from the Arabidopsis Biological Resource Center, and DNA was cloned into the pBSTA vector (Carvalho-de-Souza and Bezanilla, 2018; Shih et al., 1998). Mutations were introduced via site-directed

mutagenesis and confirmed by Sanger sequencing. cRNA was synthesized using the T7 RNA expression Kit (Ambion, Invitrogen). Approximately 24hr post surgical removal from adult frogs, in accordance with animal usage protocol 71475 of the University of Chicago Institutional Animal Care and Use Committee, 50-100ng cRNA in 50nl RNAse-free water was injected into enzymatically-defolliculated oocytes. Oocytes were maintained at 18°C in Standard Oocyte Solution (SOS), a solution containing 10 mM HEPES pH 7.5, 100mM NaCl, 5mM KCl, 2mM $CaCl_2$, and 50 µg/ml gentamycin.

Macroscopic currents were recorded 36-48hrs post injection on a two electrode voltage clamp (TEVC) setup, comprising a OC-720C (Warner Instruments), Digidata 1322A 16 bit digitizer (Axon Instruments) and a Windows XP PC running Clampex10.3. Oocytes were impaled with two 3M KCl-filled Ag/AgCl electrodes with resistances in the range 0.2–1.0 MΩ, in bath containing SOS. For each mutant, more than 4 recordings were obtained, each from a different oocyte. Non-expression of a mutant was determined by absence of tail currents for more than 10 oocytes, and was confirmed in an independent injection session. KAT1 K^+ currents were evoked by voltage steps of 1 s, going from 0 to -190 mV in 10-mV steps. The holding potential was set at 0 mV except for extremely right-shifted mutants, the holding potential was set to +20 mV or +70 mV in order to measure the full activation curve. SKOR currents were evoked by voltage steps of 1 s, going from -90 to ~100 mV in 10-mV steps. Many right-shifted KAT1 and KAT1-SKOR SC mutants gave large outward currents at positive potentials. Thus, SKOR-like protocols were employed, holding at the K+ reversal potential -90 mV, and pulsing upwards to monitor channel closure. Raw data were analyzed by in-house Python scripts.

The conductance-voltage relation (GV) was obtained by fitting the isochronal tail current to:

$$G(V) = A_2 + \frac{(A_1 - A_2)}{1 + e^{(V - V_h)zF/RT}}$$

Where V_h is the half-activation voltage, *R* is the gas constant, *T* is absolute temperature, *z* is the apparent gating charge, and *F* is Faraday's number. Data were normalized by A1 and A2 values from the fit. Recordings were excluded from analysis if leak or endogenous currents prevented analysis. A record was determined to be an outlier, and thus excluded, if the V_h was more than 10 mV (approximately two standard deviations) outside the mean of the normalized ensemble, or if the z was more than two standard deviations outside the mean of the normalized ensemble.

KAT1-SKOR flipping cluster experiments

Substitutions were designed based on criteria described in the body text above. Mutations were introduced via successive rounds of site-directed mutagenesis and confirmed by Sanger sequencing after each round. As a result of this strategy, primer design for certain mutant clusters was dependent on presence of other mutations, thus, only a subset of all potential combinations of different SCs were cloned and tested.

Yeast complementation experiments

Yeast strain SGY1528 (del_trk1, del_trk2) (Anderson et al. 1992; Ko and Gaber, 1991) was a kind gift from Daniel Minor, UCSF (Bagriantsev and Minor 2013). Yeast were grown, transformed and selected closely following detailed published protocols (Bagriantsev and Minor 2013). Final recipes are shown here:

YPAD 100K liquid media (100ml)

1g yeast extract
2g peptone
2.4mg adenine
10ml 1M KCl
Autoclave.
Add 4ml of sterile glucose (50% soln) once cooled

YPAD 100K plates (500ml)
5g yeast extract
10g peptone
10g bacto agar
3.73g KCl
12mg adenine
Autoclave.
Add 20ml of sterile glucose (50% soln) once cooled

-Ura -Met 100K double drop plates (500ml total)
Part A:
10g bacto agar
250ml H2O
Autoclave.

Part B:
0.75g dropout powder
3.35g yeast nitrogen base (w/o aa)
50ml 1M KCl
200ml H2O
pH to 6.5 with free base tris
Autoclave.
Combine parts A and B, add 20ml glucose

-Ura -Met low K double drop plates (500ml total)
Part A:
7.5g LE agarose
250ml H2O
Autoclave.

Part B:
1.05g arginine free base
0.75g dropout powder
10ml glucose (50%)
0.5ml 1000X trace mineral soln
0.5ml 1000X vitamin soln
0.5ml 1M MgSO4
50 uL 1M CaCl2
250/500 uL 1M KCl
To 250ml H2O
pH to 6 with phosphoric acid
Filter sterilise.
Combine parts A and B

Amino acid dropout powder
0.6g glutamic acid
0.25g adenine hemisulfate
0.12g arginine
0.6g aspartic acid
0.18g lysine
0.3g phenylalanine
2.25g serine
1.2g threonine
0.24g tryptophan
0.18g tyrosine
0.9g valine
0.12g histidine
0.34g leucine

1000X trace metals solution (50ml final volume)
25mg boric acid
2mg $CuSO_4$
5mg KI
25mg $FeCl_3$
20mg $MnSO_4$
56mg $NaMb.H_2O$
20mg $ZnSO_4$
0.5ml HCL (6-12M)

100X vitamin soln
MEM vitamin soln, supplement with biotin

The full-length, native Arabidopsis KAT1 was cloned into a modified pYes2 plasmid (Bagriantsev and Minor 2013) using 5'HindIII and 3'XhoI. Additionally, N-terminal truncations of KAT1 (removing the VSD to generate isolated pore domains) were cloned using the same methodology, generating constructs 189-677, and 192-677. Other plasmids used included pYes2 mmK_{ir}, and pYes mmKir-H5-stuffer (a negative control, shown previously not to complement) (Bagriantsev and Minor 2013). The full-length, native Arabidopsis KAT1 was also cloned into pCM190-GFP, a tet-ON vector (Urlinger et al. 2000) using Gibson Assembly. The pCM190-GFP plasmid was a kind gift from the laboratory of Gábor Balázsi (Nevozhay et al.

2012). Additionally, the G72V mutation was introduced into the tet DNA binding protein in this plasmid, as it was shown by (Roney et al. 2016) to reduce leak expression to undetectable levels.

Figure preparation

Structural figures were prepared with Chimera (Pettersen et al., 2004).

References

Altomare, C., Bucchi, A., Camatini, E., Baruscotti, M., Viscomi, C., Moroni, A., and Difrancesco, D. (2001). Integrated Allosteric Model of Voltage Gating of HCN Channels. J. Gen. Physiol. *117*, 519–532.

Bagriantsev, S. N., & Jr, D. L. Minor. (2013). Chapter 3 Using Yeast to Study Potassium Channel Function and Interactions with Small Molecules. Methods in Molecular Biology, 995, 31–42. http://doi.org/10.1007/978-1-62703-345-9

Blunck, R., and Batulan, Z. (2012). Mechanism of electromechanical coupling in voltage-gated potassium channels. Front. Pharmacol. *3*, 1–16.

Carvalho-de-Souza, J.L., and Bezanilla, F. (2018). Nonsensing residues in S3–S4 linker's C terminus affect the voltage sensor set point in K+ channels. J. Gen. Physiol. *150*, 307–321.

Cowgill, J., Klenchin, V. A., Alvarez-baron, C., Tewari, D., Blair, A., & Chanda, B. (2019). Bipolar switching by HCN voltage sensor underlies hyperpolarization activation. *Proceedings of the National Academy of Sciences of the United States of America*, *116*, 670–678. http://doi.org/10.1073/pnas.1816724116.

Dominik, P. K., Borowska, M. T., Dalmas, O., Kim, S. S., Perozo, E., Keenan, R. J., et al. (2016). Conformational Chaperones for Structural Studies of Membrane Proteins Using Antibody Phage Display with Nanodiscs Resource Conformational Chaperones for Structural Studies of Membrane Proteins Using Antibody Phage Display with Nanodiscs. *Structure/Folding and Design*, *24*(2), 300–309. http://doi.org/10.1016/j.str.2015.11.014

Firnberg, E., Labonte, J. W., Gray, J. J., & Ostermeier, M. (2014). A Comprehensive, High-Resolution Map of a Gene's Fitness Landscape. *Molecular Biology and Evolution*, *31*(6), 1581–1592. http://doi.org/10.1093/molbev/msu081

Goehring, A., Lee, C.-H., Wang, K. H., Michel, J. C., Claxton, D. P., Baconguis, I., et al. (2014). Screening and large-scale expression of membrane proteins in mammalian cells for structural studies. *Nature Protocols*, *9*(11), 2574–2582. http://doi.org/10.1038/nprot.2014.173

Grabe, M., Lai, H.C., Jain, M., Jan, Y.N., and Jan, L.Y. (2007). Structure prediction for the down state of a potassium channel voltage sensor. Nature *445*, 550–553.

Kimanius, D., Forsberg, O., Scheres, S.H.W., and Lindahl, E. (2016). Accelerated cryo-EM structure determination with parallelisation using GPUs in RELION-2. eLife 1–21.

Ko, C. H., & Gaber, R. F. (1991). TRK1 and TRK2 Encode Structurally Related K+ Transporters in Saccharomyces cerevisiae. *Molecular and Cellular Biology*, *8*(11), 4266–4273.

Lai, H.C., Grabe, M., Yuh, N.J., and Lily, Y.J. (2005). The S4 voltage sensor packs against the pore domain in the KAT1 voltage-gated potassium channel. Neuron *47*, 395–406.

Latorre, R., Olcese, R., Basso, C., Gonzalez, C., Muñoz, F., Cosmelli, D., and Alvarez, O. (2003). Molecular Coupling between Voltage Sensor and Pore Opening in the Arabidopsis Inward Rectifier K+ Channel KAT1. J. Gen. Physiol. *122*, 459–469.

Lee, C.-H., and MacKinnon, R. (2017). Structures of the Human HCN1 Hyperpolarization-Activated Channel. Cell *168*, 111–120.

Li, L., Liu, K., Hu, Y., Li, D., & Luan, S. (2008). Single mutations convert an outward K + channel into an inward K + channel. PNAS, 105(8).

Liu, K., Li, L., & Luan, S. (2005). An essential function of phosphatidylinositol phosphates in activation of plant shaker-type K + channels. *The Plant Journal*, *1*, 433–443.

Männikkö, R., Elinder, F., and Larsson, H.P. (2002). Voltage-sensing mechanism is conserved among ion channels gated by opposite voltages. Nature *419*, 837–841.

Nevozhay, D., Adams, R. M., Van Itallie, E., Bennett, M. R., & Balázsi, G. (2012). Mapping the Environmental Fitness Landscape of a Synthetic Gene Circuit. *PLoS Computational Biology*, *8*(4), e1002480–17. http://doi.org/10.1371/journal.pcbi.1002480

Pettersen, E.F., Goddard, T.D., Huang, C.C., Couch, G.S., Greenblatt, D.M., Meng, E.C., and Ferrin, T.E. (2004). UCSF Chimera A visualization system for exploratory research and analysis. J. Comput. Chem. *25*, 1605–1612.

Porée, F., Wulfetange, K., Naso, A., Carpaneto, A., Roller, A., Natura, G., et al. (2005). Plant Kin and Kout channels: Approaching the trait of opposite rectification by analyzing more than 250 KAT1–SKOR chimeras. *Biochemical and Biophysical Research Communications*, *332*, 465–473. http://doi.org/10.1016/j.bbrc.2005.04.150

Rohou, A., and Grigorieff, N. (2015). CTFFIND4: Fast and accurate defocus estimation from electron micrographs. J. Struc. Biol. *192*, 216–221.

Roney, I. J., Rudner, A. D., Couture, J.-F., & Kærn, M. (2016). Improvement of the reverse tetracycline transactivator by single amino acid substitutions that reduce leaky target gene expression to undetectable levels. *Scientific Reports*, 1–8. http://doi.org/10.1038/srep27697

Schachtman, D.P., Schroeder, J.I., Lucas, W.J., Anderson, J.A., and Gaber, R.F. (1992). Expression of an Inward-Rectifying Potassium Channel by the Arabidopsis KAT1 cDNA. Science *258*, 1654–1658.

Scheres, S.H.W. (2012). RELION: Implementation of a Bayesian approach to cryo-EM structure determination. J. Struc. Biol. *180*, 519–530.

Scheres, S.H.W., and Chen, S. (2012). Prevention of overfitting in cryo-EM structure determination. Nat. Methods *9*, 853–854.

Shaya, D., Kreir, M., Robbins, R.A., Wong, S., Hammon, J., Brüggemann, A., and Minor, D.L. (2011). Voltage-gated sodium channel (NaV) protein dissection creates a set of functional pore-only proteins. Proc. Natl. Acad. Sci. U.S.A *108*, 12313–12318.

Shih, T.M., Smith, R.D., Toro, L., and Goldin, A.L. (1998). High-Level Expression and Detection of Ion Channels in *Xenopus* Oocytes. Meth. Enzymol. *293*, 529–556.

Urlinger, S., Baron, U., Thellmann, M., Hasan, M. T., Bujard, H., & Hillen, W. (2000). Exploring the sequence space for tetracycline- dependent transcriptional activators: Novel mutations yield

expanded range and sensitivity. *Proceedings of the National Academy of Sciences*, *97*(14), 7963–7968.

Vargas, E., Yarov-Yarovoy, V., Khalili-Araghi, F., Catterall, W.A., Klein, M.L., Tarek, M., Lindahl, E., Schulten, K., Perozo, E., Bezanilla, F., et al. (2012). An emerging consensus on voltage-dependent gating from computational modeling and molecular dynamics simulations. J. Gen. Physiol. *140*, 587–594.

Wainger, B. J., Degennaro, M., Santoro, B., Siegelbaum, S. A., & Tibbs, G. R. (2001). Molecular mechanism of cAMP modulation of HCN pacemaker channels. *Nature*, *411*, 805–810.

Whicher, J.R., and MacKinnon, R. (2016). Structure of the voltage-gated K+ channel Eag1 reveals an alternative voltage sensing mechanism. Science *353*, 664–669.

Xu, H., Hackos, D.H., Koth, C.M., Xu, H., Li, T., Rohou, A., Arthur, C.P., Tzakoniati, F., Wong, E., and Estevez, A. (2019). Structural Basis of Nav1.7 Inhibition by a Gating-Modifier Spider Toxin. Cell *176*, 702–715.

Zheng, S.Q., Palovcak, E., Armache, J.-P., Verba, K.A., Cheng, Y., and Agard, D.A. (2017). MotionCor2: anisotropic correction of beam-induced motion for improved cryo-electron microscopy. Nat. Methods *14*, 331–332.

Chapter 4: Towards the structural and functional characterization of the hyperpolarization-activated K^+ channel MVP

Multiple scientists contributed to the work presented here. They include Shane Gonen, Tamir Gonen, Dan Shi, Pedro Rodriguez, and Jason F. Xiao.

Abstract

The voltage-gated ion channel (VGIC) constitutes the molecular basis of cellular excitability and intercellular electrical communication. Structurally, VGICs comprise two essential domains: (1) a voltage-sensing domain (VSD) which undergoes a conformational change in response to changes in the membrane potential, and (2) a pore domain that allows conductance of ions across the membrane. We seek to understand how a conformational change in the VSD opens or closes the pore domain; a process termed electromechanical coupling. We use as a model system an archaeal potassium channel, MVP, which is activated by membrane hyperpolarization, ie activated with the opposite polarity to the majority of ion channels of known structure. Here we present our progress in elucidating the structure of MVP, as well as understanding the function of MVP and its prokaryotic and archaeal orthologs. We determined that an MVP-KcsA chimera Fab complex can be purified to homogeneity and its structure resolved to sub nanometer resolution by cryo-EM. In this protein, the inner gate appears closed, and the channel adopts a non-domain-swapped configuration of its VSDs with respect to its pore domain. We conclude that a non-domain-swapped architecture is a universal feature of hyperpolarization-activated ion channels.

Introduction

VGICs are tetramers comprised of four voltage sensing domains (VSDs) and one central pore domain (figure 1) (MacKinnon 1991; Long et al. 2005). The S4 segment of each VSD contains a string of evolutionarily-conserved arginine residues, termed gating charges, which have been shown to move in response to changes in membrane voltage (Bezanilla 2008). While the detailed mechanism of voltage sensing is debated, it is clear that the S4 segment moves in response to change in membrane potential (Guo et al. 2014; Li et al. 2014; Jiang et al. 2003). This outward movement upon membrane depolarization of the S4 helix / paddle is coupled mechanically to the pore domain through a short, intervening linker, leading to pore opening in the classic channel type, which is activated by membrane depolarization (Blunck and Batulan 2012). Additionally, a host of structural and mechanistic studies have provided a consensus model of opening and closing of the ion conduction pore via dilation or constriction of the central helical bundle crossing at the intracellular end of the channel (Yifrach and MacKinnon 2002).

Yet, the question of how VSD motion is coupled to pore activation remains more obscure. Functional studies have provided valuable insights into this process, termed electromechanical coupling. Multiple, distinct interactions between VSD and pore have been suggested to be required for coupling, and evolutionary covariation between VSD and pore has been a subject of debate (Lee et al. 2009). Notably, channel chimeras between the VSD of shaker and the pore domain of KcsA showed that the VSD of a voltage-sensitive channel could confer voltage sensitivity to a pore domain from a distantly-related, non-voltage sensitive bacterial channel. Successful coupling was only achieved when the C-terminal portion of the S6 pore helix of KcsA was replaced by that of Shaker (Caprini et al. 2001, Lu et al. 2001). When analyzed in the context of the Kv1.2 crystal structure, Long et al. suggested that contacts between the S4-S5 linker and the distal S6 of the adjacent subunit were required to couple the VSD to pore (Long et

al. 2005, Lu et al. 2001). However, chimeras between the VSD of a voltage-sensitive phosphatase and the non-voltage gated pore domain viral KCV channel show behavior which mimics that of a K_v channel, and coupling is independent of the sequence of the VSD-pore linker (Arrigoni et al. 2013). Furthermore, mutant cycle analysis of shaker has pinpointed contacts between the S4S5 linker and S6 segment of the same subunit (Chowdhury et al. 2014), in contrast to the conclusions of the MacKinnon group (Long et al. 2005; Lu et al. 2001). Thus, the general consensus is that contacts between the S4-S5 linker and the S6 pore-forming segment are crucial for coupling, however the detailed nature of these interactions, the conformational rearrangement of the S4-S5 linker and S6 upon channel opening/closing, and finally the importance of other VSD-pore contacts are unknown or disputed (Blunck and Batulan 2012; Vardanyan and Pongs 2012).

We have attempted to elucidate this coupling mechanism by structurally characterizing MVP, a hyperpolarization-activated potassium channel from Methanocaldococcus Janaschi. MVP is activated with opposite polarity to most ion channels of known structure and can provide insight into how an inward movement of the S4 segment might open a pore (Sesti et al. 2003). MVP may also serve as a minimalist model system of a hyperpolarization-activated ion channel; at only 211 amino acids in length, the channel must terminate immediately after its S6 helix, leaving no room for a C-linker or CNBD (like those found in HCN and KAT1 channels). Additionally, MVP contains a remarkably short S4-S5 linker between VSD and pore domains (**Fig. 4-1**), and presents an opportunity to observe a potentially novel mode of coupling between these two elements.

Figure 4-1

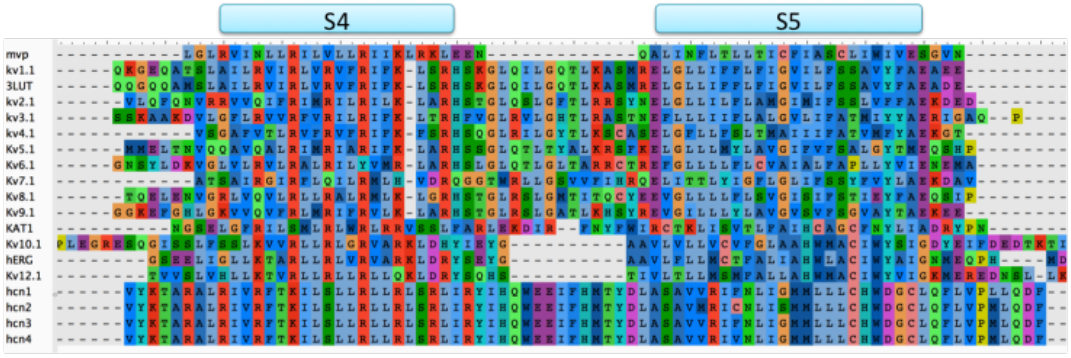

Figure 4-1: Multiple sequence alignment of selected Kv channels
Note the range of S4-S5 linker lengths, of which MVP (top row) is the shortest.

In this chapter we describe our efforts to elucidate the structure of MVP using X-ray crystallography and cryo-EM. While we were unsuccessful in attaining high resolution, we provided evidence that MVP adopts a non-domain-swapped architecture, paralleling that seen in HCN1 and KAT1, indicating that this architecture is a universal feature of hyperpolarization-activated channels. We also present preliminary functional and biochemical data on a series of MVP orthologs that may prove useful in subsequent studies of VSD-pore coupling.

Results and Discussion

Preliminary efforts in crystallization of MVP

The MVP gene hails from an archaeal thermophile, and expresses protein at high levels in E. coli. Purified protein is stable in maltoside detergents for weeks (Randich et al. 2014) and presents an attractive target for crystallography. Thus, we embarked an extensive and unsuccessful endeavor, employing standard vapor diffusion crystallization in a variety of detergents, in presence and absence of a synthetic antibody Fab fragment, bicelle, lipidic cubic phase, and high-detergent-lipid mixture crystallization protocols (Hunte and Michel 2002; Ujwal and Boxie 2011; Landau and Rosenbusch 1996; Gourdon et al. 2011). Results are shown in **Fig. 4-2**, and additional details are provided in the methods sections. Crystallization experiments were eventually abandoned in favor of cryo-EM experiments described below.

Design and characterization of an MVP-KcsA chimera Fab complex

At the time, we considered it essential to increase the size of our membrane protein complex for cryo-EM analysis. In addition, we wanted to break the additional pseudo-two fold rotational seen at low resolution for a flat membrane protein (i.e. at low resolution, a flat membrane protein will look the same upside down as it will right side up, unless there is some soluble domain to facilitate proper alignment). We now know this thinking to be partly fallacious; there now exist several examples of relatively flat membrane proteins have since been solved. However, at the time we proceeded to construct chimeras in which the C-terminal four-helix bundle, or stalk, of the KcsA channel was grafted onto the C-terminus of MVP (**Fig. 4-3**). Multiple MVP-stalk registers were tested, and the shortest register that still expressed robustly (termed AV) was carried further for analysis (see methods section for details of construct design). The function of the chimera was tested using an E. coli strain (LB2003) deficient in potassium uptake.

Figure 4-2

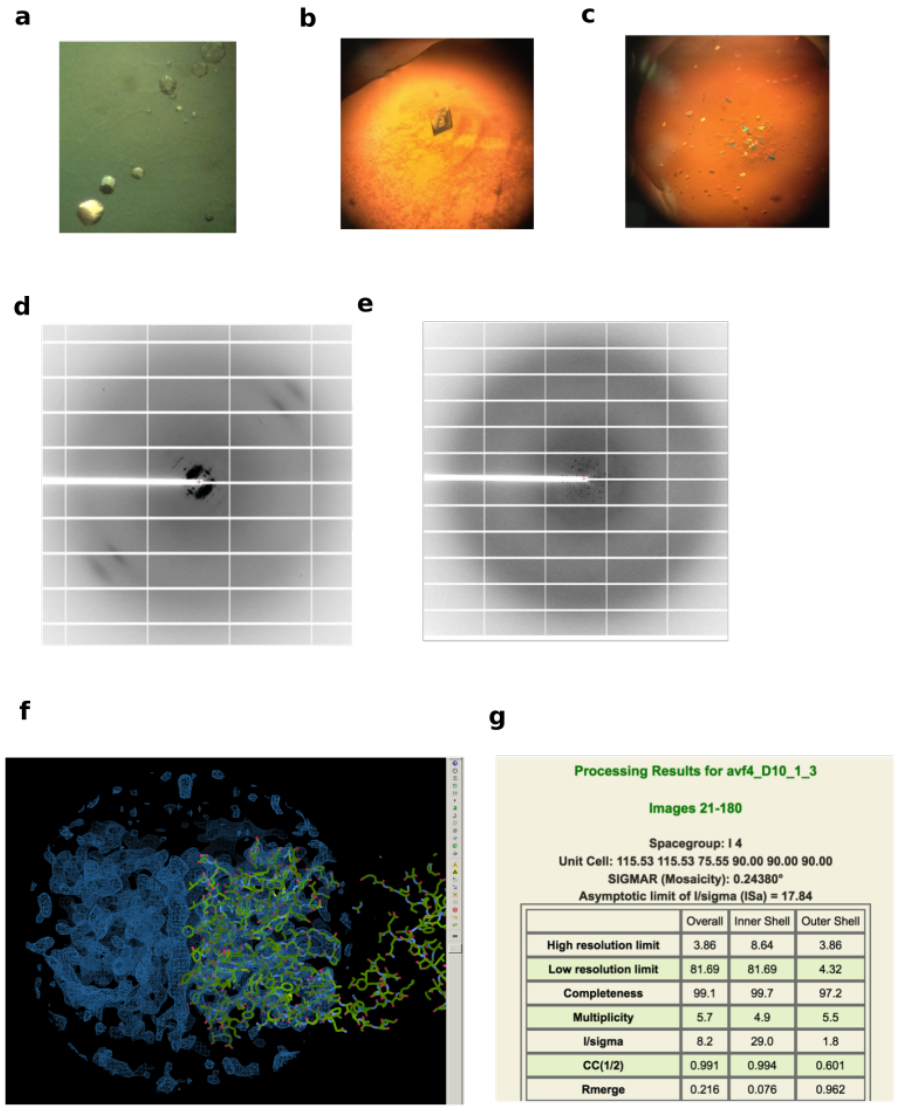

Figure 4-2: Initial efforts in MVP structure determination by X-ray crystallography

a,b,c Various crystal forms of MVP and MVP-Fab complexes. **d,e** Representative diffraction patterns for wt-MVP (**d**), and MVP-Fab12(**e**). **f,** Unrefined, unmodified electron density post molecular replacement of a ~4 Ang dataset of MVP-KcsA chimera – Fab4 complex. Density for the stalk and Fab4 are seen, while any density from the MVP portion is absent. **g,** RAPD processing results for dataset shown in **f**. See methods section for details.

Figure 4-3

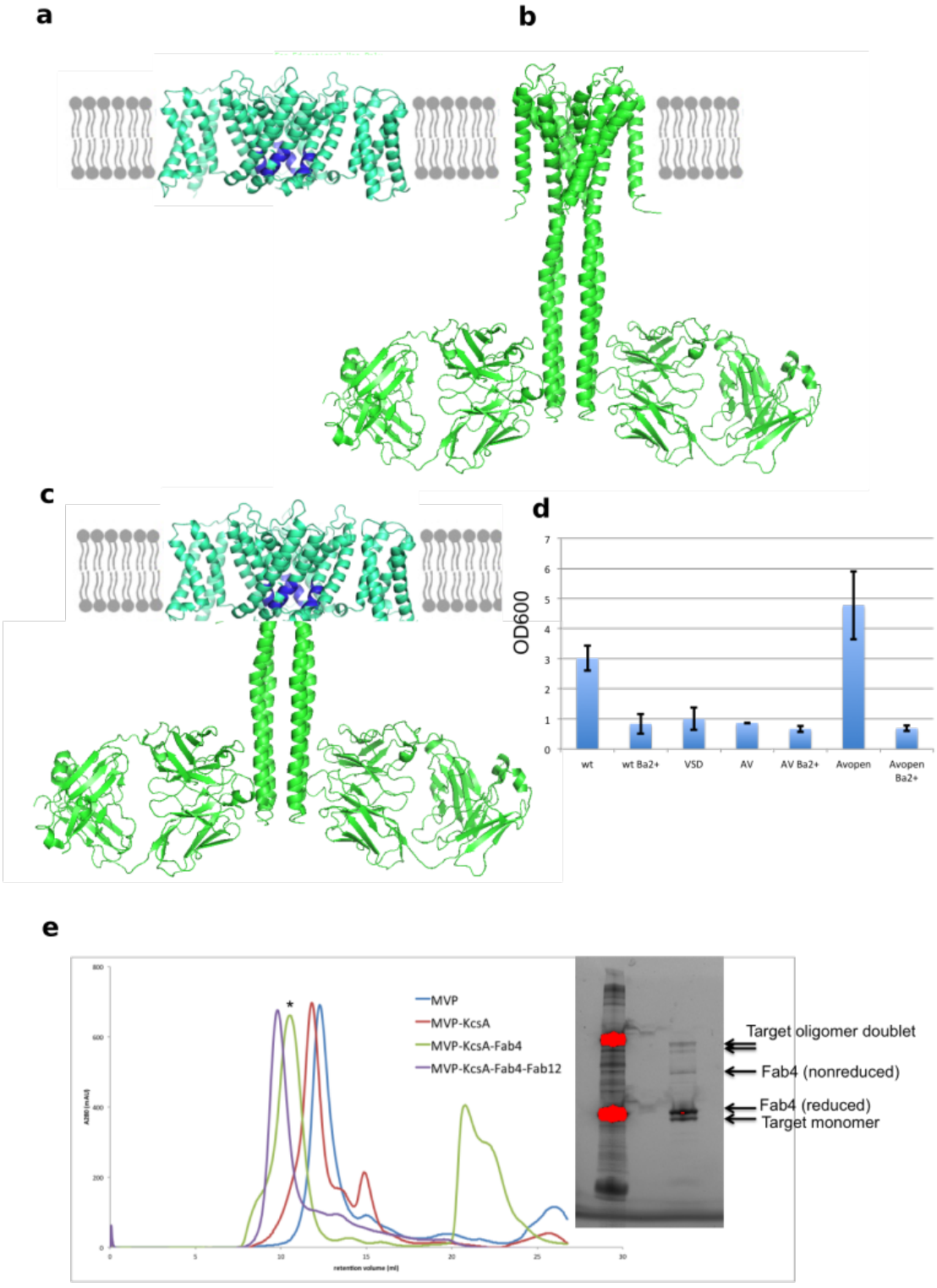

Figure 4-3: Design, function and biochemistry of MVP-KcsA chimeric Fab complexes

Figure 4-3, continued.

a, Homology model of MVP. Note the absence of any C-terminal domain, due to the short overall sequence length of MVP. **b,** Structure of the full-length KcsA-Fab2 complex (PDBID:3EFF) (Uysal et al. 2009). Note C-terminal 4-helix bundle, or stalk, bound to two fabs. **c,** Schematic of MVP-KcsA chimera design, in which the KcsA stalk was grafted to the MVP C-terminus. **d,** LB2003 liquid growth assay demonstrating function of MVP-KcsA chimera, AV. AVopen contains mutations in KcsA stalk which constituitively open the channel (Cuello et al. 2010). **e,** SEC and SDS-PAGE analysis of MVP-KcsA chimeric Fab complexes. In the SEC traces, successive shifts are seen upon addition of the stalk (red), Fab4 (green, binds to KcsA stalk with 4:4 stoichiometry Uysal et al. 2009)), and Fab4 plus Fab12 (purple, Fab12 binds MVP directly (Uysal thesis, Kossiakoff laboratory UChicago)). The MVP-KcsA-Fab4 sample was used for cryo-EM experiments.

Similar to the yeast strain described in chapter 3, LB2003 requires high external K^+ concentrations, or expression of a conductive K^+ conduit to grow (Stumpe and Bakker 1997). When tested in an LB2003 liquid growth assay format, MVP-KcsA chimera complements poorly. A variant of the chimera in which charged residues are mutated to splay open the stalk (mutations shown to generate a constitutively-open KcsA channel) allow for complementation comparable to the wildtype MVP (**Fig. 4-3d**). We conclude that the chimera is functional (in the sense that it can be opened), and that the introduction of the stalk stabilizes a closed inner gate. The AV chimera displays robust biochemical behavior, and a variety of Fab complexes can be

generated (**Fig. 4-3e**). For cryo-EM analysis, we chose to use Fab4, shown to bind KcsA in a 4:4 stoichiometry (Uysal et al. 2009). Addition of Fab4 would likely facilitate particle alignment at low resolution, and when vitrified in cryo-EM grids, gave single, well-dispersed particles. This was a contrast to the apo-MVP protein, or even apo-AV chimera, which both tended to stack via their soluble loops (data not shown).

Cryo-EM analysis of MVP-KcsA chimera Fab4 complex

We collected several large datasets on a 200 keV Talos microscope with side entry holder and Falcon II camera (that gave ~1 nm resolution maps). We believed the resolution to be limited to hardware and user expertise in microscope operation. We then collaborated with Shane and Tamir Gonen at Janelia, who collected a large dataset on an optimized sample. After extensive processing, a nominally sub nanometer map was obtained (**Fig. 4-4**). We suspect that our resolution is limited by conformational flexibility / heterogeneity that is likely continuous in nature. This is seen clearly in the 2D class averages, in which the Fabs adopt many different orientations relative the TMD/micelle. In fact, in 2D classes in which the TMD/micelle are well resolved, the Fabs are blurry.

Figure 4-4

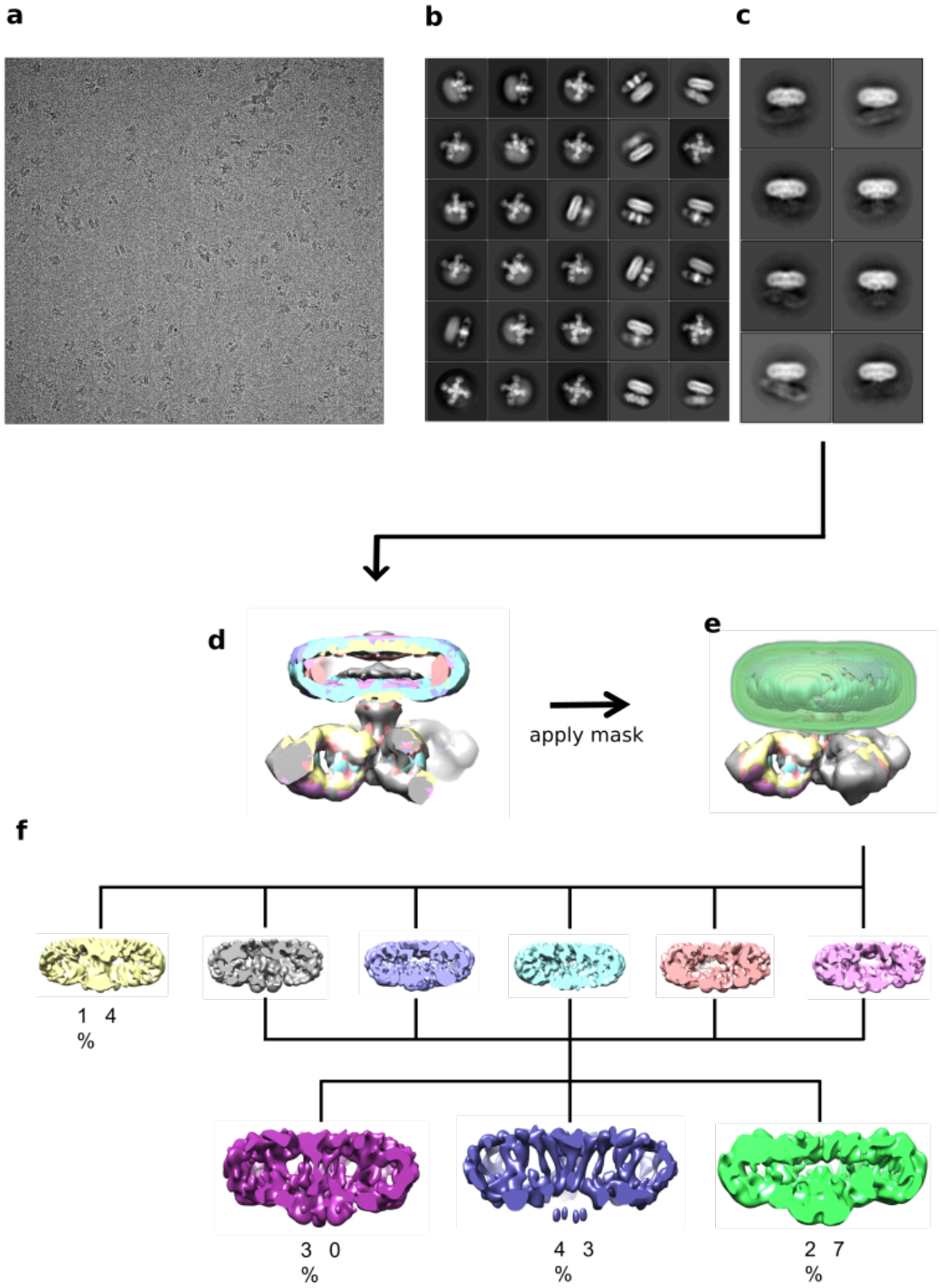

Figure 4-4: MVP-KcsA-Fab4 cryo-EM dataset

Figure 4-4, continued.

a, Representative micrograph **b,** Reference-free 2D classification **c,** 2D classification post signal subtraction of Fab4 density. **d,** 3D classes of full molecule, with C4 symmetry imposed. Note micelle is empty. **e,** 3D classes of full molecule, with TMD-focused mask (green) shown. **f,** Cascade of 3D classification after masking and local alignment. Details of processing procedure are in the methods section.

The opposite is also seen, in 2D classes in which the Fabs are well resolved, the TMD/micelle are blurry. Signal subtraction of the Fabs after consensus 3D alignment improved the quality of the 2D averages (**Fig. 4-4c**), yet only somewhat improved the quality of the 3D classes. The most effective strategy to improve the quality of the TMD region was to mask out the Fabs and continue the classification with local angular searching; such the particle alignments were allowed to vary locally, as global re-alignment post masking allowed for flipping of the TMDs. This approach, combined with two rounds of 3D classification allowed visualization of sausage-like densities for transmembrane helices. Pore helices S6 and S5 are individually resolved, while the VSD S1-S4 helices are somewhat discontinuous.

While the MVP EM density map is low resolution, we can derive a few biological conclusions (**Fig. 4-5**). First, the inner gate, formed by the S6 appears to be closed/nonconductive. This is

expected; MVP natively is closed at 0mV, and the LB2003 assay results suggest that MVP-KcsA is closed, even at negative potentials. Additionally, while hard to visualize, the volume of inner cavity of the MVP pore domain is small. This was also observed in KAT1em (chapter 2). Finally, when the MVP map is aligned with a low-pass-filtered map of HCN1 (to allow for a fair comparison), the TM helices align quite well (**Fig. 4-5b**) (Lee and MacKinnon 2017). This suggests that MVP, like HCN1 and KAT1, is non-domain-swapped. Thus, it appears that a non-domain-swapped architecture is a universal feature of hyperpolarization-activated ion channels. In fact, MVP-like, KAT1-like and HCN-like channels form the entirety of known hyperpolarization-activated ion channels.

Figure 4-5

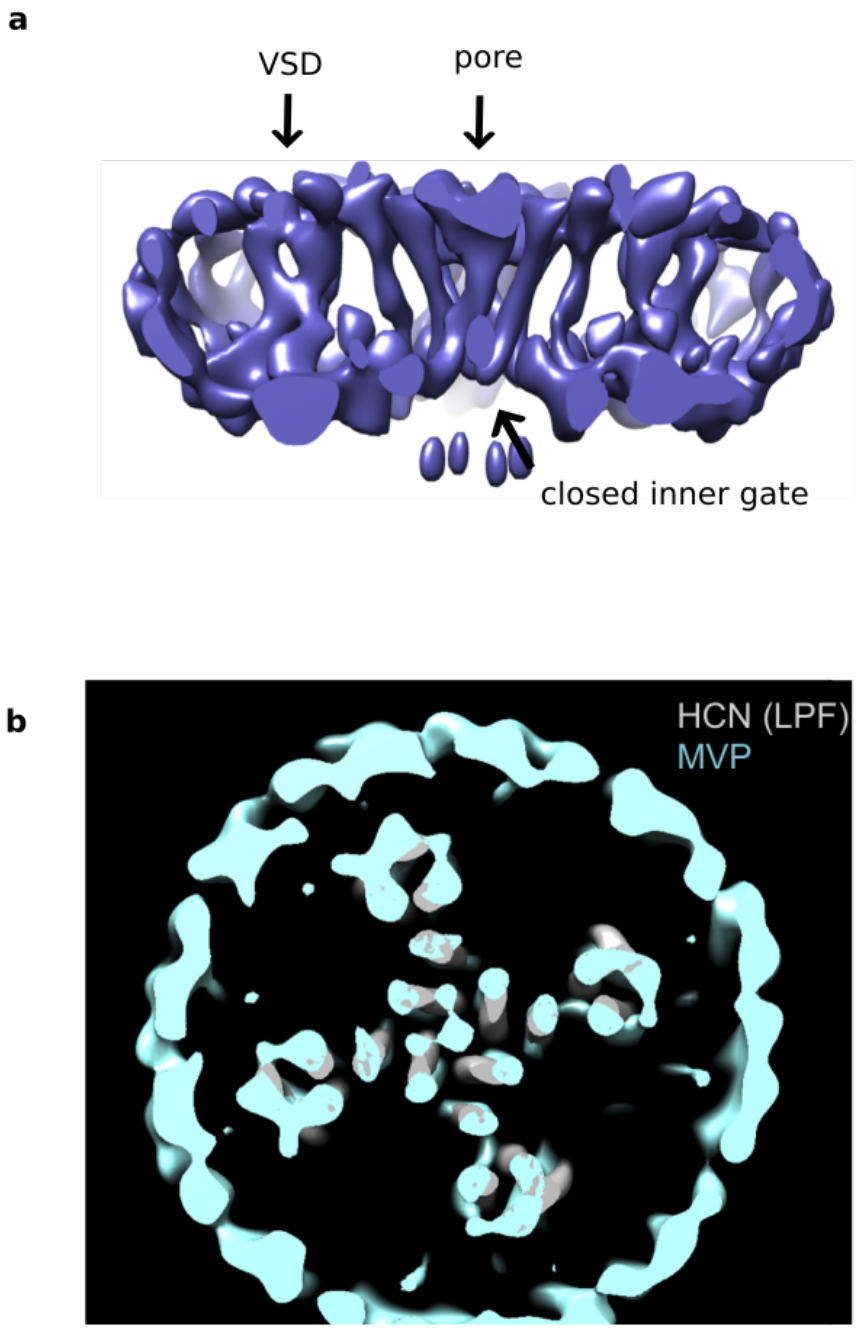

Figure 4-5: MVP-KcsA-Fab4 cryo-EM: preliminary biological interpretation

a, Best 3D class map, derived from ~272k particles. The inner gate appears to be in a closed/non-conductive conformation. **b,** Overlay of best MVP map with a low-pass-filtered map of hsHCN1 (Lee and MacKinnon 2017). Note good correspondence of TM helices between the maps, indicating that MVP, like HCN, is likely non-domain-swapped.

Preliminary functional and biochemical studies of MVP orthologs

Little is known about the structure and function of other MVP-like channels. BLAST (Altschul et al. 1990) and Jackhmmer (Johnson et al. 2010) searches of MVP against prokaryotic and archaeal protein sequences return numerous sequences. We synthesized eight of these sequences, systemically varying the global sequence identity and S4-S5 linker length between orthologs (**Fig. 4-6**). We tested the ability of these orthologs to complement LB2003 growth in the plate assay format, as well as attempted overexpression and purification following protocols established for wild-type MVP (**Fig. 4-6**). Multiple orthologs complemented LB2003, for the ones that did not, we cannot rule out lack of surface expression, however it is possible that non-complementers might be activated by depolarization and thus are closed at the negative resting potential of LB2003 *E. coli*.

Next, we took the sequences of four proteins which complemented the LB2003 (MVP, miVP, maVP, rhVP) and generated chimeras in which VSDs and pore domains were separately swapped among the proteins, resulting in 12 chimeras, in addition to the 4 wild type proteins. The ability of these 16 constructs to complement LB2003 was determined, and the results displayed in the 4x4 grid in **Fig. 4-7b**. Trivially, all the wildtype proteins (diagonal, green) complemented. Intriguingly, several combinations failed to complement, potentially indicating some specific contacts between VSD and pore domain that might co-vary between these different orthologs. An interesting future direction will be to substitute point mutations in these non-complementers (red squares) to re-rescue the complementation phenotype. Finally, we tested the biochemical behavior of a number of these orthologs, some with C-terminal mass tags included, as a prelude to further structural analyses **Fig. 4-7c,d**.

Figure 4-6

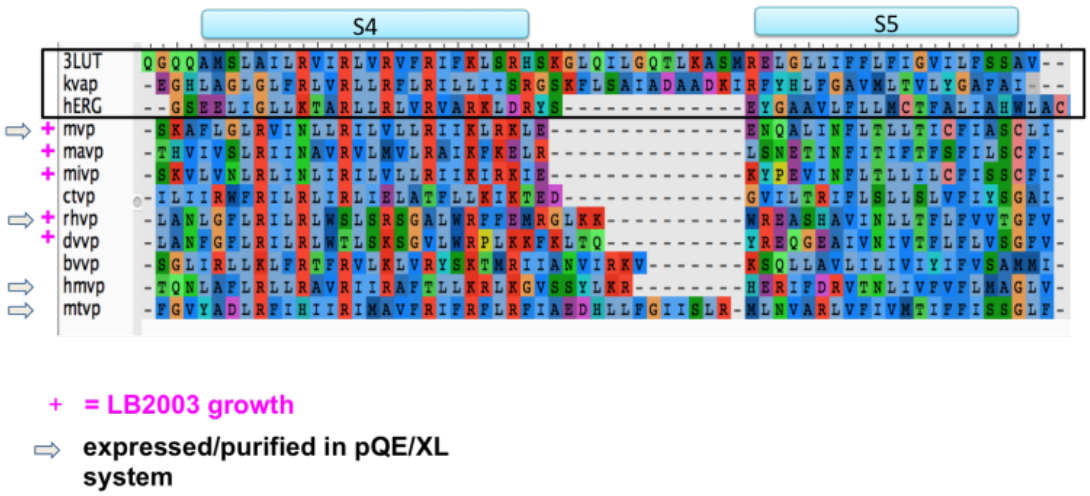

Figure 4-6: Multiple sequence alignment of three K_v channels, MVP and eight prokaryotic/archael MVP orthologs

Note the array of S4-S5 linker lengths among orthologs. Orthologs that complemented LB2003 potassium deficiency are denoted with a magenta "+". Orthologs that could be successfully expressed and purified in *E. coli* are indicated with gray arrows.

Figure 4-7

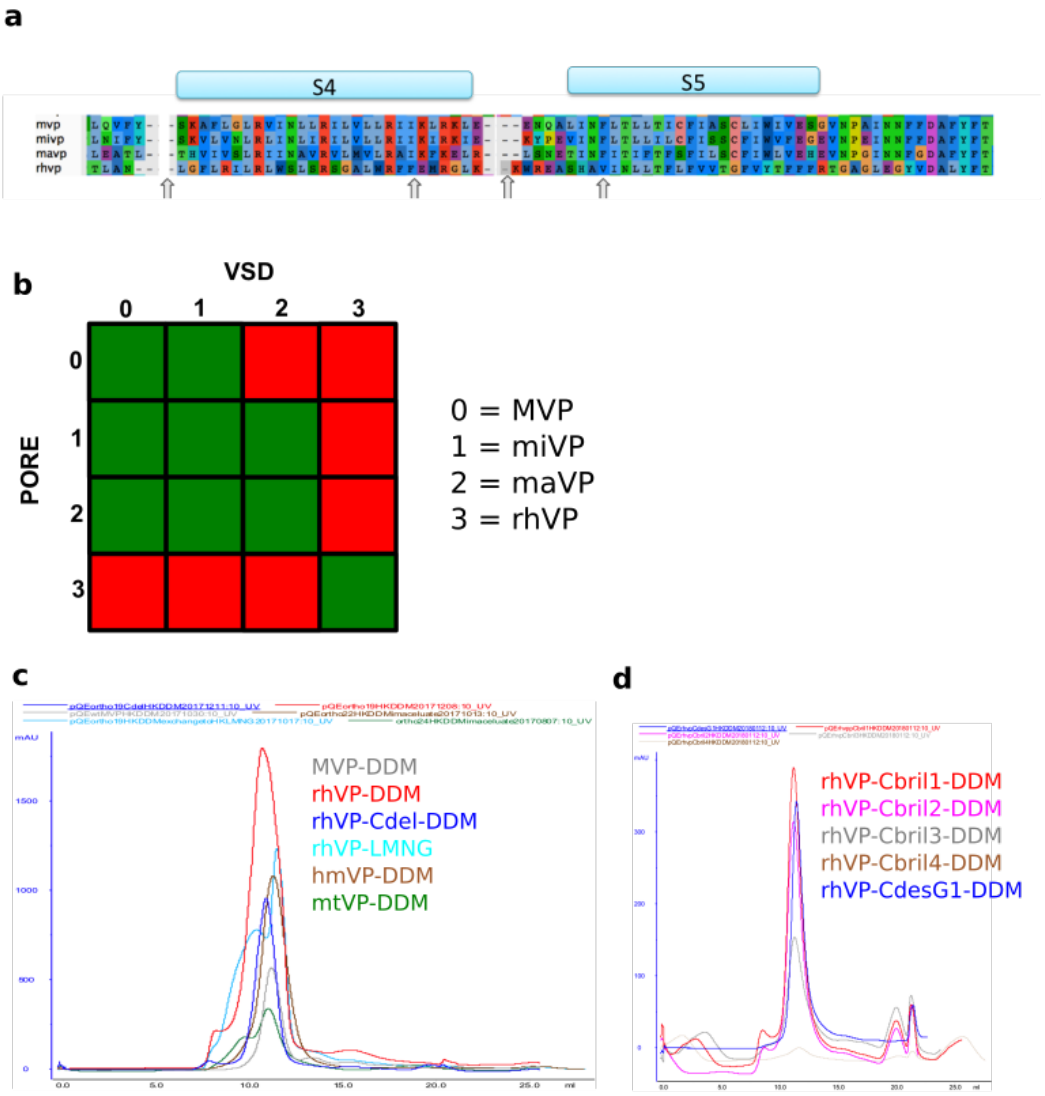

Figure 4-7: MVP ortholog chimera design, LB2003 assay and ortholog biochemistry

a, Multiple sequence alignment of MVP and three orthologs (miVP, maVP, rhVP) all of which complement LB2003, and were used for construction of chimeras. **b,** Results of LB2003 assay on chimeras. VSD-pore chimeras between the four proteins were generated (12 chimeras, plus the four wildtype proteins for the 16 squares in the grid). All 16 constructs were tested in the LB2003 assay in plate format. Constructs which complement are green squares, constructs which failed to complement are red squares. **c,** SEC traces for MVP and several orthologs. **d,** SEC traces for rhVP ortholog with various mass-tags at its C-terminus. Bril and desG are small, single domain proteins.

Conclusion

We generated and purified to homogeneity a MVP-KcsA chimera Fab and determined its structure to sub nanometer resolution by cryo-EM. In this protein, the inner gate appears closed, and the channel adopts a non-domain-swapped configuration of its VSDs with respect to its pore domain. We conclude that a non-domain-swapped architecture is a universal feature of hyperpolarization-activated ion channels. The mechanistic implications of MVP are intriguing in that it lacks a C-linker and CNBD. Thus, the direct coupling mechanism proposed for KAT1 in chapter 2 cannot apply to MVP. More likely, MVP may employ a mechanism based on zipper-like interactions between S4 and S5, as proposed for HCN mutants with C-linkers and CNBDs deleted. Thus, MVP highlights the diversity in putative coupling mechanisms, even within the hyperpolarization-activated subfamily.

Methods

MVP and MVP-KcsA biochemistry

A DNA construct encoding MVP codon optimized for E. coli expression was previously described (Randich et al. 2014). MVP biochemistry was performed essentially as described (Randich et al. 2014), with some modifications. Construct pQE60-MVP was transformed to XL10-gold cells, and grown overnight in liquid culture (without plating) with ampicillin. Overnight culture was then diluted into terrific broth media, grown at 37C to an OD600nm of 0.6-0.8, shifted to temperature 30C for 15min, and induced with 0.5 mM IPTG. Expression proceeded for 5 hrs, at which point cells were harvested by low speed centrifugation and frozen at -80C. Cell pellets were thawed and purified as described (Randich et al. 2014).

Extensive and unsuccessful efforts in crystallization of MVP were undertaken. Efforts included standard detergent crystallization of MVP in DDM, DM, LMNG, DMNG, Cymal6, in the absence and presence of Fab12 (Uysal thesis, Kossiakoff laboratory UChicago)). Bicelles, lipidic cubic phase and HiLiDe methodology were also attempted. The best diffracting crystals for apo-pQE60-MVP-C-His were grown in memgold 1-D5: 24% PEG400, 50mM NaOAc pH 5.4, 50 mM MgOAc (Diffraction pattern shown in **Fig. 4-2d**). The best diffracting crystals for pQE60-MVP-C-His+Fab12 complex were grown in a custom screen containing 10% PEG 4000, 25mM BIS-TRIS propane pH7, 0.875M NH4Cl (Diffraction pattern shown in **Fig. 4-2e**). Additionally, crystallization of the MVP-KcsA chimera – Fab4 complex (discussed below) was attempted. Crystals were grown in DMNG, 20% PEG3350, 50mM HEPES pH 7, 0.2M NH4NO3, which diffracted to ~4 Ang, and while density for the stalk and Fab4 are seen after molecular replacement, any density from the MVP portion is absent. Proteolysis is suspected, as the crystal took more than one month to reach full size.

MVP-KcsA chimeras were generated by megaprimer loopin PCR cloning to fuse the KcsA stalk onto a pET15b-N-His6-thrombin-MVP construct. Multiple fusion points were generated, with the best behaving fusion termed AV (A205:V115, MVP:KcsA). Other fusions included KV (K204:V115, MVP:KcsA), LA (L202:A108, MVP:KcsA), LT (L202:T112, MVP:KcsA), QA (Q203:A109, MVP:KcsA), QR (Q203:R117, MVP:KcsA), KG (K204:G116, MVP:KcsA), KT (K204:T112, MVP:KcsA), GT (G208:T112, MVP:KcsA), GW (G208:W113, MVP:KcsA). pET15b-MVP-KcsA constructs were expressed in Rosetta2 Codon+ cells, at 37C for 3hrs after IPTG induction. Purification was as described (Randich et al. 2014), except that for cryo-EM studies the final SEC step was run in HEPES pH7.4, 200mM KCl, 0.05% DDM (anatrace) 0.01% CHS (anatrace), asolectin (avanti) 0.05mg/ml. Purified protein was mixed with purified KcsA fabs (Fab4) with a 0.2 molar excess of Fab, and run in above SEC buffer. Protein was concentrated prior to SEC such that the peak fraction, when collected was 4-5 mg/ml, and required no concentration after SEC. This manipulation was critical in minimizing aggregation on the cryo-EM grid.

MVP-KcsA-chimera Fab4 complex cryo-EM

Purified complex, as described above, was prepared for cryo-EM using a number of grid types, including C-flat 200 mesh 1.2/1.3 (EMS), C-flat 400 mesh 1.2/1.3 (EMS), and Quantifoil 200mesh 1.2/1.3 grids. Quantifoil 200mesh 1.2/1.3 grids (Quantifoil) gave the most reproducible results, and had the fewest number of broken squares, when compared to the C-flat grids. Grids were plasma cleaned for 30sec in an air mixture. Grids were frozen in liquid nitrogen-cooled liquid ethane in a Vitrobot Mark IV (FEI) using the following parameters: sample volume 3.5ul, blot time 2.5sec, blot force 3, humidity 100%, temperature 22C and double filter papers on each side of the vitrobot. Parameters were varied to some degree, and blot time typically ranged from 1-4sec.

Grids were screened on a 200 kV Talos side entry microscope (FEI) equipped with a Falcon II direct detector (Gatan) using a Gatan 626 single-tilt holder. Replicate grids from the same preparation were shipped to the laboratory of Tamir Gonen Janelia Farm research campus. Grids were imaged on a Titan Krios with K2 detector (super-resolution mode) at a nominal magnification that corresponded to a super-res pixel size 0.655 Å/pix. The dose rate was roughly 10e-/pix/s and the exposure time was 10 seconds, yielding a total dose of 58 e-/Å^2. A nominal defocus range of 1.2-2.5 micron was used, and 6349 movies were collected using SerialEM (Mastronarde et al. 2005). Data were processed using motioncor2, Ctffind4, and Relion 2 (Kimanius et al., 2016; Rohou and Grigorieff, 2015; Scheres, 2012; Zheng et al., 2017). 3,000 particles were manually picked and classified in 2D to generate autopicking templates. Autopicking in Relion2 gave ~930k Particles, and micrographs were subsequently manually cleaned and 2D classified, resulting in ~683k particles which were subjected to a number of different 3D classification schemes. Despite extensive efforts, the best 3D maps were low-resolution, nominally ~9 Å resolution. Masking, focused classification with and without global or local alignment, signal subtraction of Fabs or detergent micelle belt were all attempted. Focused classification with local alignment was critical in resolving transmembrane helices, without it the micelle appeared empty. The final map was derived from a 3D class (resolution tended to degrade during 3D auto_refine) with ~272k particles and imposed C4 symmetry.

MVP ortholog selection, molecular biology and biochemistry

The sequence of MVP was used as a query for proteinBlast (Altschul et al. 1990) searches against prokaryotic non-redudant protein sequences, as well as in Jackhmmer (Johnson et al. 2010) for three iterations. Eight ortholog sequences were selected based on their S4-S5 linker lengths lying in between MVP and KvAP. Sequences were codon optimized for E. coli expression and synthesized by Integrated DNA Technologies. CDNAs were subcloned to

pQE60, bacterial expression vector with T5 promoter and C-terminal hexahistidine tag. Protein sequences are shown below, along with molecular weights (MW) and extinction coefficients (E).

>mvp
MNLKDRRLKKIMEVLSLIFTFEIVASFILSTYNPPYQDLLIKLDYISIMFFTFEFIYNFYYVEDKAKFF
KDIYNIVDAIVVIAFLLYSLQVFYSKAFLGLRVINLLRILVLLRIIKLRKLEENQALINFLTLLTICFIAS
CLIWIVESGVNPAINNFFDAFYFTTISITTVGYGDITPKTDAGKLIIIFSVLFFISGLITSLQKALKGDR
SHHHHHH
MW: 25.2KDa
E: 22

>miVP
MGKIKELLSLIFTLEIAISFILSTYHIHSQVLFILDYIAILYFTFETLYNFYKAKCKKEFFKDIYNIIDTIVI
IAFVLYTLNIFYSKVLVNLRLINLIRILVLLRIIKIRKIEKYPEVINFLTLLILCFISSCFIWVFEGEVNPEI
NNFFDAFYFTTISITTVGYGDITPKTEAGKLIIIFSVLLFISGIITSIQKALRGEDGNSRSHHHHHH
MW: 24.8
E: 22

>maVP
MNRELHKKIYSPRIYRKIEFIVLLCTLEIIISFVISTYNPPYEALLFKLDFFSISFLTFEFIYRFVGSKN
KTKFFKDKYNLIDAFVIVAFIMYLLEATLTHVIVSLRIINAVRVLMVLRAIKFKELRLSNETINFITIFT
FSFILSCFIWLVEHEVNPGINNFGDAFYFTVVSLTTIGYGDITPMTSEGKLIIVLAVLYVISGLVSKA
KGFLHEEHRLYYENKKIKKKISRSHHHHHH
MW: 27.9
E: 23.5

>rhVP
MKAPESDGVQEFSALARLRDKLRKLYHGRTRAAFRFQLAAVIIDLAIIAFFIATPVIQESSSFLWL
DYSVAALVAVDMIARLLASNDMLRLMKQPTSWVDAFILLTLLMPTTLANLGFLRILRLWSLSRSG
ALWRFFEMRGLKKWREASHAVINLLTFLFVVTGFVYTFFFRTGAGLEGYVDALYFTVATVTTTG
FGDIVLPGIAGKLTAIVTMIIGISLFVRLAQALFRPNKVFFPCPQCGLQRHEADAVHCKACGHLLN
IPDEGDRSHHHHHH
MW: 30.9
E: 35

>bvVP
MTNRKKRIYEVIEVSNIGDDSSRAYDVMITVAVIVGLLPMTLKSESIYTRIIEFSTSLLFFVDYCVR
VYTADYKMGYKSVEAYIAYIFTPLAIFDLLSIVPVISLFLPVSGLIRLLKLFRTFRVLKLVRYSKTMRI
IANVIRKVKSQLLAVLILIVIYIFVSAMMIYQLEPDLFNNFFDALYWATISITTIGYGDISPVTTLGRMI
TMLSALVGMAVIALPTGIITAAYMNEINKKKSKYELRSHHHHHH
MW: 28.6
E: 29.3

>ctVP
MVDQPITLKKKLSHYLDDFDSLTGIIINLIILGLILLSFLIFVVETYPISESLLIRLKQLDKIILLVFTLEYI
IRFWCSDNKLRFLFSFFSWIDLLAIVPLFVGFLDIRYILIIRWFRILRLIRLIELATFLLKIKTEDGVILT

RIFLSLLSLVFIYSGAIYQIEHQTNPQIFQNFFDALYFSIVTMTTVGFGDVTPLSETGKFITLMMILS
GIILIPWQISILTQQLLKITNKSPKLCFHCGLTVHEHDANFCKICGAKLENNEQIISQRRSHHHHHH
MW: 32.5
E: 32.4

>hmVP
MSERKGLNRRLFWLYEGHGPAPYYFRIGLLTFDVLTIAYFLWAPFRGDGVSHPVADYAIGAIIAL
DLAARFYIAQPRTKFWRRLYNWADIIVVISMLAPLFTQNLAFLRLLRAVRIIRAFTLLKRLKGVSSY
LKRHERIFDRVTNLIVFVFLMAGLVFVLQKDTNPGIENYVDALYFTVTSLTTTGYGDILMEGVWG
RLLAVVIMVLGLTLFLRLLRAITLPGGKIDYTCEACGLTRHDMDAIHCKHCGAMLKIETEGRGRS
HHHHHH
MW: 30.7
E: 45.4

>dvVP
MDEAKPEHGLTRLRSTLRLLYHGSSTTALRFQFAVLLVDLAIIAFFIATPLLRDRPSFIWIDIAVAV
LLVADLVARALASTDPLRWLRQPTTIVDIFILITLLLPAWLANFGFLRILRLWTLSKSGVLWRPLKK
FKLTQYREQGEAIVNIVTFLFLVSGFVLTFFGSTDTGIEGYVDALYFTVTSVTTTGYGDVTLPGTA
GRLTSIAVMIVGITLFVRLAQSLFRPHKVFFPCPQCGLQRHEPDAVHCKACGHVLNIPDPGNRS
HHHHHH
MW: 30.2
E: 35.2

>mtVP
MSGKADRCAGTRSLRETIQFYMIDFRTPLGRAIDIAIIALNIMVVVLFVIETYPLPSRISLLLWRLEI
AIIFIFMIEYILRFYGAPDRWSYVKETYSLIDLVAIMPTLILLVLPIFGVYADLRFIHIIRIMAVFRIFRF
LRFIAEDHLLFGIISLRMLNVARLVFIVMTIFFISSGLFYFAESPVNPEVNNFGDAFYFTVVAVSTV
GFGDIVPVSGAGRLVTLMMIISGIILIPIQVSRILREWISAPRKRHICSGCGQEWHEEDARYCRIC
GSPLGEESVTSQDAAERSHHHHHH
MW: 33.9
E: 36.9

Orthologs were expressed and purified in a manner analogous to wild-type MVP. Ortholog rhVP was also engineered to include C-terminal mass tags. These included bril, and desG (a ultra-stable protein G designed by the Shaw, Baker and Sosnick labs) (Chun et al. 2012; Lindorff-Larsen et al. 2011; Nauli et al. 2009; Riback et al. 2017).

Ortholog chimeras were generated by megaprimer loopin PCR, exchanging VSDs and pore domains between MVP (0), miVP (1), maVP (2), and rhVP (3). This subset of orthologs was selected due to their ability to complement LB2003 growth in a plate assay format, described below.

E. coli complementation experiments (LB2003)

E. coli strain LB2003 (Stumpe and Bakker 1997) was transformed with various pQE60 plasmid constructs, and grown overnight in LB media supplemented with 100 mM KCl. The following morning, cells were collected by low speed centrifugation, and washed twice in nominally K^+-free assay liquid media. Cells were resuspended in this assay media, and diluted to an OD600nm of 0.1. Then, 100 ul of 0.1 OD was plated. Colonies were counted 24-48hrs after plating. Final recipes (Based on thesis of Amelia Randich, Perozo lab) are shown here:

1X assay medium (g per L) (omit agar for liquid media)

NaH2PO4 3.18
Na2HPO4 12.32
NaCitrate 0.3
(NH4)2SO4 1.06
FeSO4-7H2O 0.0033
Agar 10

After autoclave, add (per L)

glucose(50%stock) 14.4ml
KCl(1M stock) 2ml
Thiamine 0.1g
Ampicillin 2ml

A kinetic growth assay was also conducted in LB2003 strain for MVP-KcsA fusions, in which LB2003-transformed cells were grown in LB media, in the presence / absence of 10mM BaCl2, and OD600nm monitored over time.

References

Altomare, C., Bucchi, A., Camatini, E., Baruscotti, M., Viscomi, C., Moroni, A., and Difrancesco, D. (2001). Integrated Allosteric Model of Voltage Gating of HCN Channels. J. Gen. Physiol. *117*, 519–532.

Altschul, S. F., Gish, W., Miller, W., Myers, E. W., & Lipman, D. J. (1990). Basic Local Alignment Search Tool. *Journal of Molecular Biology*, *215*, 403–410.

Arrigoni, C., Schroeder, I., Romani, G., Van Etten, J. L., Thiel, G., & Moroni, A. (2013). The voltage-sensing domain of a phosphatase gates the pore of a potassium channel. *The Journal of General Physiology*, *141*(3), 389–395. http://doi.org/10.1085/jgp.201210940

Bezanilla, F. (2008). How membrane proteins sense voltage. Nat. Rev. Mol. Cell Biol. *9*, 323–332.

Blunck, R., and Batulan, Z. (2012). Mechanism of electromechanical coupling in voltage-gated potassium channels. Front. Pharmacol. *3*, 1–16.

Caprini, M., Ferroni, S., Planells-Cases, R., Rueda, J., Rapisarda, C., Ferrer-Montiel, A., & Montal, M. (2001). Structural Compatibility between the Putative Voltage Sensor of Voltage-gated K+ Channels and the Prokaryotic KcsA Channel. *Journal of Biological Chemistry*, *276*(24), 21070–21076. http://doi.org/10.1074/jbc.M100487200

Chen, S., McMullan, G., Faruqi, A.R., Murshudov, G.N., Short, J.M., Scheres, S.H.W., and Henderson, R. (2013). High-resolution noise substitution to measure overfitting and validate resolution in 3D structure determination by single particle electron cryomicroscopy. Ultramicroscopy *135*, 24–35.

Chowdhury, S., and Chanda, B. (2012). Perspectives on: conformational coupling in ion channels: thermodynamics of electromechanical coupling in voltage-gated ion channels. J. Gen. Physiol. *140*, 613–623.

Chowdhury, S., Haehnel, B.M., and Chanda, B. (2014). Interfacial gating triad is crucial for electromechanical transduction in voltage-activated potassium channels. J. Gen. Physiol. *144*, 457–467.

Chun, E., Thompson, A. A., Liu, W., Roth, C. B., Griffith, M. T., Katritch, V., et al. (2012). Fusion Partner Toolchest for the Stabilization and Crystallization of G Protein-Coupled Receptors. *Structure (London, England : 1993)*, *20*(6), 967–976. http://doi.org/10.1016/j.str.2012.04.010

Cowgill, J., Klenchin, V. A., Alvarez-baron, C., Tewari, D., Blair, A., & Chanda, B. (2019). Bipolar switching by HCN voltage sensor underlies hyperpolarization activation. *Proceedings of the National Academy of Sciences of the United States of America*, *116*, 670–678. http://doi.org/10.1073/pnas.1816724116.

Cuello, L. G., Jogini, V., Cortes, D. M., Sompornpisut, A., Purdy, M. D., Wiener, M. C., & Perozo, E. (2010). Design and characterization of a constitutively open KcsA. *FEBS Letters*, *584*(6), 1133–1138. http://doi.org/10.1016/j.febslet.2010.02.015

Gourdon, P., Andersen, J. L., Hein, K. L., Bublitz, M., Pedersen, B. P., Liu, X.-Y., et al. (2011).

HiLiDe — Systematic Approach to Membrane Protein Crystallization in Lipid and Detergent. *Crystal Growth and Design*, *11*, 2098–2106.

Guo, J., Zeng, W., Chen, Q., Lee, C., Chen, L., Yang, Y., Cang, C., Ren, D., and Jiang, Y. (2016). Structure of the voltage-gated two-pore channel TPC1 from Arabidopsis thaliana. Nature *531*, 196–201.

Hunte, C., & Michel, H. (2002). Crystallisation of membrane proteins mediated by antibody fragments. *Current Opinion in Structural Biology*, 503–508.

Johnson, L. S., Eddy, S. R., & Portugaly, E. (2010). Hidden Markov model speed heuristic and iterative HMM search procedure. *BMC Bioinformatics*, *11*(1), 403–8. http://doi.org/10.1186/1471-2105-11-431

Kimanius, D., Forsberg, O., Scheres, S.H.W., and Lindahl, E. (2016). Accelerated cryo-EM structure determination with parallelisation using GPUs in RELION-2. eLife 1–21.

Landau, E. M., & Rosenbusch, J. P. (1996). Lipidic cubic phases: A novel concept for the crystallization of membrane proteins. *Proceedings of the National Academy of Sciences*, *93*, 14532–14535.

Latorre, R., Olcese, R., Basso, C., Gonzalez, C., Muñoz, F., Cosmelli, D., and Alvarez, O. (2003). Molecular Coupling between Voltage Sensor and Pore Opening in the Arabidopsis Inward Rectifier K+ Channel KAT1. J. Gen. Physiol. *122*, 459–469.

Lee, C.-H., and MacKinnon, R. (2017). Structures of the Human HCN1 Hyperpolarization-Activated Channel. Cell *168*, 111–120.

Lee, S.-Y., Banerjee, A., and MacKinnon, R. (2009). Two separate interfaces between the Voltage sensor and pore are required for the function of Voltage-dependent K+ channels. PLOS Biol. 7, 0676–0686.

Li, Q., Wanderling, S., Paduch, M., Medovoy, D., Singharoy, A., McGreevy, R., Villalba-Galea, C.A., Hulse, R.E., Roux, B., Schulten, K., et al. (2014). Structural mechanism of voltage-dependent gating in an isolated voltage-sensing domain. Nat. Struct. Mol. Biol. *21*, 244–252.

Lindorff-Larsen, K., Piana, S., Dror, R. O., & Shaw, D. E. (2011). How Fast-Folding Proteins Fold. *Science*, *334*, 517–520.

Long, S.B., Campbell, E.B., and MacKinnon, R. (2005). Voltage sensor of Kv1.2: structural basis of electromechanical coupling. Science *309*, 903–908.

Lu, Z., Klem, A. M., & Ramu, Y. (2001). Ion conduction pore is conserved among potassium channels. *Nature*, *413*(6858), 809–813. http://doi.org/10.1038/35101535

MacKinnon, R. (1991). Determination of the subunit stoichiometry of a voltage-activated potassium channel. Nature *350*, 232–235.

Männikkö, R., Elinder, F., and Larsson, H.P. (2002). Voltage-sensing mechanism is conserved

among ion channels gated by opposite voltages. Nature *419*, 837–841.

Mastronarde, D. N. (2005). Automated electron microscope tomography using robust prediction of specimen movements. *Journal of Structural Biology*, *152*, 36–51. http://doi.org/10.1016/j.jsb.2005.07.007

Nauli, S., Kuhlman, B., Le Trong, I., Stenkamp, R. E., Teller, D., & Baker, D. (2009). Crystal structures and increased stabilization of the protein G variants with switched folding pathways NuG1 and NuG2. *Protein Science*, *11*(12), 2924–2931. http://doi.org/10.1110/ps.0216902

Randich, A. M., Cuello, L. G., Wanderling, S. S., & Perozo, E. (2014). Biochemical and structural analysis of the hyperpolarization-activated K+ channel MVP. *Biochemistry*, *53*(10), 1627–1636. http://doi.org/10.1021/bi4014243

Riback, J. A., Bowman, M. A., Zmyslowski, A. M., Knoverek, C. R., Jumper, J. M., Hinshaw, J. R., et al. (2017). Innovative scattering analysis shows that hydrophobic disordered proteins are expanded in water. *Science*, *358*(6360), 238–241. http://doi.org/10.1126/science.aan5774

Rohou, A., and Grigorieff, N. (2015). CTFFIND4: Fast and accurate defocus estimation from electron micrographs. J. Struc. Biol. *192*, 216–221.

Rosenthal, P.B., and Henderson, R. (2003). Optimal Determination of Particle Orientation, Absolute Hand, and Contrast Loss in Single-particle Electron Cryomicroscopy. J. Mol. Biol. *333*, 721–745.

Scheres, S.H.W. (2012). RELION: Implementation of a Bayesian approach to cryo-EM structure determination. J. Struc. Biol. *180*, 519–530.

Scheres, S.H.W., and Chen, S. (2012). Prevention of overfitting in cryo-EM structure determination. Nat. Methods *9*, 853–854.

Sesti, F., Rajan, S., Gonzalez-Colaso, R., Nikolaeva, N., and Goldstein, S.A.N. (2003). Hyperpolarization moves S4 sensors inward to open MVP, a methanococcal voltage-gated potassium channel. Nat. Neurosci. *6*, 353–361.

Stumpe, S., & Bakker, E. P. (1997). Requirement of a large K+-uptake capacity and of extracytoplasmic protease activity for protamine resistance of Escherichia coli. Archives of Microbiology, 167(2-3), 126–136. http://doi.org/10.1007/s002030050425

Ujwal, R., & Bowie, J. U. (2011). Crystallizing membrane proteins using lipidic bicelles. Methods, 55(4), 337–341. http://doi.org/10.1016/j.ymeth.2011.09.020

Uysal, S., Vásquez, V., Tereshko, V., Esaki, K., Fellouse, F. A., Sidhu, S. S., et al. (2009). Crystal structure of full-length KcsA in its closed conformation. *Proceedings of the National Academy of Sciences*, *106*(16), 6644–6649.

Vardanyan, V., and Pongs, O. (2012). Coupling of voltage-sensors to the channel pore: A comparative view. Front. Pharmacol. *3*, 1–10.

Vargas, E., Yarov-Yarovoy, V., Khalili-Araghi, F., Catterall, W.A., Klein, M.L., Tarek, M., Lindahl, E., Schulten, K., Perozo, E., Bezanilla, F., et al. (2012). An emerging consensus on voltage-

dependent gating from computational modeling and molecular dynamics simulations. J. Gen. Physiol. *140*, 587–594.

Wainger, B. J., Degennaro, M., Santoro, B., Siegelbaum, S. A., & Tibbs, G. R. (2001). Molecular mechanism of cAMP modulation of HCN pacemaker channels. *Nature*, *411*, 805–810.

Whicher, J.R., and MacKinnon, R. (2016). Structure of the voltage-gated K+ channel Eag1 reveals an alternative voltage sensing mechanism. Science *353*, 664–669.

Xu, H., Hackos, D.H., Koth, C.M., Xu, H., Li, T., Rohou, A., Arthur, C.P., Tzakoniati, F., Wong, E., and Estevez, A. (2019). Structural Basis of Nav1.7 Inhibition by a Gating-Modifier Spider Toxin. Cell *176*, 702–715.

Yifrach, O., and MacKinnon, R. (2002). Energetics of pore opening in a voltage-gated K+ channel. Cell *111*, 231–239.

Zheng, S.Q., Palovcak, E., Armache, J.-P., Verba, K.A., Cheng, Y., and Agard, D.A. (2017). MotionCor2: anisotropic correction of beam-induced motion for improved cryo-electron microscopy. Nat. Methods *14*, 331–332.

Chapter 5: Conclusion

This thesis was guided by the following overarching question: how does voltage open an ion channel? We chose to address this question by studying the determinants of gating polarity, that is: how can similar VSD motions close some channels yet open others? What are the minimal structural and dynamic features necessary to make a channel depolarization vs hyperpolarization-activated? Here, studying several model systems using structural and functional techniques we begin to answer these questions.

In chapter two, we described the structure of KAT1, with an 'up' sensor and a closed gate. KAT1 marks only the second hyperpolarization-activated ion channel of known structure, and in combination with the structure of HCN1 (Lee and MacKinnon 2017), as well as depolarization-activated Eag1 (Whicher and MacKinnon 2016), we can begin to draw some general conclusions. KAT1 and HCN1 show different VSD-pore interfaces (in terms of S4-S5 inter-helical packing), which suggests a divergence in activation mechanism. Accordingly, certain HCN channels remain functional when their C-linker and CNBD are deleted (Wainger et al. 2001), while in KAT1, an R to K mutation in the C-linker abolishes function. Thus, there appear to be two distinct pathways for VSD coupling (at a minimum). The first likely lies within the plane of the membrane, formed by interactions between S4 and S5 helices. This interface likely plays a role in HCN1 activation (Lee and MacKinnon 2017), as well as in MVP activation: MVP lacks a C-linker and CNBD, and is thus the smallest natively hyperpolarization-activated ion channel known (chapter 4) (Sesti et al. 2003; Randich et al. 2014). The second pathway is likely found at the intracellular end of the channel, in which the intracellular end of the S4 contacts the C-linker. This interface is likely the predominant pathway for coupling in KAT1, and also likely contributes significantly to native HCN gating (Lee and MacKinnon 2017). To generalize further, I suggest that group formed by HCN (animal), KAT (plant), and MVP (archaea) represent the entirety of

the hyperpolarization-activated ion channel family. Thus, if we are to interpret our low-resolution MVP cryo-EM map, we can conclude that a non-domain-swapped architecture is a universal feature of hyperpolarization-activated ion channels.

In chapter 3, as a test of our understanding of electromechanical coupling and gating polarity, we attempted to flip the gating polarity of an ion channel using single residue substitutions. We began a mutagenic walk between KAT1 and SKOR, *Arabidopsis* channels gating with opposite polarity yet sharing 47% sequence identity in the TMD regions. In this process, we have discovered a mutant that gates in two distinct modes: one mode opens at depolarizing potentials, the other mode closes at depolarizing potentials. Also in chapter 3 we laid the foundation for structural studies of the open state of KAT1. Using protein-engineering to design KAT1 variants open at 0 mV in electrophysiology experiments, we found promising candidates for structural analysis. Preliminary cryo-EM suggests these variants are captured in conformations different than that of wildtype KAT1. Physiological interpretation of such a conformational difference awaits both higher resolution reconstructions, and experiments to control for detergent-lipid effects on protein conformation. Both the flipping mutants and putative open mutants of KAT1 are fruitful areas for future work.

Overall, we highlight the intriguing structural, and likely mechanistic, diversity among hyperpolarization-activated ion channels, which are interesting in their own right (Latorre et al. 2003; Mannikko et al. 2002; Sesti et al. 2003). Additionally, we have begun to apply our findings to depolarization-activated ion channels to understand electromechanical coupling in more general terms. In doing so, we found an expected link between KAT1 and Eag1, in that they are likely both directly coupled, and that the S4-S5-C-linker interface may be a determinant of gating polarity.

References

Latorre, R., Olcese, R., Basso, C., Gonzalez, C., Muñoz, F., Cosmelli, D., and Alvarez, O. (2003). Molecular Coupling between Voltage Sensor and Pore Opening in the Arabidopsis Inward Rectifier K+ Channel KAT1. J. Gen. Physiol. *122*, 459–469.

Lee, C.-H., and MacKinnon, R. (2017). Structures of the Human HCN1 Hyperpolarization-Activated Channel. Cell *168*, 111–120.

Männikkö, R., Elinder, F., and Larsson, H.P. (2002). Voltage-sensing mechanism is conserved among ion channels gated by opposite voltages. Nature *419*, 837–841.

Randich, A. M., Cuello, L. G., Wanderling, S. S., & Perozo, E. (2014). Biochemical and structural analysis of the hyperpolarization-activated K+ channel MVP. *Biochemistry*, *53*(10), 1627–1636. http://doi.org/10.1021/bi4014243

Sesti, F., Rajan, S., Gonzalez-Colaso, R., Nikolaeva, N., and Goldstein, S.A.N. (2003). Hyperpolarization moves S4 sensors inward to open MVP, a methanococcal voltage-gated potassium channel. Nat. Neurosci. *6*, 353–361.

Wainger, B. J., Degennaro, M., Santoro, B., Siegelbaum, S. A., & Tibbs, G. R. (2001). Molecular mechanism of cAMP modulation of HCN pacemaker channels. *Nature*, *411*, 805–810.

Whicher, J.R., and MacKinnon, R. (2016). Structure of the voltage-gated K+ channel Eag1 reveals an alternative voltage sensing mechanism. Science *353*, 664–669.